Cross-Shore Irregular Wave Transformation and Sediment Transport in Surf and Swash Zones

by

Bradley D. Johnson

and

Nobuhisa Kobayashi

RESEARCH REPORT NO. CACR-00-05

November, 2000

Center for Applied Coastal Research
Ocean Engineering Laboratory
University of Delaware
Newark, DE 19716

ACKNOWLEDGMENTS

This work was supported by the NOAA Office of Sea Grant under Grant No. NA85AA-D-SG033 (Projects SG R/OE-23 and SG PD), and the National Science Foundation under Grant OCE-9901471.

TABLE OF CONTENTS

LIST OF FIGURES

LIST OF TABLES

ABSTRACT

Models that predict the fluid motion in the surf and swash zones on a beach are necessary in the effort to understand nearshore processes. The movement of sediment and the associated shoreline change are caused by the action of waves and current over time. The following endeavor presents contributions to the quantitative understanding of the cross-shore wave transformation and sand transport processes in surf and swash zones on beaches.

First, a time-averaged model that is based on the finite-amplitude shallow-water equations is developed to predict the root-mean-square wave height, wave setup, and free surface skewness and kurtosis from outside the surf zone to the inner swash zone. This new model includes nonlinear correction terms in the cross-shore radiation stress and energy flux that become important in very shallow water. Calibration and initial comparisons to laboratory tests are presented; additional comparisons to independent laboratory tests and field data are presented as verification. The model is shown to effectively predict the cross-shore variations of the skewness and kurtosis as well as the root-mean-square wave height and setup on laboratory and natural beaches.

Second, a time-averaged model to predict both erosional and accretional beach profile evolutions under the assumptions of alongshore uniformity and normally incident waves is presented. In the development of the model, the cross-shore sediment transport in surf zones on beaches is analyzed on the basis of the time-dependent, depth-integrated sediment continuity equation including sediment suspension, storage, advection and settling. The energetics approach is shown to

correspond to the special case of local equilibrium between sediment suspension and settling. The corresponding time-averaged model together with the simplified assumptions of Dean (1977) yields a uniform suspension rate for the standard equilibrium profile. The simplified time-averaged model with new moving boundary conditions at the shoreline and breaker point is compared with erosional and accretional beach profile evolutions under regular waves in a large tank. The sediment suspension rate estimated for the equilibrium terraced and barred beaches under irregular waves is found to be roughly uniform in the surf zone but increases significantly in the swash zone.

Finally, a time-dependent, cross-shore sediment transport model in the surf and swash zones on beaches is developed to predict both beach accretion and erosion under the assumptions of alongshore uniformity and normally incident waves. The model is based on the depth-integrated sediment continuity equation which includes sediment suspension by turbulence generated by wave breaking and bottom friction, sediment storage in the entire water column, sediment advection by waves and wave-induced return current, and sediment settling on the movable bottom. The hydrodynamic input required for this sediment transport model is predicted using the finite-amplitude, shallow-water equations including bottom friction. The developed model is compared with three large-scale laboratory tests with accretional, neutral (little), and erosional beach profile changes under regular waves. The model predicts sediment suspension and sediment concentration in a physically realistic manner. The present computation is limited to the initial beach profile change, but the numerical model is capable of predicting the accretional, erosional and neutral profile changes.

Chapter 1

INTRODUCTION

The majority of the U.S. coastline is currently suffering from erosion, causing considerable public concern (National Research Council 1990). This ongoing beach erosion will accelerate if the mean sea-level rise increases due to the greenhouse effect (National Research Council 1987). The U.S. Army Corps of Engineer's shore protection program covers only 8 percent of the nation's 4,300 km of critically eroding shoreline and has shifted from primarily coastal structures to primarily beach restoration and nourishment through placement of sand (Hillyer *et al.* 1997). The performance of beach nourishment and protection projects is presently being predicted by extrapolating historical shoreline changes (National Research Council 1995) because none of the existing models can predict long-term shoreline changes resulting from erosion during storms and recovery between storms. At present, no model can predict the net onshore sand transport in the surf and swash zones during the post-storm recovery.

Our understanding of nearshore hydrodynamics and sediment transport mechanics were reviewed by Peregrine (1983), Grant and Madsen (1986), Komar and Holman (1986), Battjes (1988), Kobayashi (1988), Raudkivi (1990), Svendsen and Putrevu (1995), and Nielsen (1992). Considering the complexity of the nearshore processes including the spatial and temporal variability of sand bar morphology

(Lippmann and Holman) and shoreline position (Plant and Holman 1996), the following study is limited to the cross-shore processes under the assumption of alongshore uniformity and normally incident waves. The seaward increase of sand diameter observed on natural beaches [e.g. Thornton *et al.* (1996)] is not considered in the following analyses. Longshore currents (Bowen 1969; Longuet-Higgins 1970) and sediment transport [e.g. Hanson and Kraus (1989)] are better understood apart from the uncertainties of the cross-shore and vertical distributions of the longshore currents [e.g. Gallagher *et al.* (1998); Garcez Faria (1998)] and longshore sediment fluxes [e.g. Wang (1998)].

Three related mathematical models are presented here in the effort to predict short-term and long-term changes of beach profiles and shoreline positions. Chapter 2 presents a new time-averaged irregular wave model. Chapter 3 discusses a new beach profile evolution model. Chapter 4 presents a new time-dependent sediment transport model. Each of Chapters 2–4 is self-contained with independent introduction and notations because each chapter deals with related but different aspects of nearshore processes. Each of Chapters 2–4 is explained in the following, and the conclusions are presented in Chapter 5.

A computationally efficient wave model for the wave motion in the swash zone on a beach is necessary in the effort to predict beach erosion and recovery near the shoreline. While time-dependent shallow-water wave models have some success in predicting surf and swash characteristics, the significant computation time makes these models less suitable for beach profile models. The time-averaged models for random waves are much more efficient computationally but do not predict the wave conditions in the swash zone. A nonlinear time-averaged model that is based on the finite-amplitude shallow-water equations is developed in Chapter 2 to predict the root-mean-square wave height, wave setup, and free surface skewness and kurtosis

from outside the surf zone to the inner swash zone. This model is based on the time-averaged shallow-water continuity, momentum, and energy equations and includes nonlinear correction terms in the cross-shore radiation stress and energy flux that become important in very shallow water. The time-averaged equations can be solved numerically with much less computation time but require empirical relationships to close the problem as shown in Chapter 2.

Calibration and initial comparisons were conducted of this time-averaged wave model with data from three laboratory tests on 1:16 slope and two tests with quasi-equilibrium terraced and barred beaches consisting of fine sand. This time-averaged model is shown to be capable of predicting the cross-shore variations of setup and root-mean-square wave height of the free surface elevation from outside the surf zone to the lower swash zone of frequent wave uprush and downrush including the observed large increase of wave setup near the still water shoreline. In order to ascertain the applicability of the model to conditions different from tests used for calibration, the model is verified using independent data sets including new laboratory tests on a 1:30 slope that included runup measurements. Additionally, the model predictions are compared to field data collected at Duck, North Carolina. The model is shown to effectively predict the cross-shore variations of the skewness and kurtosis as well as the root-mean-square wave height and setup on laboratory and natural beaches. The exponential gamma distribution is shown to be capable of describing the measured probability distributions of the shoreline elevation as well as the free surface elevation in the field. The computationally efficient solution of irregular wave motions may make this model suitable for the prediction of sediment movement and the associated coastline changes.

Existing models have some success in predicting the sediment dynamics involved in offshore sediment transport. However, it is more difficult to predict the accretional case where sand grains are deposited on beaches. A simple time-averaged

model with moving boundary conditions at the shoreline and breaker point is shown to predict both erosional and accretional beach profile evolutions in Chapter 3. Existing models assume that the local sediment transport rate is determined by the local hydrodynamic forcing and sediment characteristics without regard to cross-shore sediment advection. The net cross-shore sediment transport rate, however, may be affected by sediment advection from or into the surrounding areas. A new cross-shore sediment transport model is developed that includes sediment suspension by turbulence generated by wave breaking and bottom friction, sediment storage in the entire water column, sediment advection by waves and wave-induced currents, and sediment settling on the movable bed. The energetics approach is shown to correspond to the special case of local equilibrium between sediment suspension and settling. The corresponding time-averaged model together with the simplified assumptions of Dean (1977) yields a uniform suspension rate for the standard equilibrium profile with the scale parameter A as a function of the sediment fall velocity. The simplified time-averaged model with new moving boundary conditions at the shoreline and breaker point is compared with erosional and accretional beach profile evolutions under regular waves in a large tank. The sediment suspension rate estimated for the equilibrium terraced and barred beaches under irregular waves is found to be roughly uniform in the surf zone but increase significantly in the swash zone.

The existing cross-shore beach profile models generally use sediment transport models that are too simplistic to predict both beach erosion and accretion. A one-dimensional, time-dependent model is developed in Chapter 4 to predict the depth-integrated sediment dynamics and resulting beach profile change in surf and swash zones. The depth-integrated sediment continuity equation includes sediment

suspension by turbulence generated by wave breaking and bottom friction, sediment storage in the entire water column, sediment advection by waves and wave-induced return current, and sediment settling on the movable bottom. The hydrodynamic input required for this sediment transport model is predicted using the finite-amplitude, shallow-water equations including bottom friction. The developed model is compared with the three large-scale laboratory tests with accretional, neutral (little), and erosional beach profile changes under regular waves as in Chapter 3. The model predicts sediment suspension under the steep front of breaking waves and due to bottom friction in the swash zone. The computed depth-averaged sediment concentration does not respond to local sediment suspension instantaneously because of the sediment storage and advection. The mean sediment concentration becomes large in comparison to the oscillatory concentration with the decrease of the normalized sediment fall velocity. The net cross-shore sediment transport rate is shown to be the small difference between the onshore transport rate due to the positively-correlated oscillatory components of the suspended sediment volume per unit area and the horizontal sediment velocity and the offshore transport rate due to the product of the mean suspended sediment volume and the mean horizontal sediment velocity. Relatedly, the net accretion or erosion rate of the movable bottom is determined by the small difference between the mean sediment settling rate and the mean suspension rate caused by wave breaking and bottom friction. The model successfully predicts the initial accretional, erosional and neutral beach profile changes.

Chapter 2

TIME-AVERAGED IRREGULAR WAVE MODEL

2.1 Introduction

The need for a simple model for the wave motion in the swash zone on a beach has been pointed out in relation to the prediction of beach erosion and recovery near the shoreline [e.g., Hedegaard *et al.* (1992)]. The time-dependent numerical model based on the finite-amplitude shallow-water equations (Kobayashi and Wurjanto 1992) has been shown to be capable of predicting the swash characteristics on natural beaches (Raubenheimer *et al.* 1995; Raubenheimer and Guza 1996). Alternatively, time-dependent models based on extended Boussinesq equations have been developed to elucidate the nonlinear wave transformation processes in the shoaling, surf and swash zones [e.g., Schäffer et al. (1992)]. These time-dependent numerical models, however, require significant computation time to resolve the breaking wave profiles varying rapidly in time and space.

On the other hand, the time-averaged models for random waves represented by the root-mean-square wave height or expressed as the superposition of regular waves are more efficient computationally at the expense of the loss of the detailed temporal information, such as the skewness of the wave profile which is regarded to be important for the onshore sediment transport on beaches [e.g., Guza and Thornton (1985)]. The time-averaged models for random waves represented by the root-mean-square wave height (Battjes and Janssen 1978; Thornton and Guza 1983) or expressed as the superposition of regular waves (Dally 1992; Mase and

Kobayashi 1991) are much more efficient computationally but do not predict the wave conditions in the swash zone (Cox *et al.* 1994a).

A nonlinear time-averaged model is developed to predict the cross-shore variations of the wave setup, $\overline{\eta}$, and the root-mean-square wave height, H_{rms}, from outside the surf zone to the lower swash zone where H_{rms} is defined as $H_{rms} = \sqrt{8}\,\sigma$ with σ = standard deviation of the free surface elevation. This model is based on the time-averaged continuity, momentum, and energy equations derived by time-averaging the nonlinear equations used in the time-dependent model of Kobayashi and Wurjanto (1992). The time-averaged equations can be solved numerically with much less computation time but require empirical relationships to close the problem. The time-averaged rate of energy dissipation due to random wave breaking is estimated by modifying the empirical formula of Battjes and Stive (1985) to account for the landward increase of $H_{rms}/\overline{h}$ near the shoreline where $\overline{h}$ = mean water depth. The skewness s and the kurtosis K of the free surface elevation included in the time-averaged momentum and energy equations are expressed empirically as a function of $H_{rms}/\overline{h}$.

The developed model is calibrated with three tests conducted on a 1:16 smooth impermeable slope and two tests on quasi-equilibrium terraced and barred beaches consisting of fine sand (Johnson and Kobayashi 1998a). This time-averaged model is shown to be capable of predicting the cross-shore variations of $\overline{\eta}$ and H_{rms} of the free surface elevation from outside the surf zone to the lower swash zone of frequent wave uprush and downrush. The model of Battjes and Stive (1985) considerably underpredicts $\overline{\eta}$ and H_{rms} near the still water shoreline.

In order to ascertain the applicability of the model to conditions different from tests used for calibration, the model is verified using independent data sets. Five additional laboratory tests on a 1:30 slope were conducted that included runup measurements. The model is compared with these five additional tests as well as

field data taken during storm conditions at Duck, North Carolina. The model is shown to effectively predict the cross-shore variations of the skewness and kurtosis as well as the root-mean-square wave height and setup on laboratory and natural beaches. The exponential gamma distribution (Kobayashi *et al.* 1998) is shown to be capable of describing the measured probability distributions of the shoreline elevation as well as the free surface elevation in the field.

2.2 Model Formulation

The assumptions of alongshore uniformity and normally incident irregular waves are made in the following. For flow on an impermeable beach, the the finite-amplitude shallow-water equations for mass and horizontal momentum can be expressed as [e.g. Kobayashi *et al.* 1989]

$$\frac{\partial h}{\partial t} + \frac{\partial}{\partial x}(hU) = 0 \tag{2.1}$$

$$\frac{\partial}{\partial t}(hU) + \frac{\partial}{\partial t}(hU^2) = -gh\frac{\partial \eta}{\partial x} \tag{2.2}$$

in which x = cross-shore coordinate taken to be positive landward; t = time; ρ = fluid density; g = gravitational acceleration; h = instantaneous water depth; η = instantaneous free surface elevation above the still water level (SWL); and U = instantaneous depth-averaged horizontal velocity. The time-averaged continuity equation corresponding to (2.1) is

$$\overline{hU} = 0 \tag{2.3}$$

where the overbar denotes time-averaging, and use is made of the no flux boundary condition into the impermeable beach. The time-averaged cross-shore momentum equation obtained from (2.2) is written as

$$\frac{dS_{xx}}{dx} = -\rho g \overline{h}\ \frac{d\overline{\eta}}{dx} \tag{2.4}$$

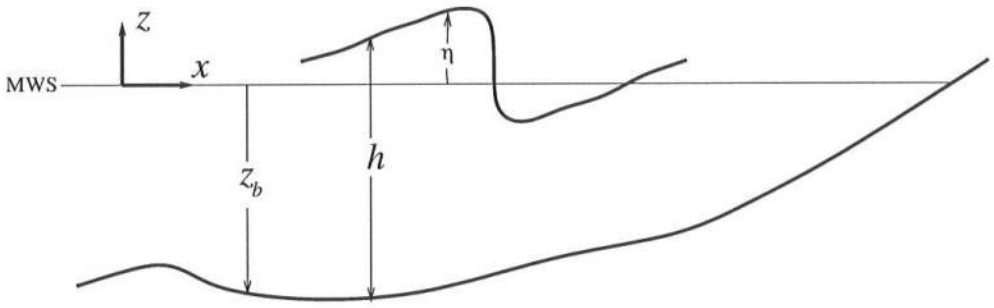

Figure 2.1: Definition Sketch

with

$$S_{xx} = \rho \left[\overline{hU^2} + \frac{1}{2} g \overline{(\eta - \overline{\eta})^2} \right] \tag{2.5}$$

in which S_{xx} may be regarded as the cross-shore radiation stress derived from (2.2). Note that the the radiation stress defined in (2.5) differs from the expressions of Phillips (1977) and Mei (1989) in that the return current $\overline{U}$ is included. The time-averaged bottom shear stress may be neglected in (2.4) as explained by Kobayashi and Johnson (1998). The bottom elevation z_b given by $z_b = (\eta - h)$ is assumed to depend on x only. The time-averaged energy equation corresponding to (2.3) and (2.4) may be expressed as (Kobayashi and Wurjanto 1992)

$$\frac{d}{dx} \left(\overline{E_F} \right) = -\overline{D_B} \tag{2.6}$$

with

$$\overline{E_F} = \frac{1}{2} \rho \, \overline{hU^3} + \rho g \overline{\eta h U} \tag{2.7}$$

in which $\overline{E_F}$ = energy flux per unit width; and $\overline{D_B}$ = energy dissipation rate due to wave breaking, which needs to be estimated empirically in this time-averaged model.

To simplify (2.3), (2.4), and (2.6), the instantaneous free surface elevation η is expressed as

$$\eta = \overline{\eta} + \sigma \eta_* \tag{2.8}$$

where $\overline{\eta}$ and σ are the mean and standard deviation of η, respectively; and $\eta_* =$ normalized free surface elevation with $\overline{\eta_*} = 0$ and $\overline{\eta_*^2} = 1$. If wave reflection is negligible, progressive linear long wave theory may be used locally to relate the oscillatory components $(\eta - \overline{\eta})$ and $(U - \overline{U})$ inside and outside the surf zone (Guza and Thornton 1980; Kobayashi *et al.* 1998). This relationship together with (2.8) yields

$$U = \overline{U} + \sqrt{\frac{g}{\overline{h}}}\,\sigma\eta_* \tag{2.9}$$

Eq. (2.9) is necessary to reduce the number of unknown variables in the time-averaged model although the local reflection coefficient may not be small near the still water shoreline on beaches (Baquerizo *et al.* 1997). Substitution of (2.8) and (2.9) into (2.3) with $h = (\eta - z_b)$ and $\overline{h} = (\overline{\eta} - z_b)$ yields

$$\overline{U} = -\sigma_*^2\,\sqrt{g\overline{h}} \quad ; \quad \sigma_* = \frac{\sigma}{\overline{h}} \tag{2.10}$$

which indicates that $\overline{U}$ is negative and represents return current (Kobayashi *et al.* 1989). Although (2.10) does not account for the landward mass flux due to a surface roller (Svendsen 1984a), it predicted the undertow measured at the mid-depth below SWL fairly accurately (Kobayashi *et al.* 1997b, 1998).

Substitution of (2.8) and (2.9) with (2.10) into (2.5) yields

$$S_{xx} = \frac{1}{8}\,\rho\,g\,H_{rms}^2\left[\left(2n - \frac{1}{2}\right) + C_s\right] \quad ; \quad H_{rms} = \sqrt{8}\,\sigma \tag{2.11}$$

with

$$C_s = \sigma_* s - \sigma_*^2 \tag{2.12}$$

where $s =$ skewness of η and η_* with $\overline{\eta_*^3} = s$; $n =$ finite-depth adjustment parameter or the ratio of group velocity to phase speed with $n = 1$ in shallow water; and $C_s =$ nonlinear correction term for S_{xx}. For linear progressive waves in finite depth, n is normally expressed as [e.g., Dean and Dalrymple (1984)]

$$n = \frac{1}{2}\left[1 + \frac{2k_p\overline{h}}{\sinh\left(2k_p\overline{h}\right)}\right] \tag{2.13}$$

where k_p = linear wave number corresponding to the spectral peak period T_p outside the surf zone. The cross-shore variation of T_p may be neglected in (2.13) because $n = 1$ in shallow water for any reasonable representative wave period used to calculate k_p. The cross-shore radiation stress S_{xx} based on linear wave theory is given by (2.11) with $C_s = 0$. C_s is on the order of unity near the still water shoreline and can not be neglected in the swash zone (Kobayashi and Johnson 1998).

Substitution of (2.8) and (2.9) with (2.10) into (2.7) yields

$$\overline{E}_F = \frac{1}{8}\,\rho\,g\,H_{rms}^2\,n\,C_p(1+C_F) \tag{2.14}$$

with

$$C_F = \frac{3}{2}\,s\,\sigma_*\left(1-\sigma_*^2\right) + \frac{1}{2}\,\sigma_*^2\,(K-5) + \sigma_*^4 \tag{2.15}$$

where C_p = phase velocity based on T_p with $C_p = \sqrt{g\overline{h}}$ in shallow water; C_F = nonlinear correction term for $\overline{E}_F$. The kurtosis K = of η and η_* is

$$K = \left(\frac{\eta-\overline{\eta}}{\sigma}\right)^4 = \overline{\eta_*^4} \tag{2.16}$$

The finite-depth adjustment is included in (2.14) in the same way as (2.11) where $n\,C_p$ in (2.14) is the group velocity based on T_p. The cross-shore energy flux $\overline{E}_F$ based on linear wave theory is given by (2.14) with $C_F = 0$ where C_F is on the order of unity near the still water shoreline (Kobayashi and Johnson 1998).

The momentum equation (2.4) with (2.11) and the energy equation (2.6) with (2.14) need to be solved numerically to predict the cross-shore variations of the wave setup $\overline{\eta} = (\overline{h} + z_b)$ and the root-mean-square wave height $H_{rms} = \sqrt{8}\,\sigma$. These equations reduce to those used in the existing time-averaged models [e.g., Battjes and Stive (1985)] if $C_s = 0$ and $C_F = 0$. To estimate the nonlinear correction terms C_s and C_F using (2.12) and (2.15) with $\sigma_* = \sigma/\overline{h}$, the skewness s and the kurtosis K are assumed to be expressed in the following empirical forms

$$s = f_s\left(H_{rms}/\overline{h}\right) \quad ; \quad K = f_K(s) \tag{2.17}$$

where f_s and f_K = empirical functions which will be obtained using the five tests discussed later.

Finally, the energy dissipation rate $\overline{D}_B$ due to wave breaking in the energy equation (2.6) needs to be estimated. The empirical formula proposed by Battjes and Janssen (1978) and calibrated by Battjes and Stive (1985) is adopted here for its simplicity. The formula proposed by Thornton and Guza (1983) may predict the distributions of breaking and nonbreaking wave heights more accurately but requires additional empirical parameters. In the present formulation, the exponential gamma function may be used to describe the probability density function of η instead of wave heights after the cross-shore variations of $\overline{\eta}$, σ, and s are predicted (Kobayashi *et al.* 1997b, 1998).

The calibrated formula by Battjes and Stive (1985) is given by

$$\overline{D_B} = \frac{\alpha}{4} \rho\, g\, f_p\, Q\, H_m^2 \tag{2.18}$$

with

$$\frac{Q-1}{\ln Q} = \left(\frac{H_{rms}}{H_m}\right)^2 \tag{2.19}$$

$$H_m = \frac{0.88}{k_p} \tanh\left(\frac{\gamma\, k_p\, \overline{h}}{0.88}\right) \tag{2.20}$$

$$\gamma = 0.5 + 0.4 \tanh\left(33\, \frac{H_{rmso}}{L_o}\right) \quad ; \quad L_o = \frac{g\, T_p^2}{2\pi} \tag{2.21}$$

where α = empirical coefficient recommended as $\alpha = 1$; f_p = spectral peak frequency given by $f_p = T_p^{-1}$; Q = local fraction of breaking waves in the range $0 \le Q \le 1$; H_m = local depth-limited wave height; k_p = linear wave number calculated using f_p and $\overline{h}$; γ = empirical parameter determining $H_m = \gamma \overline{h}$ in shallow water; L_o = deep-water wavelength based on T_p; and H_{rmso} = deep-water value of H_{rms} calculated using linear wave shoaling theory with T_p, $\overline{h}$ and H_{rms} specified at the seaward boundary of the numerical model.

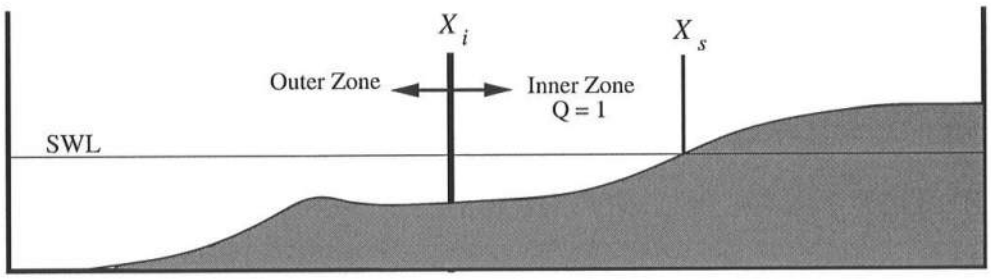

Figure 2.2: Sketch of the Boundary Between the Inner and Outer Zones

The empirical parameter γ is uncertain in light of the field data by Raubenheimer *et al.* (1996) but is estimated using (2.21) without any additional calibration. Relatedly, Battjes and Janssen (1978) indicated that $\overline{D}_B$ given by (2.18) would underestimate the actual energy dissipation rate and produce $H_{rms} > H_m$ near the shoreline, although (2.19) with $Q \leq 1$ requires $H_{rms} \leq H_m$. They recommended use of a cutoff of $H_{rms} = H_m$ when $H_{rms} > H_m$. This adjustment leads to $H_{rms} = \gamma\overline{h}$ near the shoreline. However, $H_{rms}/\overline{h}$ is not constant and increases landward where $H_{rms}/\overline{h} \simeq 2$ at the still water shoreline for the SUPERTANK data of Kriebel (1994). It is interesting to note that the simple theoretical analysis of Svendsen (1984b) also indicates a $H_{rms}/\overline{h} \simeq 2$. As a result of landward increase, (2.18) with (2.19)–(2.21) is assumed to be valid only in the outer zone $x < x_i$ with x_i = cross-shore location where Q computed by (2.19) becomes unity and the still water depth decreases landward in the region $x > x_i$. The latter condition is required for a barred beach to allow $Q < 1$ landward of the bar crest where $Q = 1$ may occur. An example of the boundary between the inner and outer zones is shown in Figure 2.2. For the inner zone $x > x_i$, the ratio $H_* = H_{rms}/\overline{h}$ is assumed to be expressed as

$$H_* = \gamma + (\gamma_s - \gamma)\, x_*^{\beta} \quad ; \quad x_* = \frac{x - x_i}{x_s - x_i} > 0 \tag{2.22}$$

where γ_s = value of H_* on the order of two at the still water shoreline located at $x = x_s$; and β = empirical parameter. The values of γ_s and β will be calibrated using the five tests discussed later. Eq. (2.22) describes the landward increase of

H_* from $H_* = \gamma$ at $x = x_i$ to $H_* = \gamma_s$ at $x = x_s > x_i$. For the inner zone $x > x_i$, the momentum equation (2.4) and (2.22) are used to predict the cross-shore variations of $\overline{h}$ and H_{rms}, whereas the energy equation (2.6) is used to estimate $\overline{D_B}$ which must be positive or zero.

2.3 Numerical Solution

The numerical model called CSHORE (Kobayashi and Johnson 1998) is developed to solve (2.4) and (2.6) with (2.11)–(2.22) where CSHORE includes the option to include the bottom friction effects neglected in (2.4) and (2.6). The seaward boundary of CSHORE is located at $x = 0$ where the values of T_p, H_{rms} and $\overline{\eta}$ at $x = 0$ are specified as input. The bottom elevation $z_b(x)$ in the region $x \geq 0$ is also specified as input and the location x_s of the still water shoreline is found using $z_b(x = x_s) = 0$. First-order finite-difference approximations of (2.4) and (2.6) are expressed as

$$\overline{\eta}_{j+1} = \overline{\eta}_j - \left[\rho\, g\, (\overline{h}_{j+1} + \overline{h}_j)\right]^{-1} \left\{2\left[(S_{xx})_{j+1} - (S_{xx})_j\right]\right\} \tag{2.23}$$

$$(\overline{E}_F)_{j+1} = (\overline{E}_F)_j - \frac{\Delta x}{2}\left[(\overline{D}_B)_{j+1} + (\overline{D}_B)_j\right] \tag{2.24}$$

where the subscripts $(j+1)$ and j indicate the quantities at nodes located at x_{j+1} and x_j, respectively, with $\Delta x = (x_{j+1} - x_j)$ being the nodal spacing. The first-order numerical method in (2.23) and (2.24) is simple and accurate provided that the nodal spacing Δx is sufficiently small. The computation time is short, and therefore this simple approach may be adequate. In the subsequent computations for the laboratory data, use is made of $\Delta x \simeq 10$ cm. For the known quantities at node j, the unknown quantities at node $(j+1)$ are computed by solving (2.23) and (2.24) using an iteration method starting from σ^2_{j+1} computed using (2.24) with $(\overline{D}_B)_{j+1} = (\overline{D}_B)_j$. The adopted iteration method is found to converge within several iterations. The convergence criteria is based on the differences between the iterated values of σ_{j+1} and $\overline{h}_{j+1}$ being less than the specified small value ϵ, where $\epsilon = 0.01$

mm is used in the subsequent computations. If $Q_{j+1} = 1$ and $(dz_b/dx) > 0$ for $x \geq x_{j+1}$, the inner zone is reached and $x_i = x_{j+1}$ is set.

For the nodes located in the inner zone $x > x_i$, (2.22) is used to obtain $H_* = H_{rms}/\overline{h}$ and $\sigma_* = H_*/\sqrt{8}$. Since the mean water depth $\overline{h}$ can become very small in the inner zone, (2.4) with (2.11) is rewritten as

$$(2P+1)\frac{d\overline{h}}{dx} = -\overline{h}\frac{dP}{dx} - \frac{dz_b}{dx} \qquad \text{for} \quad x > x_i \tag{2.25}$$

with

$$P = \sigma_*^2\left[\left(2n - \frac{1}{2}\right) + \sigma_* s - \sigma_*^2\right] \tag{2.26}$$

A first-order finite difference approximation of (2.25) between nodes j and $(j+1)$ yields

$$\overline{h}_{j+1} = (3P_{j+1} + P_j + 2)^{-1}\left\{(P_{j+1} + 3P_j + 2)\,\overline{h}_j - 2\left[(z_b)_{j+1} - (z_b)_j\right]\right\} \tag{2.27}$$

Eq. (2.27) is solved using an iteration method starting from the value of n_{j+1} involved in P_{j+1} calculated using $\overline{h}_j$ where $(\sigma_*)_{j+1}$ and s_{j+1} are known using (2.22) and (2.17), respectively. Since n given by (2.13) is essentially unity in shallow water, this interaction method converges rapidly. After $\overline{h}_{j+1}$ is computed, the energy equation (2.6) is used to obtain $(\overline{D}_B)_{j+1}$. The computation is marched landward until $\overline{h}_{j+1} < \epsilon$.

2.4 Experiments and Empirical Formulas

Two different experiments were conducted in a wave tank that was 30 m long, 2.4 m wide, and 1.5 m high. These experiments were described in detail by Kobayashi *et al.* (1997b, 1998). Irregular waves based on the TMA spectrum were generated with a piston-type wave paddle. Three tests were conducted with a plywood beach of a 1:16 slope. The water depth in the tank was 76.2 cm. For each test, 17 runs were performed to measure free surface elevations using eight

capacitance wave gauges. Wave gauges partially immersed in gauge wells were used for the free surface measurements near the still water shoreline. In addition, two tests were conducted with a fine sand beach with an initial slope of 1:12. The sand was well-sorted and its median diameter was 0.18 mm. The sediment specific gravity was 2.66, and particles were observed to be suspended by the breaking waves in the surf zone for both tests 4 and 5. The initial slope of the sand was approximately 1:12 for tests 4 and 5. Data were collected from these two tests with specified random waves after the sand beach was exposed to the specified wave action for several days and became quasi-equilibrium with the bottom elevation changes less than about 1 cm/hr. For each of the two tests, 21 runs were performed to measure free surface elevations using ten wave gauges. Wave gauges near the still water shoreline were partially buried in the sand. The duration of each run in these five tests was 400 s and the initial transient duration of 75 s was removed. The sampling rate was 20 Hz.

Table 2.1 lists the wave conditions at the seaward boundary located at $x = 0$ for each of the five tests where d = still water depth; $\overline{\eta}$ = wave setup or set-down; T_p = spectral peak period; and H_{rms} = root-mean-square wave height defined as $H_{rms} = \sqrt{8}\,\sigma$ with σ = standard deviation of the measured free surface oscillation. Tests 1, 2 and 3 are the 1:16 slope tests described by Kobayashi *et al.* (1998), whereas tests 4 and 5 correspond to the sand beach tests explained by Kobayashi *et al.* (1997b). The incident irregular waves were generated on the basis of the TMA spectrum, and the spectral shape was not varied in these experiments. The wave setup or set-down is very small at $x = 0$ outside the surf zone. The measured wave conditions at $x = 0$ include the slight effects of reflected waves. The incident and reflected waves at $x = 0$ were estimated using a three-gauge method by Kobayashi *et al.* (1997b, 1998). Table 2.1 lists the estimated values of the spectral root-mean-square wave height, $H_{inc} = \sqrt{8m_{oi}}$, with m_{oi} = zero-moment of the incident wave

Table 2.1: Wave Conditions at Seaward Boundary and Breaker Parameter γ for Calibration Tests Comprised of Tests 1, 2, 3 Conducted on a Planar 1:16 Slope and Tests 4, 5 Conducted on a Fine Sand Beach.

Test (1)	d (cm) (2)	$\overline{\eta}$ (cm) (3)	T_p (s) (4)	H_{rms} (cm) (5)	H_{inc} (cm) (6)	R (7)	γ (8)	x_i (m) (9)	x_s (m) (10)
1	75.0	0.03	1.5	12.4	12.2	0.14	0.84	11.1	12.0
2	75.0	-0.32	2.8	16.9	15.8	0.15	0.67	9.0	12.0
3	76.2	-0.24	4.7	18.4	18.4	0.17	0.56	8.3	13.0
4	60.0	-0.15	1.6	12.8	12.9	0.19	0.83	13.3	13.8
5	60.0	-0.12	2.8	14.6	14.3	0.25	0.65	12.4	13.7

spectrum at $x = 0$, and the average reflection coefficient, $R = \sqrt{m_{or}/m_{oi}}$, with m_{or} = zero-moment of the reflected wave spectrum at $x = 0$. The difference between H_{rms} and H_{inc} is negligible except for test 2 with $(H_{rms} - H_{inc})/H_{rms} = 0.065$. The reflection coefficient was in the narrow range $0.14 \leq R \leq 0.25$ and slightly larger for tests 4 and 5 with the foreshore slope of about 1:5 at the still water shoreline.

The measured values of $\overline{\eta}$, T_p, and H_{rms} at $x = 0$ listed in Table 2.1 are specified as input to CSHORE. The measured bottom elevation $z_b(x)$ in the region $x \geq 0$ is also specified as input where Table 2.1 lists the cross-shore location x_s of the still water shoreline for each test. The bottom profile $z_b(x)$ will be presented in conjunction with the measured and predicted cross-shore variations of $\overline{\eta}$ and H_{rms}. The breaker parameter γ calculated using (2.21) and the cross-shore location x_i at the seaward limit of the inner zone computed by CSHORE are listed in Table 2.1.

The measured values of $H_* = H_{rms}/\overline{h}$ in the inner zone $x > x_i$ are used to

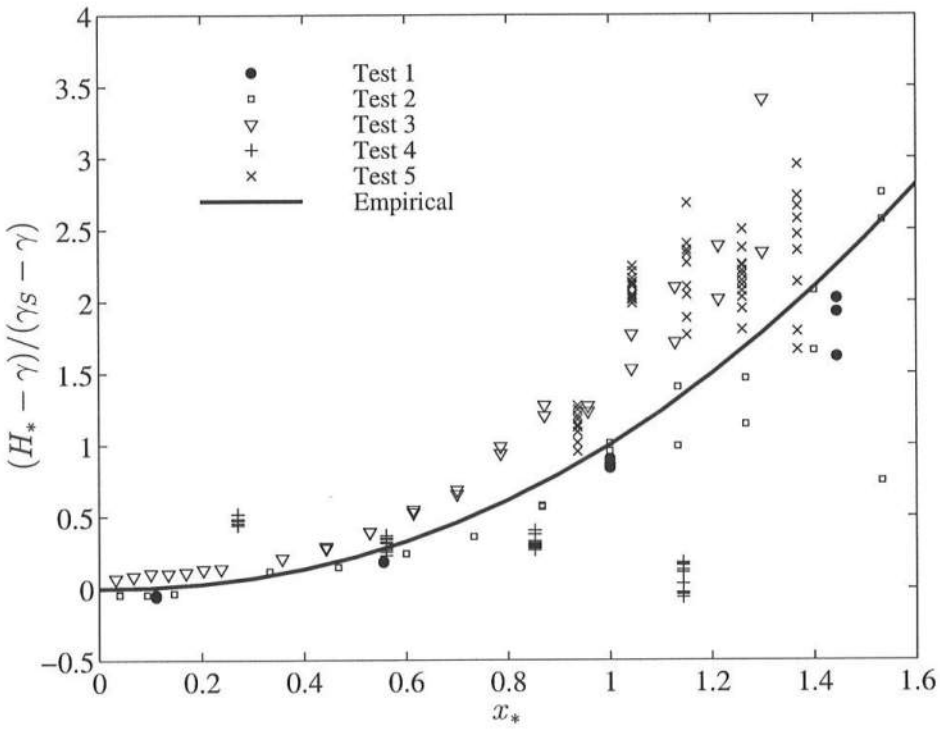

Figure 2.3: Empirical Formula for $H_* = H_{rms}/\overline{h}$ in Inner Zone $x > x_i$.

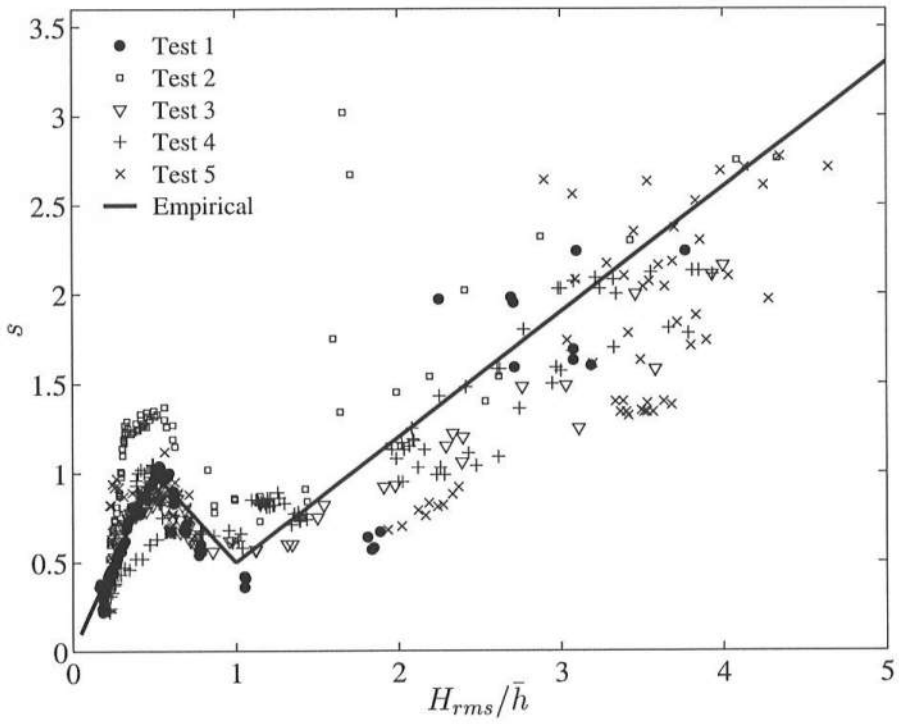

Figure 2.4: Empirical Formula for Skewness s as a Function of H_*.

calibrate the new empirical parameters γ_s and β in (2.22) for the five tests. Figure 2.3 shows the measured values of $(H_* - \gamma)/(\gamma_s - \gamma)$ with $\gamma_s = 2$ as a function of $x_* = (x - x_i)/(x_s - x_i)$ where the values of γ, x_i, and x_s for each test are listed in Table 2.1. The trend of the scattered data points for the five tests may be represented by (2.22) with $\gamma_s = 2$ and $\beta = 2.2$. Figure 2.3 shows that H_* increases gradually from $H_* = \gamma$ at $x_* = 0$ and more rapidly above the still water shoreline located at $x_* = 1$. It is noted that the large scatter in the region $x_* > 1$ is caused partly by the scatter of data points obtained in repeated runs due to the difficulty in measuring the small values of $\overline{h}$ and H_{rms} accurately in the swash zone.

The measured values of H_*, s, and K in the entire region $x \geq 0$ for the five tests are analyzed to obtain the empirical relationships expressed by (2.17). Figure 2.4 shows the skewness s as a function of $H_* = H_{rms}/\overline{h}$. The trend of the scattered

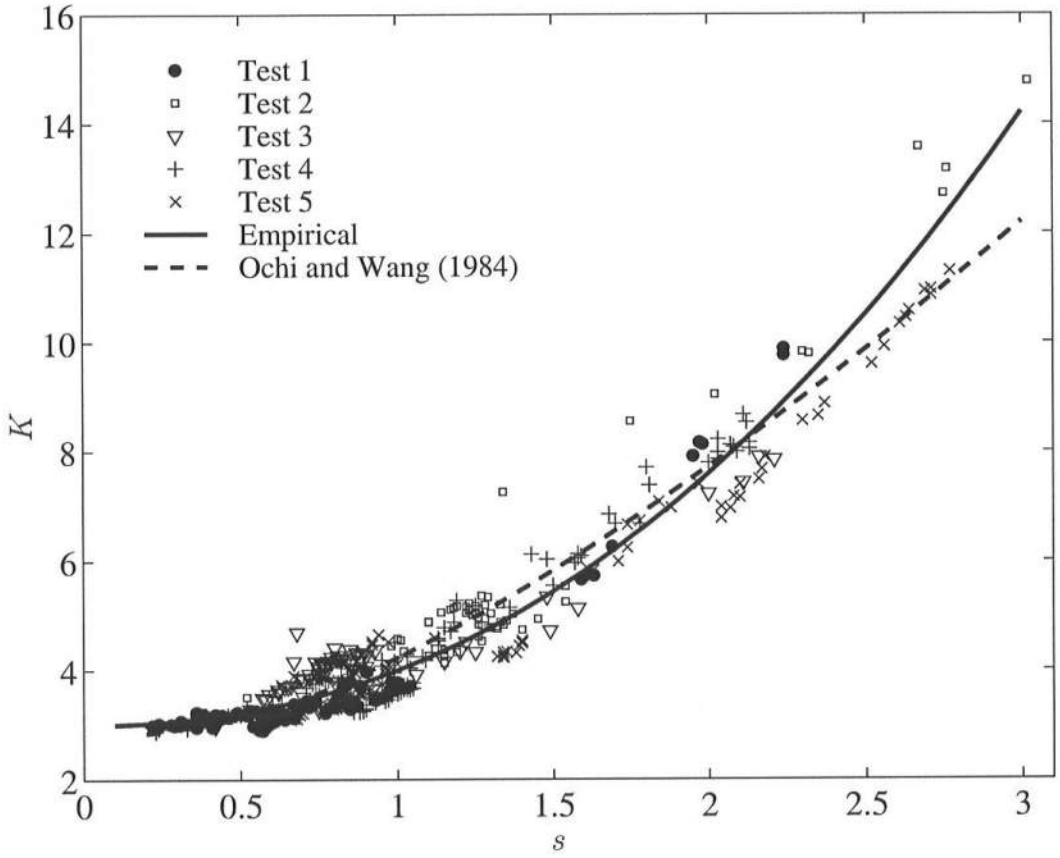

Figure 2.5: Empirical Formula for Kurtosis K as a Function of Skewness s.

data points in Figure 2.4 are simply represented by three straight lines

$$\begin{aligned} s &= 2H_* && \text{for} \quad 0.1 < H_* \leq 0.5 \\ s &= 1.5 - H_* && \text{for} \quad 0.5 \leq H_* \leq 1.0 \\ s &= 0.7H_* - 0.2 && \text{for} \quad 1.0 \leq H_* \lesssim 5 \end{aligned} \tag{2.28}$$

The skewness s increases initially with the increase of H_* due to wave shoaling but decreases after wave breaking. Both s and H_* increase rapidly near and beyond the still water shoreline. Figure 2.5 shows the relationship between the kurtosis K and

the skewness s which may be expressed as

$$K = 3 + s^{2.2} \qquad \text{for} \qquad 0.2 < s \lesssim 3 \tag{2.29}$$

The empirical relationship between K and s proposed by Ochi and Wang (1984) yields similar agreement as shown in Figure 2.5. However, their expression is more complicated and (2.29) is adopted here for its simplicity.

2.5 Comparisons With Five Tests

The numerical model CSHORE is compared with the five tests listed in Table 2.1 and used to develop the empirical formulas (2.28) and (2.29) as well as (2.22) with $\gamma_s = 2$ and $\beta = 2.2$. Figures 2.6–2.8 compare the measured and computed cross-shore variations of $\overline{\eta}$ and H_{rms} for tests 1–5. The variations of $\overline{\eta}$ and H_{rms} computed by the model of Battjes and Stive (BJS hereafter) are also plotted in these figures. The bottom elevation $z_b(x)$ above and below SWL is shown in the first and second panels, respectively, in Figures 2.6–2.8 to show the effects of the beach profile on the wave setup $\overline{\eta}$ and the root-mean-square wave height H_{rms}. The seaward boundary x_i of the inner zone listed in 2.1 is indicated in each figure. The data points from repeated runs in each test are presented without averaging to indicate the degree of the data scatter that was apparent in the swash zone because of the difficulty in measuring small water depth accurately (Kobayashi *et al.* 1997b, 1998). Time averaging in the swash zone was performed for the entire measured time series because the separation of wet and dry durations was difficult due to the presence of a very thin water layer.

For tests 1–3 shown in Figures 2.6 and 2.7, breaker types on the 1:16 smooth slope varied from mostly spilling breakers for test 1 to predominantly plunging breakers for test 3. Correspondingly, the inner zone became wider from test 1 to test 3 where $(x_s - x_i) = 0.9$, 3.0 and 4.7 m for tests 1, 2, and 3, respectively, in

Table 2.1. Comparing CSHORE and the BJS model, the computed variations of $\overline{\eta}$ and H_{rms} in the outer zone $x < x_i$ are practically the same in view of the larger uncertainty associated with the empirical formula (2.18) with (2.19)–(2.21). No attempt is made to calibrate γ to improve the agreement for H_{rms} in the outer zone for test 2. In the inner zone $x > x_i$, CSHORE is capable of predicting the larger increase of the wave setup $\overline{\eta}$ and the more gradual decrease of the wave height H_{rms} in the inner zone.

For tests 4 and 5 shown in Figure 2.8, incident waves shoaled and broke on the small bar at the edge of the terrace. Plunging breakers at the terrace edge were intense in test 5. Wave breaking was reduced on the terrace before incident waves broke again in the swash zone. The BJS model is capable of predicting this wave transformation across the terrace except for the detailed variations of H_{rms} at the terrace edge. The differences between CSHORE and BJS model are limited essentially in the narrow inner zone where $(x_s - x_i) = 0.5$ and 1.3 m for tests 4 and 5, respectively, in Table 2.1. CSHORE allows the extension of BJS model into the lower swash zone.

2.6 Independent Verification on Mild Slope

In order to ascertain the applicability of the model to different conditions, the model is verified using independent data sets. Five additional laboratory tests were conducted that included measurements of runup as well as the free surface. The experiments were conducted in the same wave tank used for the calibration of the model as outlined in Sections 2.4 and 2.5 except that the 1:16 planar slope used in tests 1–5 was replaced with a relatively mild 1:30 slope. The water depth in the tank was 75.0 cm as indicated in Figure 2.9 which shows the general layout for the experiments. For each test, four runs were performed with identical wavemaker input time series; it was demonstrated that the wave field and runup time series were

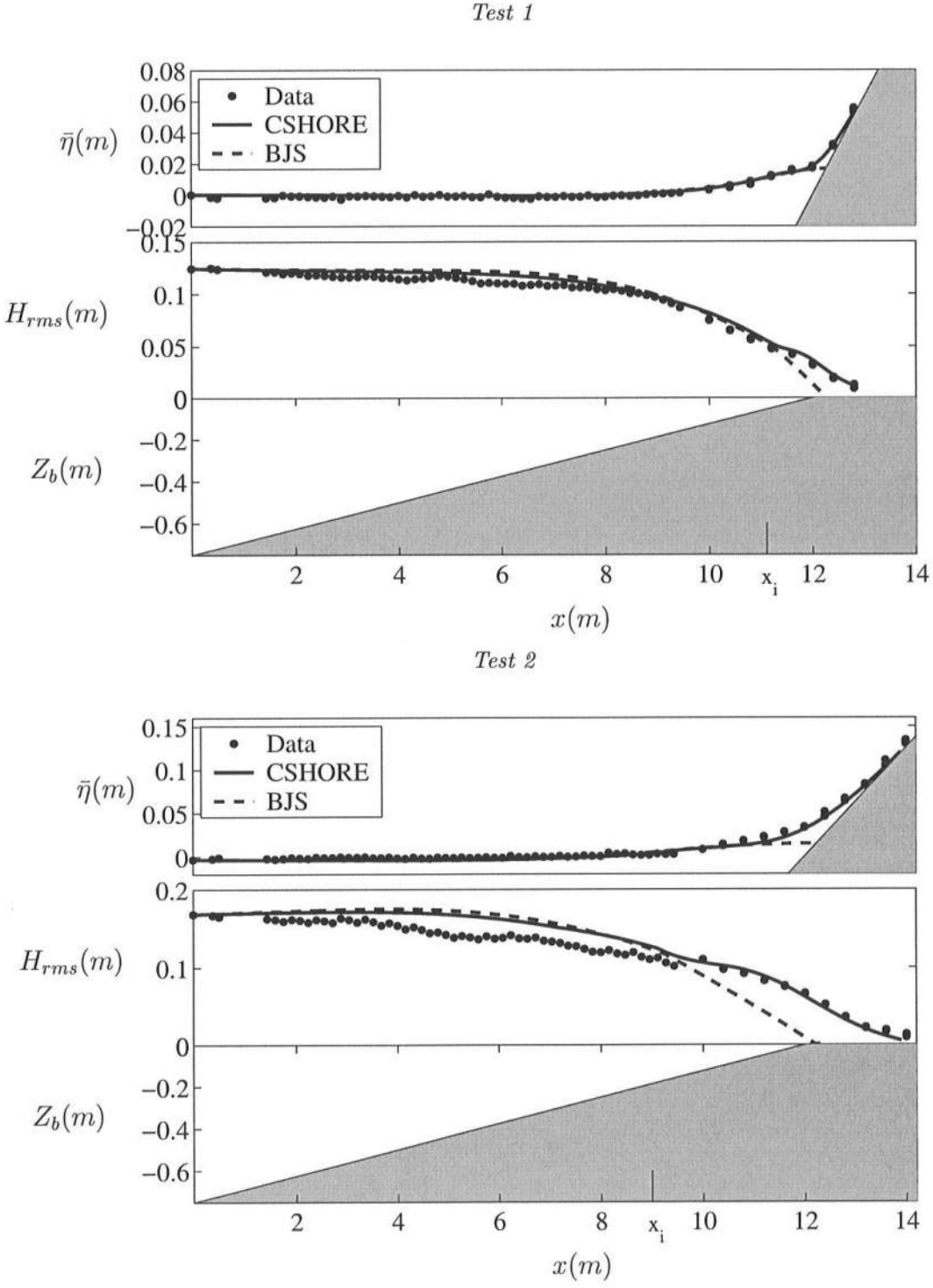

Figure 2.6: Measured and Computed Setup $\overline{\eta}$, and Height H_{rms} for Tests 1 and 2.

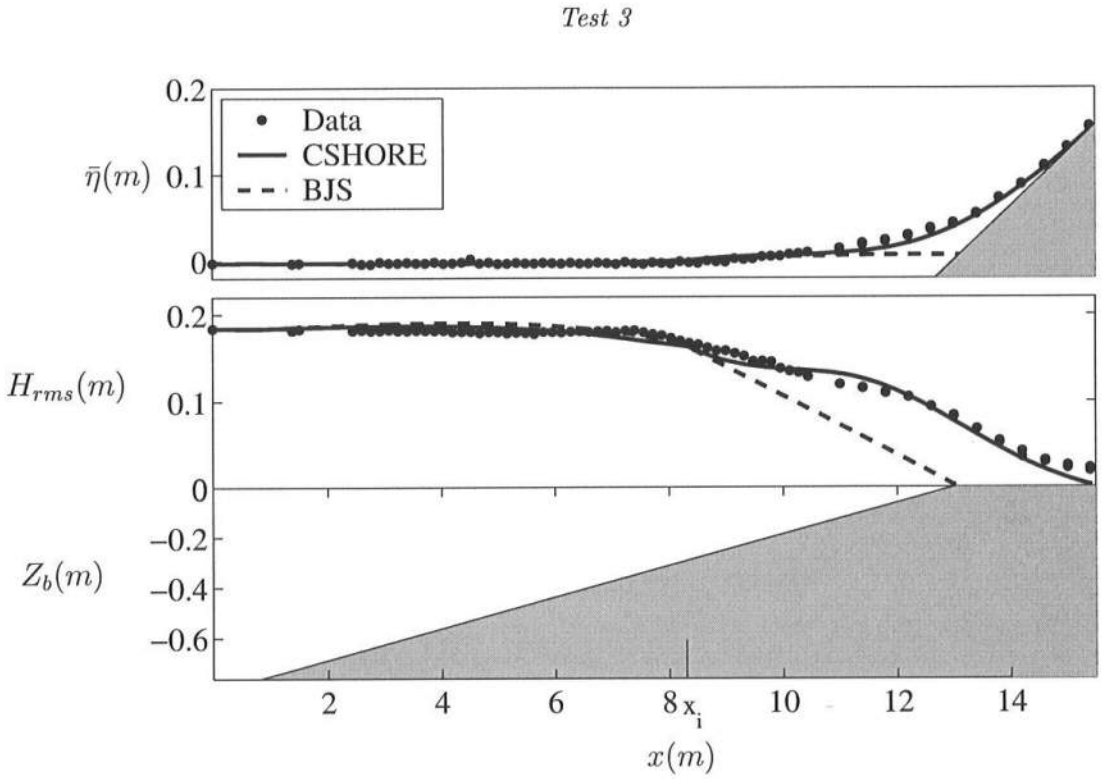

Figure 2.7: Measured and Computed Setup $\overline{\eta}$, and Height H_{rms} for Test 3

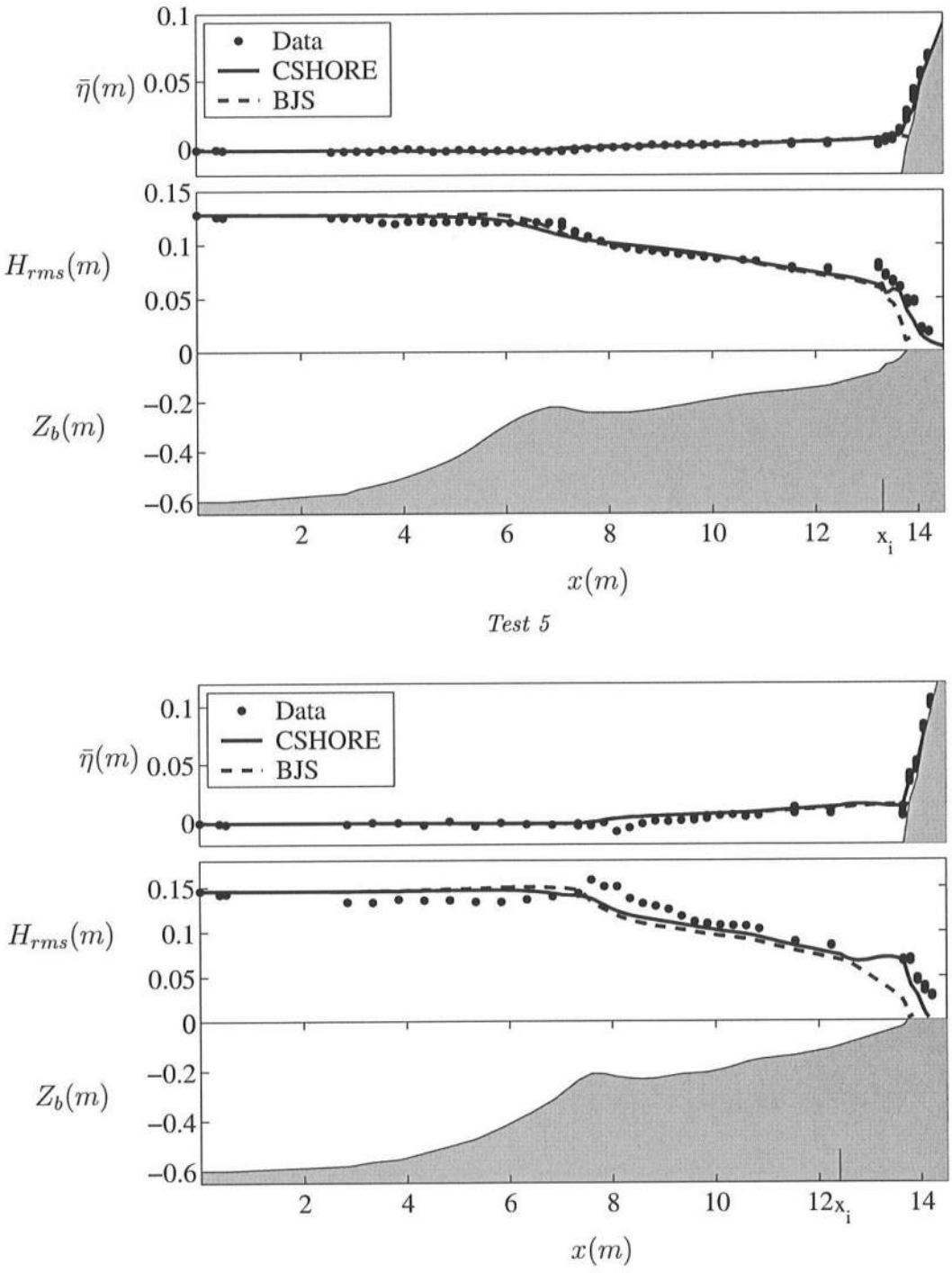

Figure 2.8: Measured and Computed Setup $\overline{\eta}$, and Height H_{rms} for Tests 4 and 5.

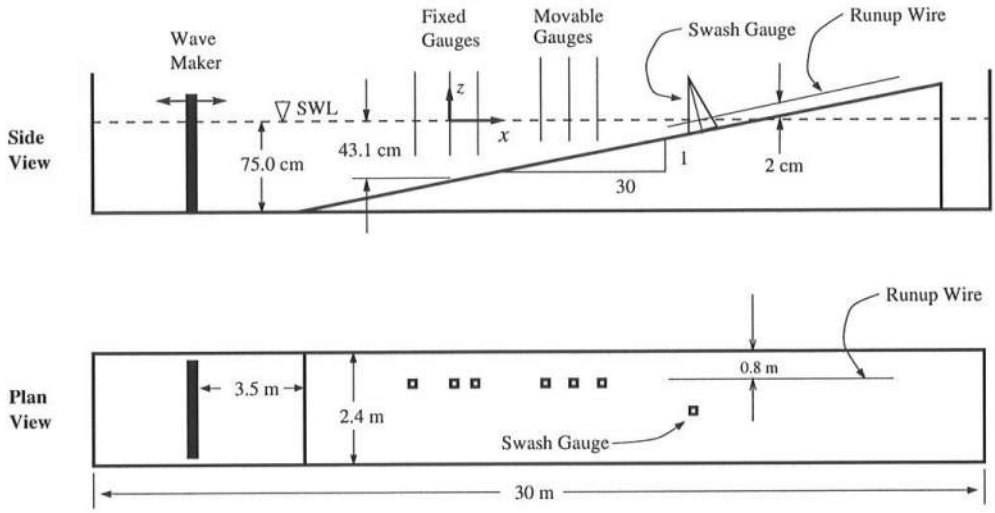

Figure 2.9: Experimental Setup for Tests 6–8 with Planar 1:30 Slope.

practically identical between runs. Detailed measurement of the free surface elevations was conducted using three movable capacitance wave gauges and three fixed gauges that functioned to separate the incident and reflected waves immediately seaward of the breaker zone. A capacitance runup wire placed at a vertical distance of 2 cm above the 1:30 slope was used to measure the shoreline elevation above the still water level (SWL). As in tests 1–5, The duration of each run in these five tests was 400 s with a data sampling rate of 20 Hz. The initial transient duration of 75 s was removed prior to any analysis.

Measurements in the swash zone pose particular problems for capacitance wave gauges due to the intermittent periods of essentially zero water depth. A wave gauge to measure the free surface in the swash zone was designed to overcome these difficulties. The instrument was secured to the plywood bottom and was moved along the center line in the wave basin between each run.

Table 2.2 lists the wave conditions at the seaward boundary $x = 0$ taken at the location of the middle gauge of the three fixed gauges as shown in Figure 2.9. The quantities tabulated are defined as those in Table 2.1 for the five calibration tests. The wave set-down is very small at $x = 0$ outside the surf zone. The measured

Table 2.2: Wave Conditions at Seaward Boundary and Breaker Parameter γ for Five Verification Tests

Test (1)	d (cm) (2)	$\overline{\eta}$ (cm) (3)	T_p (s) (4)	H_{rms} (cm) (5)	H_{inc} (cm) (6)	R (7)	γ (8)	x_i (m) (9)	x_s (m) (10)
6a	43.1	-0.13	1.54	8.12	8.90	0.23	0.76	12.39	12.93
6b	43.1	-0.17	1.54	9.01	9.73	0.25	0.78	12.54	12.93
7a	43.1	-0.24	2.58	10.14	10.26	0.24	0.62	10.78	12.93
7b	43.1	-0.29	2.57	11.25	11.11	0.25	0.63	10.88	12.93
8	43.1	-0.35	4.47	12.64	12.38	0.25	0.54	8.08	12.93

wave conditions at $x = 0$ include the slight effects of reflected waves. The incident and reflected waves at $x = 0$ were estimated using a three-gauge method in the same manner as tests 1–5. The reflection coefficient was in the narrow range $0.23 \leq R \leq 0.25$.

The measured values of $\overline{\eta}$, T_p, and H_{rms} at $x = 0$ listed in Table 2.2 are specified as input to CSHORE. Figures 2.10–2.12 demonstrate the accurate prediction of the cross-shore variation of root-mean-square wave height H_{rms}, wave setup $\overline{\eta}$, and free surface skewness s and kurtosis K. Data for two different incident root-mean-square wave heights are shown in the common Figures 2.10 and 2.11. The data and computed results shown indicate the saturation near the shoreline because the wave statistics are nearly independent of the incident wave height. The skewness s and kurtosis K are not specified as boundary conditions of the model, and therefore the model prediction of these higher order moments is marginal in the region affected by the mismatch of s and K at $x = 0$.

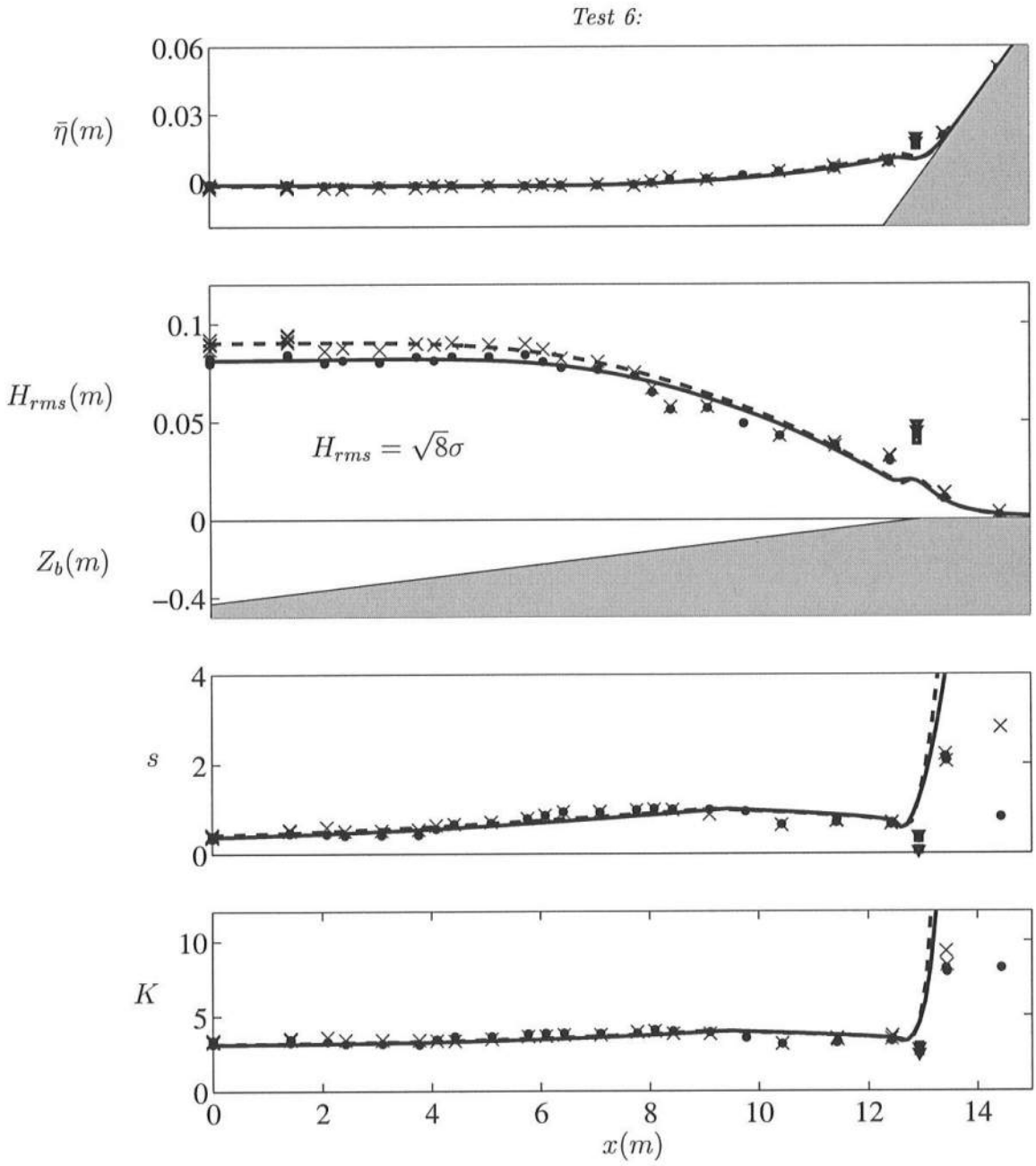

Figure 2.10: Cross-Shore Variations of Wave Setup $\bar{\eta}$, Root-Mean-Square Wave Height H_{rms}, Free Surface Skewness s and Kurtosis K: Model Prediction for Test 6a(——), and Test 6b (– – –); Measured Free Surface for Test 6a (•), and Test 6b (×); Measured Runup for Test 6a (□), and Test 6b (▽).

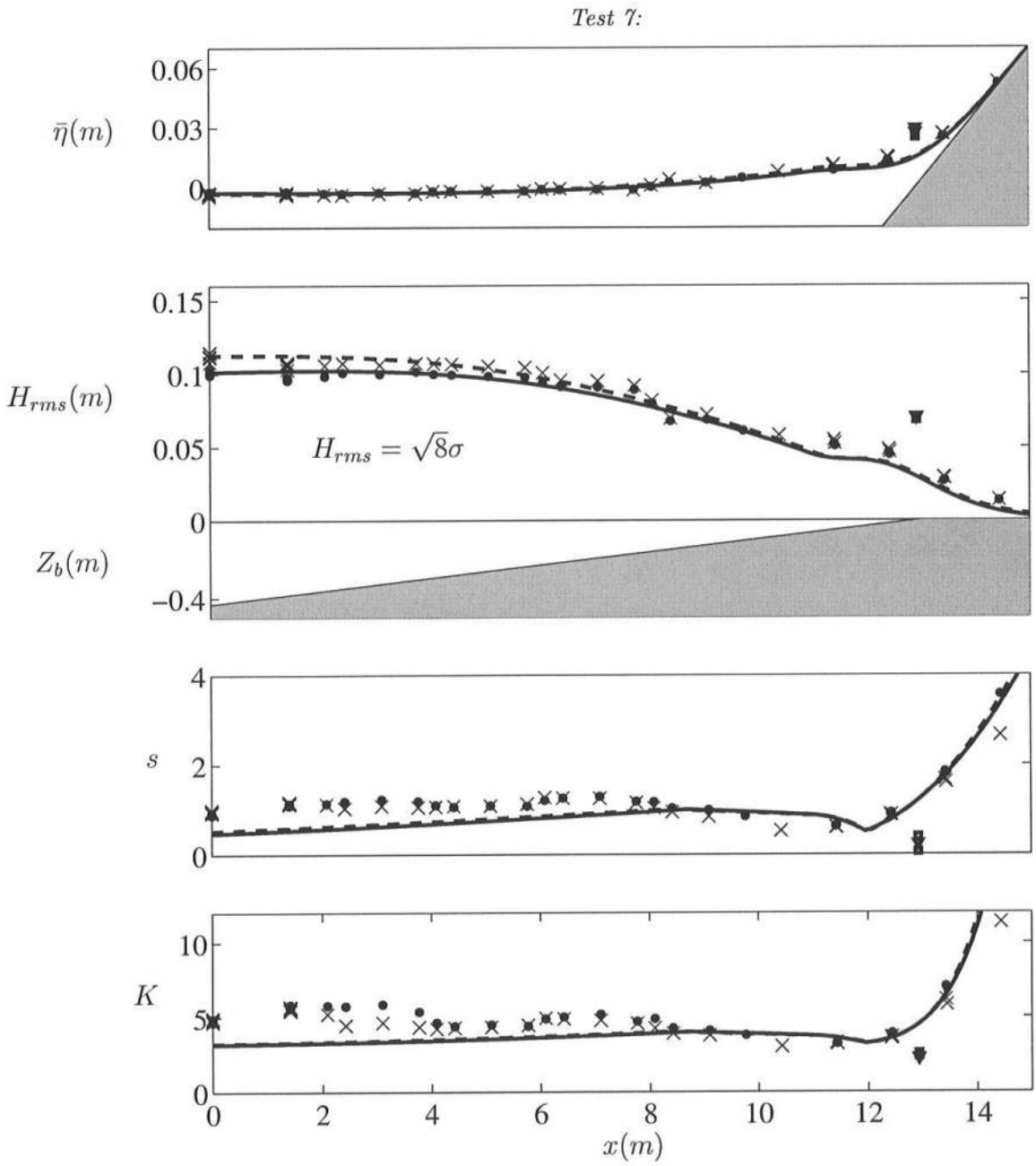

Figure 2.11: Cross-Shore Variations of Wave Setup $\bar{\eta}$, Root-Mean-Square Wave Height H_{rms}, Free Surface Skewness s and Kurtosis K: Model Prediction for Test 7a (———), and Test 7b (– – –); Measured Free Surface for Test 7a (•), and Test 7b (×); Measured Runup for Test 7a (□), and Test 7b (▽).

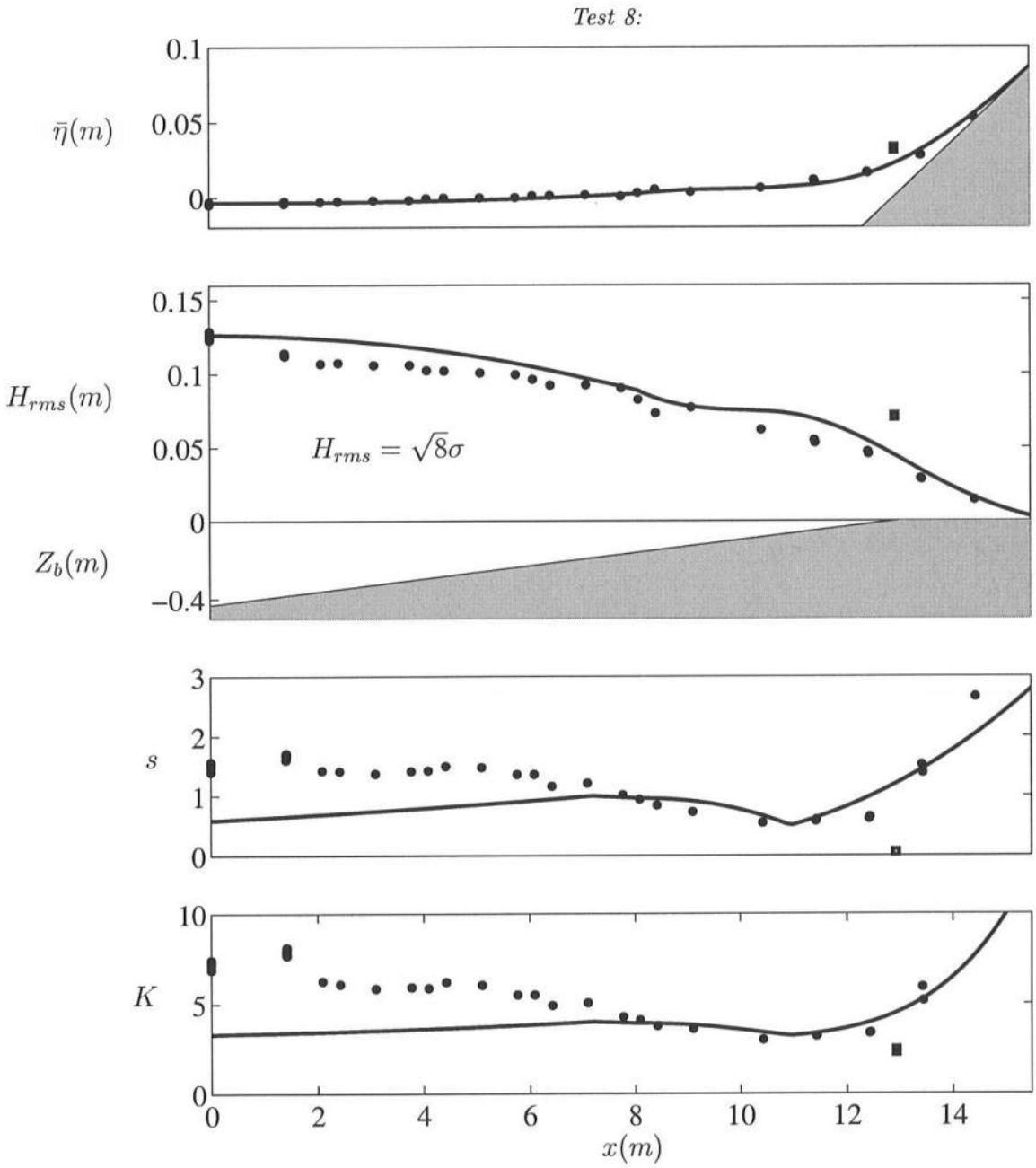

Figure 2.12: Cross-Shore Variations of Wave Setup $\bar{\eta}$, Root-Mean-Square Wave Height H_{rms}, Free Surface Skewness s and Kurtosis K: Model Prediction for Test 8 (——); Measured Free Surface for Test 8 (•); Measured Runup for Test 8 (□).

The statistical quantities of the measured runup time series are also plotted in each panel at the location of the still water shoreline although the location is arbitrary because the actual shoreline location as measured by the runup wire in Figure 2.9 varies with time. It is clear that the characteristics of the runup are markedly different from those of the free surface time series measured by a vertical wave gauge. The values of $H_{rms} = \sqrt{8}\sigma_r$, where σ_r = standard deviation of the shoreline elevation, shown in the second panel is relatively large because the shoreline freely oscillates; the vertical free surface motions at a fixed point, however, are limited by the bottom. Likewise, the mean shoreline elevation is higher than the setup $\bar{\eta}$. The skewness and kurtosis of the shoreline elevation are approximately Gaussian ($s = 0$ and $K = 3$) as observed by others [e.g., Holland and Holman (1993)], but the free surface elevation at a fixed location shows the landward increase of s and K as observed by Kobayashi *et al.* (1998). The measured runup data in Figure 2.10 (tests 6a and 6b) and in Figure 2.11 (tests 7a and 7b) indicate that the slightly larger incident wave height results in the slightly larger mean and standard deviation due to the un-saturated low frequency shoreline oscillations [e.g., Guza and Thorton (1982)].

Figure 2.13 is an example of the recorded time series of runup and free surface elevation η as measured by the bottom mounted swash gauge designed to measure the elevation of the free surface in the swash zone. The gauge was comprised of a frame to support a capacitance wire while minimizing the disturbance of the flow. The runup wire was stationary and therefore recorded a reproducible record for each of four runs. The swash gauge, however, was moved between runs. It was positioned in the still water depth of 5 and 2 cm for runs 1 and 2, respectively, while it was located 2 cm and 5 cm above SWL on the slope for runs 3 and 4, respectively. The free surface oscillations measured by the swash gauge decrease landward. The shoreline oscillations appear to be dominated by occasional large excursions lasting

Test 7a

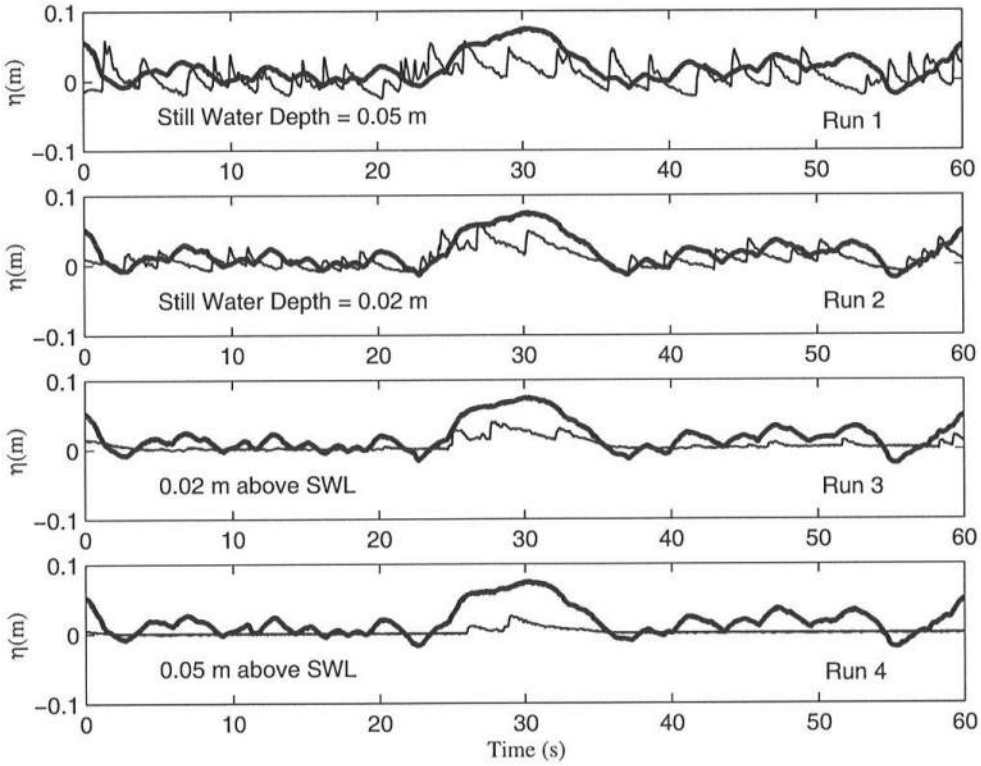

Figure 2.13: Free Surface Time-Series for Four Runs: Runup(——) and Swash Gauge (——).

for several waves. For example, the group of large waves occurring in the vicinity of $t = 30$ s in the free surface signal of η resulted in the large runup event lasting about 10 s.

The frequency spectra of the measured shoreline oscillations in Figure 2.14 indicate that the shoreline oscillations on the 1:30 slope are dominated by the low frequency components for all of the tests. Two tests are plotted together for tests 6 and 7 to show that the runup spectra are practically independent of incident wave height except for the very low frequency component.

Figure 2.15 compares the measured probability density function P of the normalized runup $\eta_* = (\eta_r - \overline{\eta_r})/\sigma_r$ where η_r = shoreline elevation above SWL, and $\overline{\eta_r}$ and σ_r = mean and standard deviation of η_r. Use is made of the exponential gamma distribution (Kobayashi *et al.* 1998) along with the measured skewness for each test. The exponential gamma distribution is capable of describing the measured probability distribution of the runup with relatively small skewness as measured by a wire placed parallel to the bottom. The distributions with large skewness measured by vertical gauges for tests 1–5 were already shown to be well represented by the exponential gamma distribution (Kobayashi *et al.* 1997b, 1998). CSHORE will need to be extended to predict the mean, standard deviation, and skewness of the shoreline elevation η_r in order to predict the exceedance probabilities of the shoreline elevation.

2.7 Independent Verification on Natural Beach

The pressure recordings from the storm on Jan. 28, 1998 collected at the Field Research Facility in Duck, NC were also used in verifying CSHORE. Data samples are available for the 24 hour period of January 28, 1998. The cases of largest and smallest water depth occurring at 7:00 (high tide) and 13:34 (low tide), respectively, on January 28, 1998, are analyzed in some detail in Johnson and Kobayashi (1998b). Time series from three pressure gauges mounted on the pier as well as bathymetry

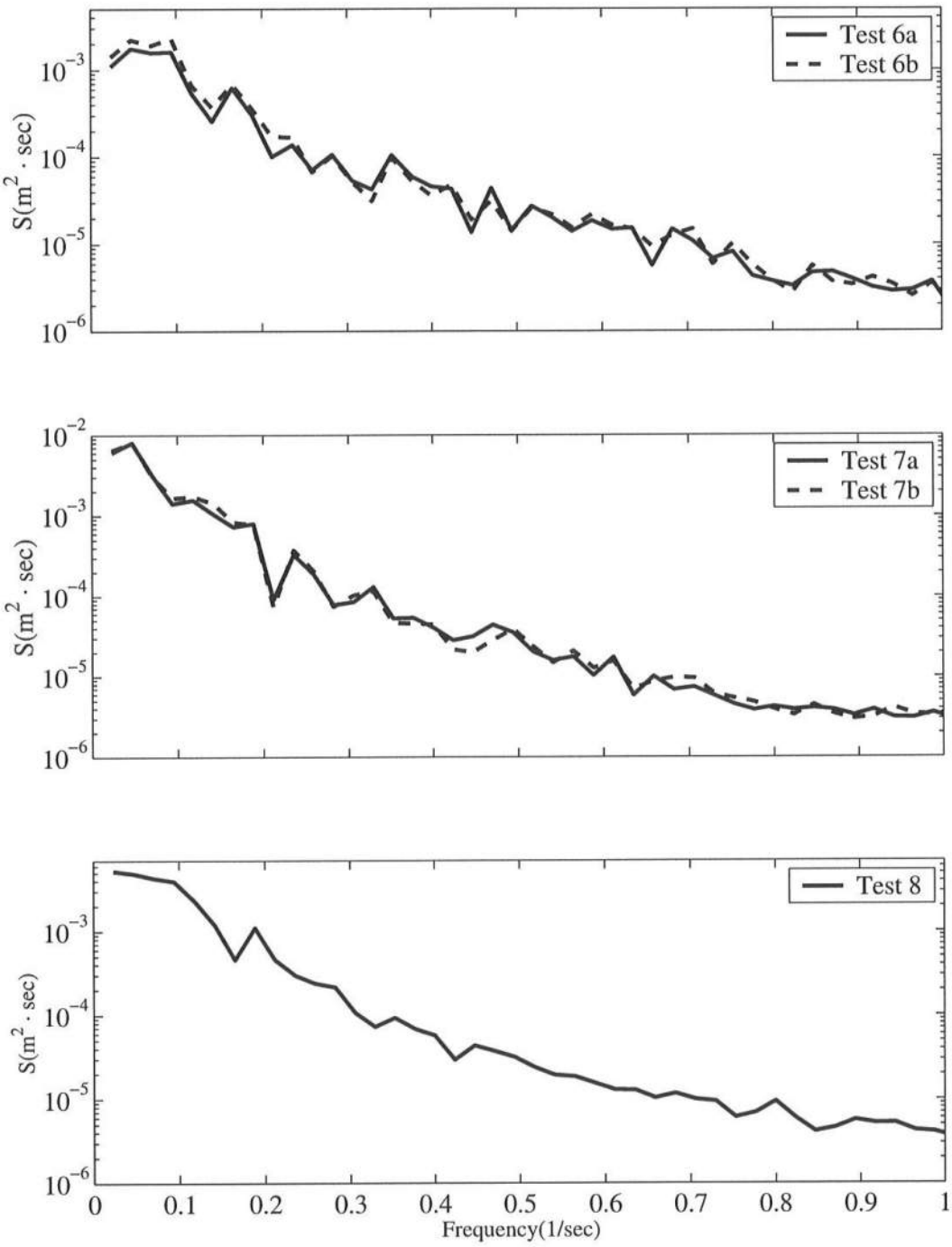

Figure 2.14: Power Spectral Density of Runup for Five Tests

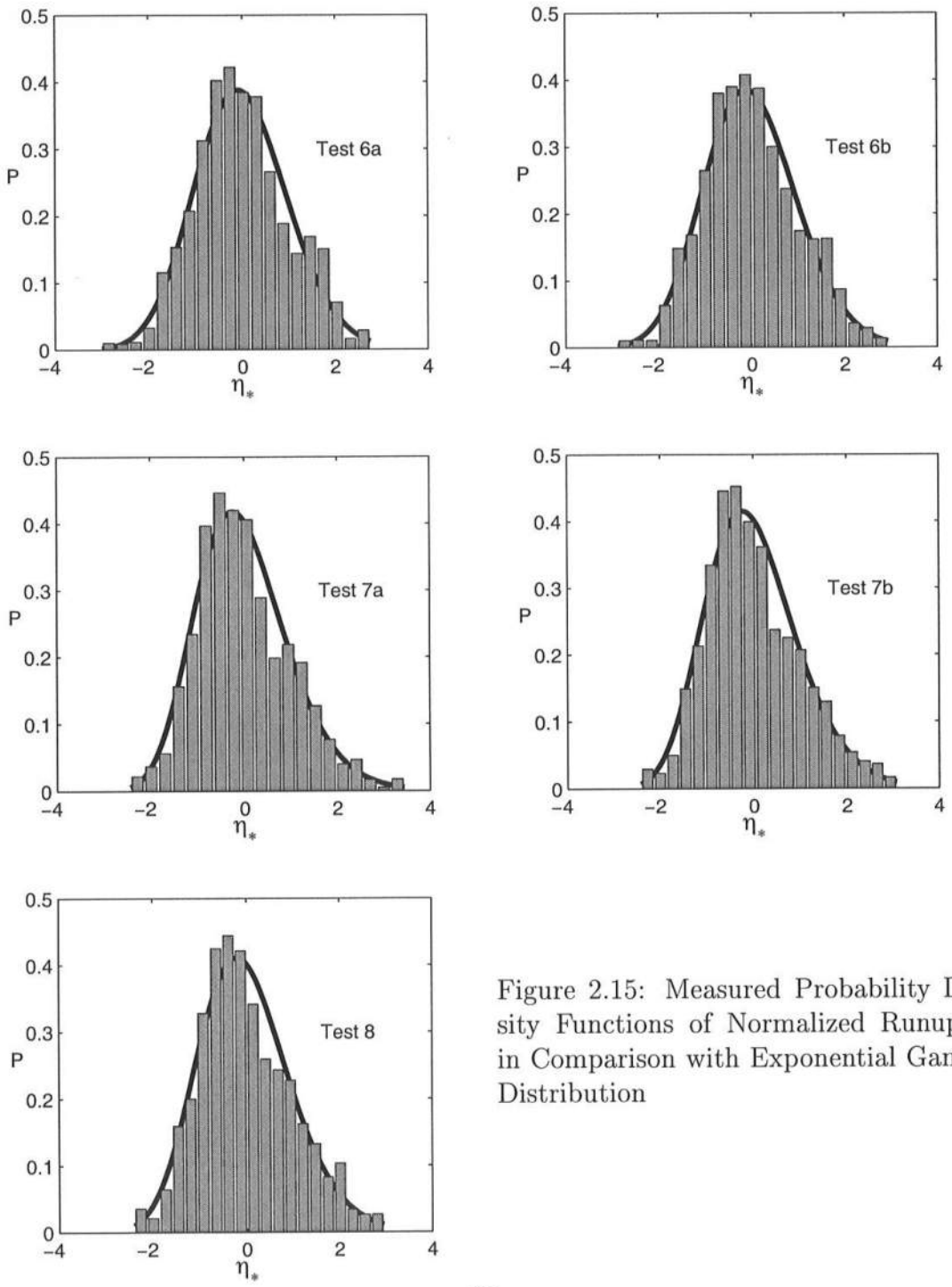

Figure 2.15: Measured Probability Density Functions of Normalized Runup η_* in Comparison with Exponential Gamma Distribution

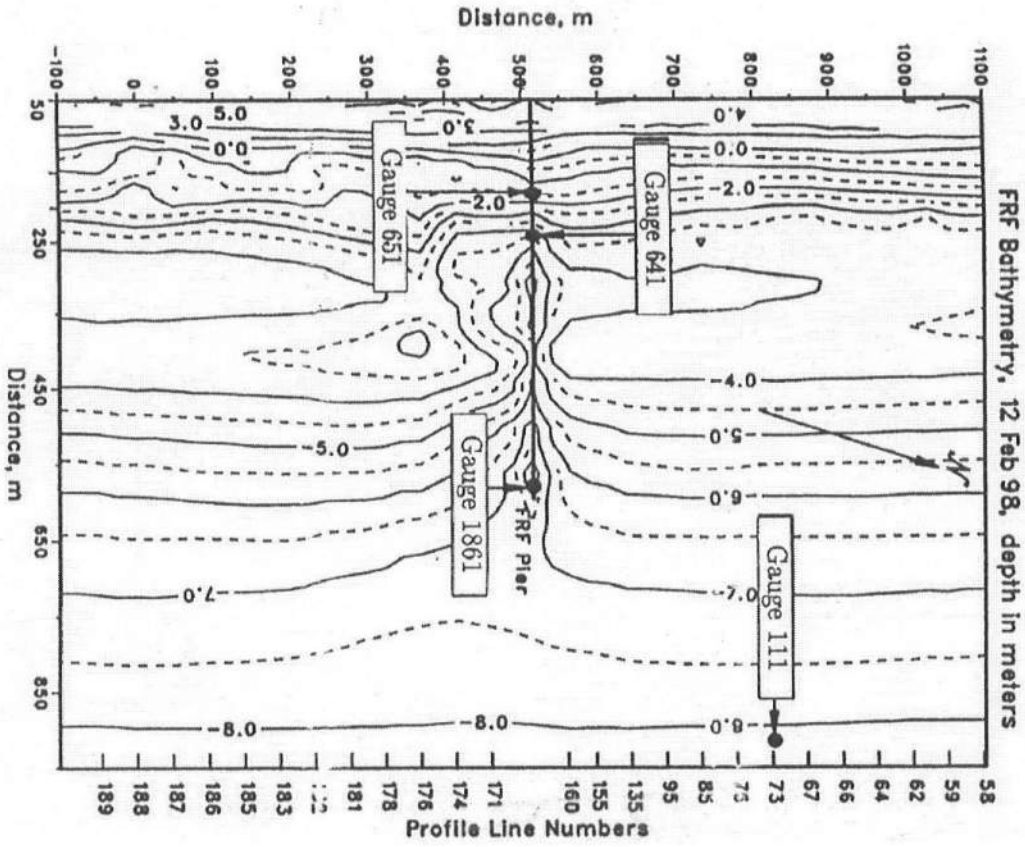

Figure 2.16: Bathymetry of the Area Surrounding the Pier.

Table 2.3: Locations of Four Gauges Deployed During SandyDuck Experiment.

Gauge	Cross-shore (m)	Longshore (m)	Deployment Position below NGVD (m)	Bottom Position below NGVD (m)
651	182.9	513.6	1.01	1.46
641	239.11	516.64	1.64	1.96
1861	566.9	516.6	8.17	8.57
111			7.49	7.9

Table 2.4: Wave Conditions at End of Pier during High and Low Tides

Test	$\bar{\eta}$ (m)	H_{rms} (m)	T_p (sec)
High Tide	0.13	1.71	11.63
Low Tide	0.16	1.67	12.8

taken as part of a larger study were used as shown in Figure 2.16. Table 2.3 indicates the cross-shore and long-shore position as well as the deployment depth relative to National Geodetic Vertical Datum (NGVD) of the three gauges used. Also, the bottom position is indicated relative to NGVD. The free surface elevation was derived from the pressure record using linear wave theory[e.g., Guza and Thorton 1980]. Figures 2.17 and 2.18 show the comparisons of the predicted root-mean-square wave height, setup, and skewness of the free surface with the measured data for the high tide and low tide conditions. The model is initiated at the end of the pier located at $x = 0$ with the measured wave conditions listed in Table 2.4.

The slight overprediction of the wave heights seen in Figures 2.17 and 2.18 are due in part to the application of the one-dimensional model when the assumption of normally incident waves on a long straight coast of longshore uniformity is questionable. Scour in the vicinity of the pier due to the effect of the piles was

clearly evident in the measured bathymetry shown in Figure 2.16. The depth of the scour was approximately 1 m and the level of the bottom along the pier was approximately 1 m below the bathymetry far from the pier. The scour hole may reduce the wave height through refraction. The bathymetry in the vicinity of the pier is expected to cause incoming wave energy to refract out and reduce the wave height at the positions where the pressure is measured.

Figure 2.19 shows the measured probability density function of the normalized free surface elevation $\eta_* = (\eta - \bar{\eta})/\sigma$ with $\sigma =$ the standard deviation of the free surface. The gauge locations are indicated in the third panel in Figures 2.17 and 2.18 and the values of H_{rms} listed in Figure 2.19 decrease landward. The exponential gamma distributions with the measured and predicted skewness are also plotted in Figure 2.19. The agreement is not very sensitive to the measured and predicted skewness. The tail of the skewed distribution for large η_* is predicted well. As a result, CSHORE combined with the exponential gamma distribution can be used, for example, to estimate the required deck clearance for piers.

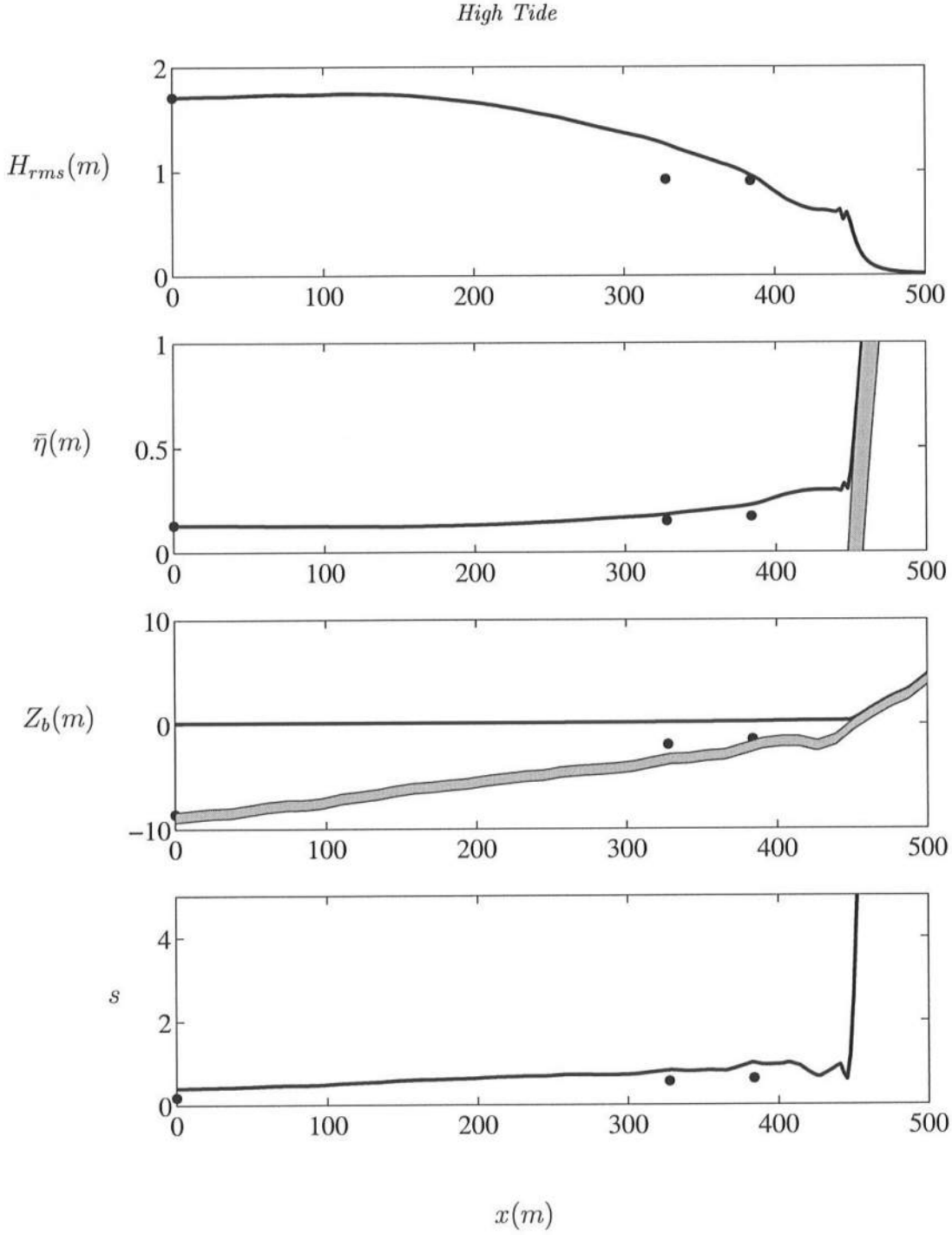

Figure 2.17: Cross-Shore Variations of Wave Height H_{rms}, Wave Setup $\bar{\eta}$, Bottom Elevation Z_b, and Skewness s: Model ——, Data •.

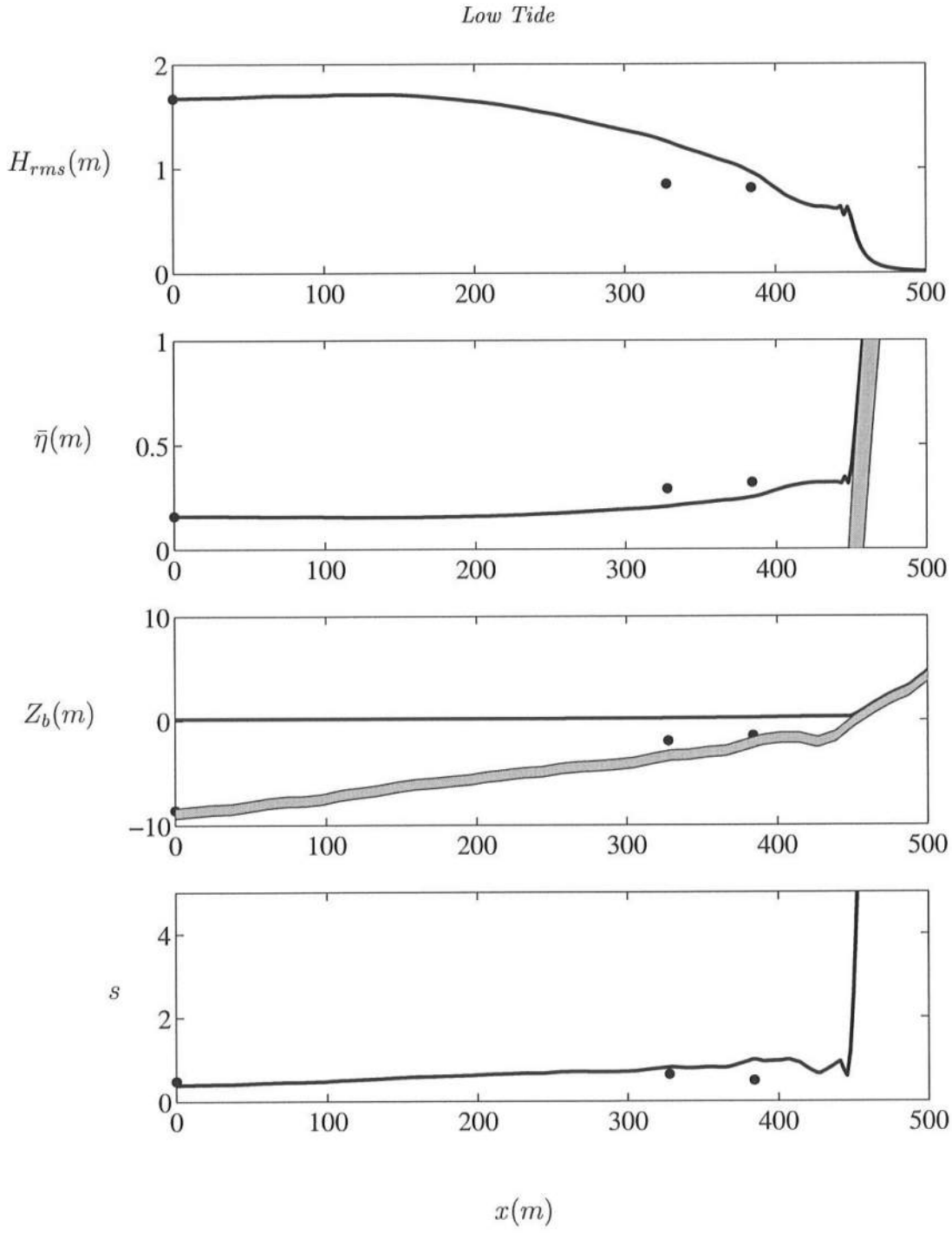

Figure 2.18: Cross-Shore Variations of Wave Height H_{rms}, Wave Setup $\bar{\eta}$, Bottom Elevation Z_b, and Skewness s: Model ——, Data •.

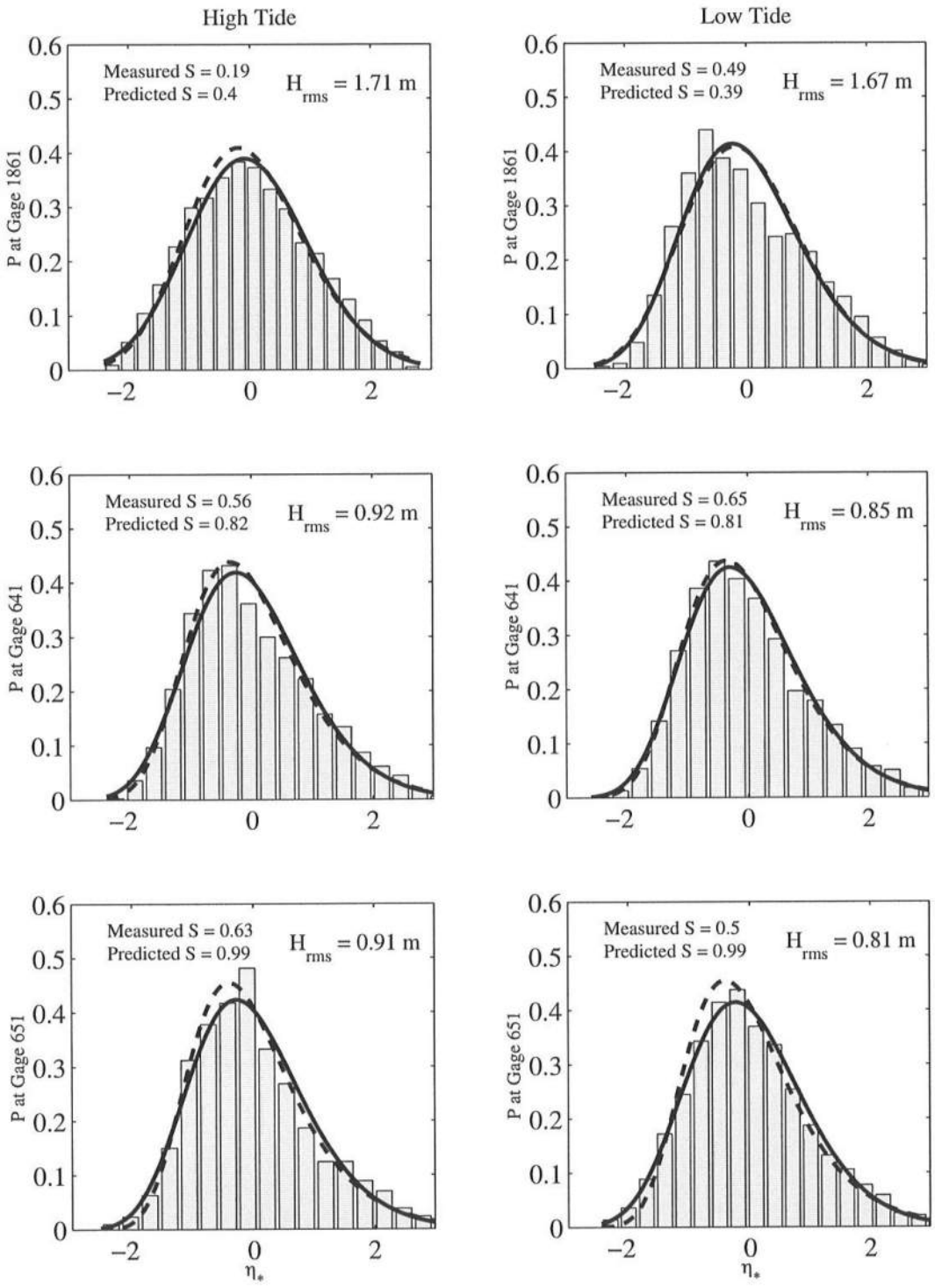

Figure 2.19: Probability Density Function of Normalized Free Surface Elevation η_*: Based on Predicted Skewness (– – –), Based on Measured Skewness (——)

Chapter 3

PROFILE EVOLUTION MODEL

3.1 Introduction

Existing models have some success in predicting the sediment dynamics involved in offshore (erosional) sediment transport [e.g. Dean (1991)]. However, it is more difficult to predict the accretional case where sand grains are deposited on beaches. A simple time-averaged model with moving boundary conditions at the shoreline and breaker point is shown to predict both erosional and accretional beach profile evolutions herein. Existing models assume that the local sediment transport rate is determined solely by the local hydrodynamic forcing and sediment characteristics without regard to cross-shore sediment advection. The net cross-shore sediment transport rate is generally the small difference between large onshore and offshore transport rates and may be affected by sediment advection from or into the surrounding areas. A new cross-shore sediment transport model is developed that includes sediment suspension by turbulence generated by wave breaking and bottom friction, sediment storage in the entire water column, sediment advection by waves and wave-induced currents, and sediment settling on the movable bed.

The cross-shore sediment transport is analyzed on the basis of the time-dependent, depth-integrated sediment continuity equation including sediment suspension, storage, advection and settling. The energetics approach by Bagnold (1966) is shown to correspond to the special case of local equilibrium between sediment suspension and settling. The corresponding time-averaged model together with the

simplified assumptions of Dean (1977) yields a uniform suspension rate for the standard equilibrium profile with the scale parameter A as a function of the sediment fall velocity. The simplified time-averaged model with new moving boundary conditions at the shoreline and breaker point is shown to predict both erosional and accretional beach profile evolutions under regular waves in a large tank. The sediment suspension rate estimated for the equilibrium terraced and barred beaches under irregular waves is found to be roughly uniform in the surf zone but increase significantly in the swash zone.

3.2 Formulation

3.2.1 Time-Dependent Sediment Continuity Equation

It is difficult and time-consuming to predict the vertical distributions of bed load and suspended load in surf zones. As a first attempt, the depth-integrated sediment continuity equation is expressed as

$$\frac{\partial}{\partial t}\left[\int_{z_b}^{\eta} c\, dz\right] + \frac{\partial}{\partial x}\left[\int_{z_b}^{\eta} cu\, dz\right] = S - w_f c_{z_b} \tag{3.1}$$

where t = time; x = cross-shore coordinate, positive onshore; c = volumetric sediment concentration; c_{z_b} = volumetric sediment concentration near the bottom elevation z_b; η = instantaneous free surface elevation; u = horizontal fluid velocity; S = upward sediment suspension rate from the bottom per unit horizontal area; and w_f = sediment fall velocity. The depth-averaged concentration C is defined as

$$C = \frac{1}{h}\int_{z_b}^{\eta} c\, dz \tag{3.2}$$

where $h = \eta - z_b$. and depth-averaged horizontal velocity U is defined as

$$U = \frac{1}{h}\int_{z_b}^{\eta} u\, dz \tag{3.3}$$

Substitution of (3.2) and (3.3) into (3.1) leads to

$$\frac{\partial}{\partial t}(hC) + \frac{\partial}{\partial x}(\alpha hCU) = S - w_f c_{z_b} \tag{3.4}$$

where the correction factor α is defined as

$$\alpha = \frac{1}{h}\int_{z_b}^{\eta}\left(\frac{u}{U}\frac{c}{C}\right)dz \tag{3.5}$$

If the horizontal sediment velocity u is assumed to be represented by U in the advection term, then $\alpha = 1$ is a reasonable approximation and is used in the following. However, experimental data is necessary to verify the accuracy of $\alpha = 1$. Assuming $c_{z_b} \simeq C$, (3.4) is rewritten as

$$\begin{array}{cccccc} \frac{\partial}{\partial t}(hC) & + & \frac{\partial}{\partial x}(hCU) & = & S & - & w_f C \\ \text{storage} & & \text{advection} & & \text{suspension} & & \text{settling} \end{array} \tag{3.6}$$

The concentration C in (3.6) includes both bed load and suspended load. The sediment storage term is exact for the depth-averaged concentration C, and the settling rate $w_f C$ per unit horizontal area is assumed to be determined by C.

The sediment suspension rate S in (3.6) in surf zones is uncertain but may be expressed as

$$S = < c'w' > \tag{3.7}$$

where $< c'w' >$ = ensemble-averaged upward sediment flux due to turbulence generated by wave breaking and bottom friction; c' = turbulent concentration fluctuation; and w' = turbulent vertical fluid velocity. To estimate $< c'w' >$, the transport equation for the turbulent kinetic energy k per unit mass [e.g., Tennekes and Lumley (1974)] may be approximated by

$$P + < b'w' > -\epsilon \simeq 0 \tag{3.8}$$

where P = production rate of k; $< b'w' >$ = destruction rate of k due to the negative buoyancy fluctuation b' due to suspended sediment; and ϵ = dissipation rate of k. The temporal change, advection and diffusion of k may be neglected relative to P and ϵ in (3.8) on the basis of the order-of-magnitude data analysis by Cox *et*

al. (1994b) for the case of no sediment. The negative buoyancy and concentration fluctuations are related by

$$b' = -(s-1)gc' \tag{3.9}$$

where s = sediment specific gravity; and g = gravitational acceleration. Substituting (3.9) into (3.8), the sediment suspension rate S expressed as (3.7) is given by

$$S \simeq \frac{P-\epsilon}{(s-1)g} \tag{3.10}$$

The net production rate $(P-\epsilon)$ of the turbulent kinetic energy per unit mass used for sediment suspension may be related to the local wave energy dissipation rates D_B and D_f per unit horizontal area due to wave breaking and bottom friction, respectively, in the following form:

$$P-\epsilon \simeq \frac{e_B D_B + e_f D_f}{\rho h} \tag{3.11}$$

where ρ = fluid density; and e_B and e_f = suspension efficiencies for the turbulence induced by wave breaking and bottom friction, respectively. Substitution of (3.11) into (3.10) yields

$$S \simeq \frac{e_B D_B + e_f D_f}{\rho g(s-1)h} \tag{3.12}$$

Admittedly, (3.12) is crude because the complicated suspension processes are taken into account through the empirical efficiencies e_B and e_f. Nevertheless, (3.6) and (3.12) are more general than the energetics approach by Bagnold (1966) who implicitly assumed $S \simeq w_f C$ in (3.6). This assumption of local equilibrium and (3.12) yield

$$\rho g(s-1)hCw_f \simeq e_B D_B + e_f D_f \tag{3.13}$$

The cross-shore sediment transport rate q_s per unit width can be obtained by substituting C from (3.13) into $q_s = hCU$. Eq. (3.13) implies that the rate of work required to keep the sediment suspended is approximately the same as the rate of

the dissipated fluid energy used for the sediment suspension. Bagnold (1966) considered the bottom friction only and suggested e_f on the order of 0.01. The energetics formula developed by Bailard (1981) was based on (3.13) with $D_B = 0$. Roelvink and Stive (1989) added the effect of D_B to this formula. However, the energetics approach based on (3.13) is valid only if the storage and advection terms in (3.6) are negligible.

The numerical model CBREAK is developed to compute $C(t, x)$ using (3.6) and (3.12) where the numerical model RBREAK (Kobayashi and Wurjanto 1992) is used to compute h, U, D_f and D_B. CBREAK is useful in examining the time-dependent mechanisms of sediment suspension, storage, advection and settling in the surf and swash zones, and the computed results are presented in Chapter 4. However, CBREAK requires considerable computation time to resolve the rapid temporal and spatial variations of breaking waves. A time-averaged cross-shore sediment transport model is developed using (3.6) and (3.12) to predict the beach profile evolution in more efficient but empirical manners.

3.2.2 Time-Averaged Sediment Continuity Equation

The time-averaged equations corresponding to (3.6) and (3.12) may be expressed as

$$\frac{\partial}{\partial x}\left(\overline{q}_s\right) = \overline{S} - w_f \overline{C} \tag{3.14}$$

$$\overline{S} \simeq \frac{e_B \overline{D}_B + e_f \overline{D}_f}{\rho g (s-1)\overline{h}} \tag{3.15}$$

with

$$\overline{q}_s = \overline{hCU} = \overline{hC}\,\overline{U} + \overline{(hC - \overline{hC})(U - \overline{U})} \tag{3.16}$$

where the overbar indicates time averaging. The net sediment transport rate $\overline{q}_s$ is the sum of the offshore (negative) and onshore (positive) transport rates. The time-averaged suspended sediment volume per unit area, $\overline{hC}$, is transported offshore by

the return current $\overline{U}$ which is negative and flows offshore. The oscillatory components $(hC - \overline{hC})$ and $(U - \overline{U})$ are positively correlated and cause onshore sediment transport because sediment particles suspended under the steep front of breaking waves tend to be transported onshore by the onshore wave velocity $(U - \overline{U})$.

The time-averaged sediment continuity equation (3.14) involves the two unknown variables $\overline{C}$ and $\overline{q}_s$ because the terms in (3.16) can not be expressed as a function of $\overline{C}$. The time-averaged suspension rate $\overline{S}$ given by (3.15) may be estimated using the time-averaged wave model CSHORE outlined in Chapter 2. This closure problem created by time averaging may be solved in various empirical manners. An empirical approach based on the concept of equilibrium beach profiles is proposed in the following.

For equilibrium beach profiles, $\overline{q}_s = 0$ and (3.14) and (3.15) yield

$$\overline{S}_e = w_f \overline{C}_e \simeq \frac{e_B}{\rho g(s-1)} \left(\frac{\overline{D}_B}{\overline{h}} \right)_e \tag{3.17}$$

where the subscript e indicates equilibrium and $\overline{D}_f$ may be neglected in (3.15) relative to $\overline{D}_B$ in surf zones. Dean (1977) assumed the uniformity of $(\overline{D}_B/\overline{h})_e$ across the surf zone on an equilibrium beach. This assumption and (3.17) together suggest that $\overline{S}_e$ and $\overline{C}_e$ may be assumed to be independent of x in the surf zone. In addition, the concentration $\overline{C}$ is intuitively assumed to be expressed as

$$\overline{C} = \frac{\beta \overline{S} + (1-\beta)\overline{S}_e}{w_f} \qquad \text{for} \quad 0 < \beta < 1 \tag{3.18}$$

where β = empirical parameter in the range $0 < \beta < 1$ so that $\overline{C} > 0$ for $\overline{S} > 0$ and $\overline{S}_e > 0$. The empirical relationship (3.18) yields $(\overline{S} - w_f \overline{C}) = (1-\beta)(\overline{S} - \overline{S}_e)$ so that the net suspension rate is zero for the equilibrium beach. Substitution of (3.18) into (3.14) yields $\overline{q}_s$ in terms of $\overline{S}$ and $\overline{S}_e$. Admittedly, this procedure is not unique. Kriebel and Dean (1985) have assumed that the net offshore transport rate $(-\overline{q}_s)$ is proportional to $(\overline{S} - \overline{S}_e)$ in view of (3.15) with $\overline{D}_f = 0$ and (3.17). If their empirical formula is adopted, $\overline{C}$ can be obtained from (3.14).

3.2.3 Simple Model for Beach Profile Evolution

In the following, use is made of the simplest wave model in the surf zone adopted by Dean (1977) for his analysis of equilibrium beach profiles without any nearshore bar. Wave setup is neglected and $h = \overline{h}$ is the still water depth hereafter where the overbar is omitted in the following. The analysis is limited to the surf zone in the depth range $0 \leq h \leq h_b$ with h_b = breaker depth. The local breaking wave height is assumed to be γh with the empirical parameter $\gamma \simeq 0.8$. The time-averaged wave energy equation with $D_f = 0$ is expressed as

$$\frac{\partial}{\partial x} E_F = -D_B \tag{3.19}$$

where E_F is the time-averaged flux of wave energy. If the simplifying assumption of linear shallow-water wave theory is used, the energy flux is expressed as

$$E_F = \frac{1}{8} \rho g H^2 \sqrt{gh} \tag{3.20}$$

Substitution of $H = \gamma h$ into (3.20) yields

$$E_F = \frac{1}{8} \rho g \gamma^2 h^2 \sqrt{gh} \tag{3.21}$$

The use of (3.21) in (3.19) yields

$$D_B = -\frac{5}{16} \rho g^{1.5} \gamma^2 h^{1.5} \frac{\partial h}{\partial x} \tag{3.22}$$

which is recast as

$$D_B = -\frac{5}{24} \rho g^{1.5} \gamma^2 h \frac{\partial}{\partial x} (h^{1.5}) \tag{3.23}$$

Substitution of (3.23) into (3.15) with $D_f = 0$ yields the time-averaged sediment suspension rate

$$S = -\frac{5 e_B \sqrt{g} \gamma^2}{24(s-1)} \frac{\partial}{\partial x} (h^{1.5}) \tag{3.24}$$

Substitution of (3.24) into (3.17) for constant C_e yields the equilibrium profile in the form

$$h = A(x_{oe} - x)^{2/3} \quad \text{for} \quad h = 0 \quad \text{at} \quad x = x_{oe} \tag{3.25}$$

with

$$A = \left[\frac{24(s-1)C_e}{5e_B\gamma^2}\right]^{2/3} \left(\frac{w_f^2}{g}\right)^{1/3} \tag{3.26}$$

Dean (1991) proposed $A = 0.067\ w_f^{0.44}$ where the units for A and w_f are $m^{1/3}$ and cm/s, respectively. On the other hand, Kriebel *et al.* (1991) proposed $A = 2.25(w_f^2/g)^{1/3}$ which has homogeneous units. The difference between the two formulas for A is less than 30% for sands with w_f = 1–10 cm/s. Equating (3.26) and the latter formula, $C_e = 0.7\gamma^2 e_B/(s-1)$ which yields $C_e/e_B \simeq 0.3$ for $\gamma \simeq 0.8$ and $s \simeq 2.6$. To obtain better agreement with data, A is regarded as a calibration parameter. Substitution of C_e obtained from (3.26) into (3.17) yields the equilibrium suspension rate

$$S_e = \frac{5e_B\sqrt{g}\ \gamma^2 A^{1.5}}{24(s-1)} \tag{3.27}$$

Substituting (3.24) and (3.27) into (3.18), the time-averaged sediment concentration is given by

$$C = \frac{5e_B\sqrt{g}\ \gamma^2}{24(s-1)w_f}\left[(1-\beta)A^{1.5} - \beta\frac{\partial}{\partial x}(h^{1.5})\right] \tag{3.28}$$

Substitution of (3.24) and (3.28) into (3.14) yields the time-averaged sediment transport rate $\overline{q}_s = q$ for brevity

$$\frac{\partial q}{\partial x} = -\frac{5e_B(1-\beta)\sqrt{g}\ \gamma^2}{24(s-1)}\left[\frac{\partial}{\partial x}(h^{1.5}) + A^{1.5}\right] \tag{3.29}$$

To predict the temporal variation of the still water depth h, use is made of the continuity equation of bottom sediment

$$(1-n_p)\frac{\partial h}{\partial t} = \frac{\partial q}{\partial x} \tag{3.30}$$

where t = morphological time for the profile evolution; and n_p = bottom sediment porosity. Solving (3.29) and (3.30) with appropriate initial and boundary conditions yields $h(t,x)$ and $q(t,x)$ in the region of $0 \le h \le h_b$. The governing equation for h obtained from (3.29) and (3.30) turns out to be a wave equation because of the

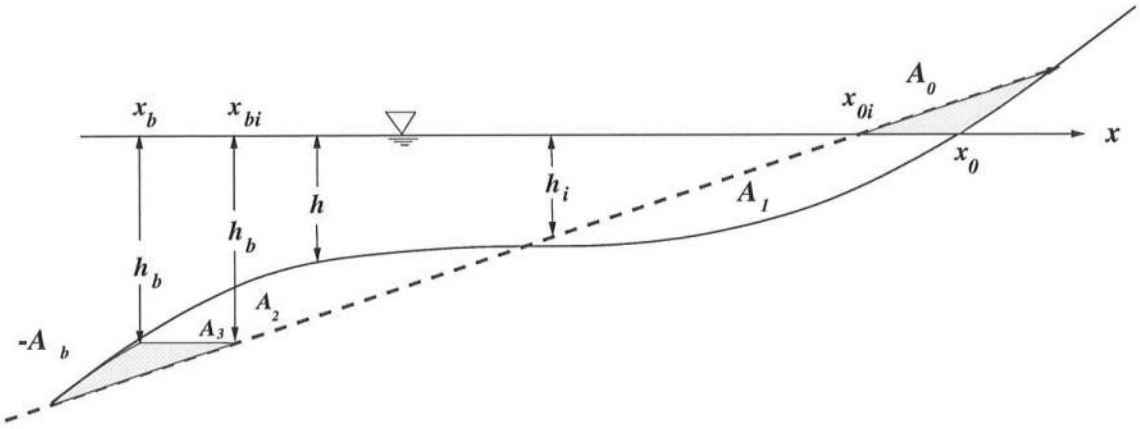

Figure 3.1: Definition Sketch

assumption of (3.18). If the assumption made by Kriebel and Dean (1985) is adopted instead of (3.18), the governing equation for h is a diffusion equation as shown by Kobayashi (1987).

The location of the shoreline where $h = 0$ varies with time t and is denoted by $x_o(t)$ and is shown in Figure 3.1. The breaker location where $h = h_b$ also varies with time and is denoted by $x_b(t)$. The subscripts o and b indicate the values at $h = 0$ and h_b, respectively. The initial condition for h is expressed as

$$h = h_i(x) \qquad \text{for} \quad t = 0 \quad \text{and} \quad x_{bi} \leq x \leq x_{oi} \tag{3.31}$$

where h_i is the initial still water depth corresponding to the initial beach profile specified as input and the subscript i indicates the initial values at $t = 0$.

The eroded (accreted) area above the still water level denoted by A_o is bounded by the initial beach profile, the eroded (accreted) profile, and the still water level as shown in Figure 3.1. The eroded (accreted) area at the seaward boundary, A_b, is bounded by the initial profile, the eroded (accreted) profile and the constant breaker depth h_b. It is noted that A_o and A_b are taken to be positive for erosion. Figure 3.1 demonstrates the case of $A_o > 0$ (erosional) and $A_b < 0$

(accretional) where sand is eroded at the still water line and deposited offshore. To avoid the complexities of detailed analyses for sediment transport above the still water line and beyond x_b, A_o and A_b are assumed to be given by

$$A_o = d_o(x_o - x_{oi}) \quad ; \quad A_b = d_b(x_b - x_{bi}) \tag{3.32}$$

where d_b and d_o = height of eroded or accreted area below the breaker depth and above the still water level, respectively. If x_o is larger (smaller) than x_{oi}, the shoreline moves onshore (offshore) and the eroded area A_o is positive (negative). If x_b is larger (smaller) than x_{bi}, the breaker point moves onshore (offshore) and the eroded area A_b is positive (negative). The translations of the breaker and shoreline locations result from the sediment transport at these locations. The sediment volume balance at these moving boundaries may be expressed as

$$q_b = (1-n_p)\frac{dA_b}{dt} \quad \text{at} \quad x = x_b(t) \quad \text{and} \quad h = h_b \tag{3.33}$$

$$q_o = -(1-n_p)\frac{dA_o}{dt} \quad \text{at} \quad x = x_o(t) \quad \text{and} \quad h = 0 \tag{3.34}$$

Substitution of (3.32) leads to

$$q_b = (1-n_p)d_b\frac{dx_b}{dt} \quad \text{at} \quad x = x_b(t) \quad \text{and} \quad h = h_b \tag{3.35}$$

$$q_o = -(1-n_p)d_o\frac{dx_o}{dt} \quad \text{at} \quad x = x_o(t) \quad \text{and} \quad h = 0 \tag{3.36}$$

The cross-shore sediment transport rates q_b and q_o in (3.35) and (3.36) are related to h through (3.29). The onshore (offshore) translation of the breaker location in (3.35) is caused by the onshore (offshore) sediment transport from (into) the region seaward of the breaker. On the other hand, the onshore (offshore) translation of the shoreline in (3.36) is caused by the offshore (onshore) sediment transport from (into) the region landward of the shoreline. The heights d_b and d_o need to be specified as input because the regions $x < x_b$ and $x > x_o$ are not analyzed here.

Conservation of sediment dictates that the eroded area match the deposited area as depicted in Figure 3.1

$$-A_b + A_2 + A_3 = A_o + A_1 \tag{3.37}$$

where

$$A_2 - A_1 = \int_{x_{bi}}^{x_{oi}} h_i \, dx - \int_{x_{bi}}^{x_o} h \, dx \tag{3.38}$$

$$A_3 = \int_{x_b}^{x_{bi}} (h_b - h) \, dx = h_b(x_{bi} - x_b) - \int_{x_b}^{x_{bi}} h \, dx \tag{3.39}$$

Substituting (3.38) and (3.39) into (3.37) yields

$$\int_{x_b}^{x_o} h \, dx + A_o + A_b + h_b(x_b - x_{bi}) = \int_{x_{bi}}^{x_{oi}} h_i \, dx \tag{3.40}$$

Along with (3.32), this can be rewritten as

$$\int_{x_b}^{x_o} h dx + d_o(x_o - x_{oi}) + (d_b + h_b)(x_b - x_{bi}) = \int_{x_{bi}}^{x_{oi}} h_i dx \tag{3.41}$$

which includes the volume changes due to the boundary displacements $(x_o - x_{oi})$ and $(x_b - x_{bi})$.

3.3 Semi-Analytical Solution

A semi-analytical solution is obtained for the case where the parameters h_b, γ, e_B, β, n_p, s, A, d_b and d_o are constant and the initial beach slope m is constant with $h_i = m(x_{oi} - x)$ in (3.31). It is convenient to introduce the following normalized variables:

$$t^* = \frac{t}{t_m} \quad ; \quad x^* = \frac{x}{L_e} \quad ; \quad h^* = \frac{h}{h_b} \quad ; \quad q^* = \frac{qt_m}{(1-n_p)h_b L_e} \tag{3.42}$$

$$d_b^* = \frac{d_b}{h_b} \quad ; \quad d_o^* = \frac{d_o}{h_b} \quad ; \quad m^* = \frac{mL_e}{h_b} \tag{3.43}$$

with

$$L_e = \left(\frac{h_b}{A}\right)^{1.5} \quad ; \quad t_m = \frac{24(s-1)(1-n_p)}{5 \, e_B(1-\beta)\gamma^2} \quad \frac{L_e}{\sqrt{gh_b}} \tag{3.44}$$

where L_e = surf zone width of the equilibrium profile given by (3.25); and t_m = beach profile evolution time scale.

Substitution of (3.42)–(3.44) into (3.29)–(3.31), (3.35), and (3.36) yields

$$\frac{\partial q^*}{\partial x^*} = -\frac{\partial}{\partial x^*}(h^*)^{1.5} - 1 \tag{3.45}$$

$$\frac{\partial h^*}{\partial t^*} = -\frac{\partial}{\partial x^*}(h^*)^{1.5} - 1 \tag{3.46}$$

$$h_i^* = m^*(x_{oi}^* - x^*) \quad \text{at} \quad t^* = 0 \quad \text{and} \quad x_{bi}^* \le x^* \le x_{oi}^* \tag{3.47}$$

$$q_b^* = d_b^* \frac{dx_b^*}{dt^*} \quad \text{at} \quad x^* = x_b^* \quad \text{and} \quad h^* = 1 \tag{3.48}$$

$$q_o^* = -d_o^* \frac{dx_o^*}{dt^*} \quad \text{at} \quad x^* = x_o^* \quad \text{and} \quad h^* = 0 \tag{3.49}$$

The normalized parameters involved in these equations are m^*, d_b^*, d_o^* and x_{oi}^* where $x_{bi}^* = (x_{oi}^* - 1/m^*)$ using (3.47). Integration of (3.45) with respect to x^* yields

$$q^* = q_o^* - (h^*)^{1.5} + x_o^* - x^* \tag{3.50}$$

where use is made of $q^* = q_o^*$ at $x^* = x_o^*$ and $h^* = 0$. Since $q^* = q_b^*$ at $x^* = x_b^*$ and $h^* = 1$, (3.50) requires

$$q_b^* = q_o^* - 1 + x_o^* - x_b^* \tag{3.51}$$

Substitution of (3.48) and (3.49) into (3.51) yields

$$d_b^* \frac{dx_b^*}{dt^*} + d_o^* \frac{dx_o^*}{dt^*} = x_o^* - x_b^* - 1 \tag{3.52}$$

Solving (3.46) with (3.47) and (3.52), $h^*(t^*, x^*)$ with $0 \le h^* \le 1$ for $t^* \ge 0$ and $x_b^*(t^*) \le x^* \le x_o^*(t^*)$ can be derived as shown in the following. Then, q_o^* and q_b^* can be obtained using (3.49) and (3.51), respectively, and $q^*(t^*, x^*)$ is given by (3.50).

The steady (equilibrium) solution for (3.46) is expressed as

$$h_e^* = (x_{oe}^* - x^*)^{2/3} \qquad \text{for} \qquad x_{be}^* \le x^* \le x_{oe}^* \tag{3.53}$$

where $h_e^* = 1$ at $x^* = x_{be}^* = (x_{oe}^* - 1)$. The normalized equation (3.53) corresponds to (3.25). To find the equilibrium shoreline location x_{oe}^*, (3.41) is normalized using (3.42)–(3.44)

$$\int_{x_b^*}^{x_o^*} h^* dx^* + d_o^*(x_o^* - x_{oi}^*) + (d_b^* + 1)(x_b^* - x_{bi}^*) = \int_{x_{bi}^*}^{x_{oi}^*} h_i^* dx^* \tag{3.54}$$

which is valid for arbitrary profiles h^* and h_i^*. Substituting (3.47) and (3.53) for h_i^* and h_e^* in (3.54), we obtain

$$\frac{3}{5} + d_o^*(x_{oe}^* - x_{oi}^*) + (d_b^* + 1)(x_{be}^* - x_{bi}^*) = \frac{1}{2m^*} \tag{3.55}$$

The displacement of the equilibrium breakerline relative to the initial location is given by

$$x_{be}^* - x_{bi}^* = (x_{oe}^* - x_{oi}^*) + (\frac{1}{m^*} - 1) \tag{3.56}$$

where use is made of (3.47) at $x^* = x_{be}^*$ and (3.53) at $x^* = x_{bi}^*$. The displacement of the equilibrium shoreline relative to the initial location is obtained from (3.56).

$$x_{oe}^* - x_{oi}^* = (x_{be}^* - x_{bi}^*) - (\frac{1}{m^*} - 1) \tag{3.57}$$

Substitution of (3.56) and (3.57) into (3.55), respectively, yields

$$x_{oe}^* - x_{oi}^* = \frac{4m^* - 5 + 10d_b^*(m^* - 1)}{10m^*(1 + d_o^* + d_b^*)} \tag{3.58}$$

$$x_{be}^* - x_{bi}^* = \frac{5 - 6\ m^* - 10d_o^*(m^* - 1)}{10\ m^*(1 + d_o^* + d_b^*)} \tag{3.59}$$

which are plotted in Figure 3.2 as a function of the normalized initial slope m^* defined in (3.43) for $0 \leq d_b^* \leq 0.5$ and $0 \leq d_o^* \leq 0.5$ which may be regarded as the expected range for d_o^* and d_b^*. The plotted variations of $(x_{oe}^* - x_{oi}^*)$ and $(x_{be}^* - x_{bi}^*)$ with respect to m^* are not sensitive to d_o^* and d_b^*. The shoreline displacement $(x_{oe}^* - x_{oi}^*)$ increases monotonically with the increase of m^* and becomes positive (shoreline erosion) for $m^* \gtrsim 1$. The breaker displacement $(x_{be}^* - x_{bi}^*)$ decreases monotonically with the increase of m^* and becomes negative (offshore displacement) for $m^* \gtrsim 1$.

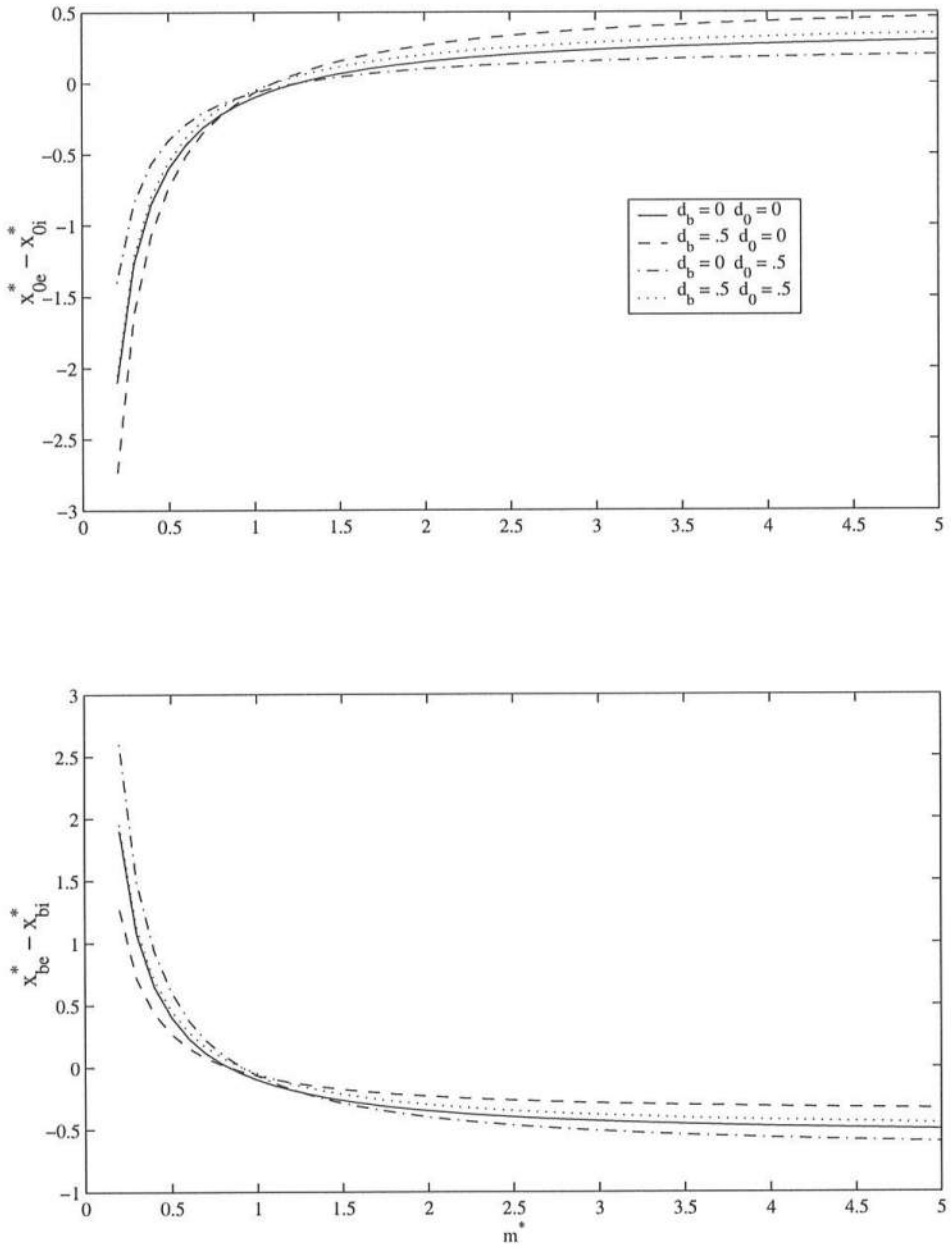

Figure 3.2: Displacements of the Equilibrium Shoreline and Breaker Locations Relative to Their Initial Locations

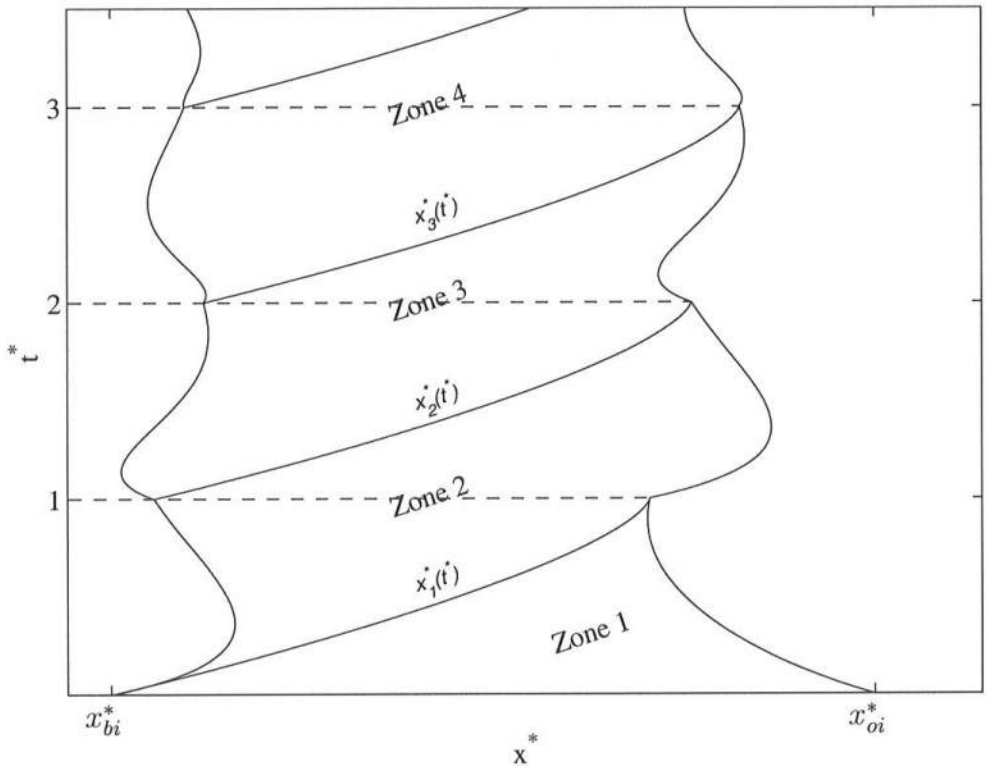

Figure 3.3: Example of Moving Shoreline, Breakerline and Characteristics

Since $m^* = m/(h_b/L_e)$, in (3.43), m^* can be regarded as the ratio between the initial slope m and the equilibrium slope h_b/L_e based on the breaker depth h_b and the equilibrium surf zone width L_e.

To predict the evolution from the initial profile (3.47) to the equilibrium profile (3.53), the wave equation (3.46) is expressed in the following characteristic form:

$$\frac{dh^*}{dt^*} = -1 \qquad \text{along} \qquad \frac{dx^*}{dt^*} = \frac{3}{2}\sqrt{h^*} \qquad \text{or} \qquad \frac{dx^*}{dh^*} = -\frac{3}{2}\sqrt{h^*} \tag{3.60}$$

which describes the variation of h^* along the characteristic path $x^*(t^*)$ propagating landward. Along the path, $dt^* = -dh^*$ and hence $dx^*/dh^* = -(3/2)\sqrt{h^*}$ which is

easier to integrate. To integrate (3.60) analytically, the plane (x^*, t^*) is separated into different zones depending on the origin of the characteristic path as shown in Figure 3.3 and explained in the following.

In zone 1, the characteristic path originates from the initial condition (3.47) at $t^* = 0$. Integration of (3.60) along the path starting from $(x_i^*,\ t^* = 0)$ where $h_i^* = m^*(x_{oi}^* - x_i^*)$ yields

$$x^*(h^*, t^*) = x_{oi}^* - \frac{h^* + t^*}{m^*} + (h^* + t^*)^{1.5} - (h^*)^{1.5} \tag{3.61}$$

which expresses x^* as a function of h^* and t^*. The landward boundary of zone 1 is the shoreline $(h^* = 0)$ located at

$$x_o^*(t^*) = x_{oi}^* - \frac{t^*}{m^*} + (t^*)^{1.5} \qquad \text{for} \quad 0 \le t^* \le 1 \tag{3.62}$$

The seaward boundary of zone 1 is the characteristic path $x_1^*(t^*)$ originating from the initial breaker location at $(x_{bi}^*,\ t^* = 0)$

$$x_1^*(t^*) = 1 + x_{bi}^* - (1 - t^*)^{1.5} \qquad \text{for} \quad 0 \le t^* \le 1 \tag{3.63}$$

The path x_1^* intersects the shoreline at $t^* = 1$ as shown in Figure 3.3. This intersection point is regarded as the upper bound of zone 1. It should be stated that x_1^* and x_o^* also becomes equal at a certain time $t^* < 1$ if $m^* > (2/3)$. The complication due to the double intersections is not considered in this analysis.

In the region of the plane (x^*, t^*) above the path $x_1^*(t^*)$, the characteristic path originates from the seaward boundary located at $x_b^*(t^*)$ which can be found from (3.52) for the known x_o^*. For x_o^* given by (3.62), (3.52) can be solved analytically.

$$\begin{aligned} x_b^*(t^*) \;=\; & x_o^*(t^*) - 1 + \frac{d_o^* + d_b^*}{m^*} - \left(x_{oi}^* - x_{bi}^* - 1 + \frac{d_o^* + d_b^*}{m^*} \right) \exp\left(-\frac{t^*}{d_b^*} \right) \\ & - \frac{3}{2} \left(d_b^* + d_o^* \right) \sqrt{d_b^*} \left[\sqrt{\frac{t^*}{d_b^*}} - F_D\left(\sqrt{\frac{t^*}{d_b^*}} \right) \right] \qquad \text{for} \quad 0 \le t^* \le 1 \end{aligned} \tag{3.64}$$

with

$$F_D(y) = \exp(-y^2) \int_0^y \exp(t^2) dt \tag{3.65}$$

where F_D is the Dawson's integral (Abramowitz and Stegun 1972). Since it is not possible to solve (3.52) analytically for $t^* > 1$, (3.52) is solved numerically using the following finite difference approximation based on $t^* = (n-1)\Delta t^*$ with $n = 1, 2, \cdots$, and $\Delta t^* =$ constant time step:

$$d_b^* \frac{(x_b^*)_{n+1} - (x_b^*)_n}{\Delta t^*} + d_o^* \frac{(x_o^*)_{n+1} - (x_o^*)_n}{\Delta t^*} = \frac{(x_o^*)_{n+1} + (x_o^*)_n}{2} - \frac{(x_b^*)_{n+1} + (x_b^*)_n}{2} - 1 \tag{3.66}$$

where the subscripts $(n+1)$ and n indicate the values at $t^* = n\Delta t^*$ and $(n-1)\Delta t^*$, respectively. Eq. (3.66) is solved for $(x_b^*)_{n+1}$ for the known $(x_o^*)_{n+1}$, $(x_o^*)_n$ and $(x_b^*)_n$ where $(x_b^*)_1 = x_{bi}^*$. For $0 < t^* \leq 1$, the computed values of $x_b^*(t^*)$ using (3.64) and (3.66) are compared and the difference is less than 0.0001 for $\Delta t^* = 0.01$ used here.

In zone j with $j = 2, 3, \cdots$, integration of (3.60) along the characteristic path originating from $x_b^*(t_b^*)$ with the specified t_b^* and $h^* = 1$ yields

$$h^* = 1 - t^* + t_b^* \qquad ; \qquad x^* = x_b^*(t_b^*) + 1 - (h^*)^{1.5} \tag{3.67}$$

which are combined to express x^* in terms of h^* and t^*

$$x^*(h^*, t^*) = x_b^*(h^* + t^* - 1) + 1 - (h^*)^{1.5} \tag{3.68}$$

where the value of x_b^* is evaluated for the value in its parentheses. The shoreline location for zone j can be found from (3.68) with $h^* = 0$.

$$x_o^*(t^*) = x_b^*(t^* - 1) + 1 \tag{3.69}$$

The upper bound of zone j is the path originating from $x_b^*(t_b^*)$ with $t_b^* = (j-1)$

$$x_j^*(t^*) = x_b^*(j-1) + 1 - (j - t^*)^{1.5} \tag{3.70}$$

The path x_j^* intersects the shoreline at $t^* = j$ in view of (3.69) and (3.70). As a result, zone j with $j = 2, 3, \cdots$ is bounded by $x_{j-1}^*(t^*)$ with $(j-2) \leq t^* \leq (j-1)$, $x_b^*(t^*)$ with $(j-2) \leq t^* \leq (j-1)$, $x_o^*(t^*)$ with $(j-1) \leq t^* \leq j$, and $x_j^*(t^*)$ with $(j-1) \leq t^* \leq j$.

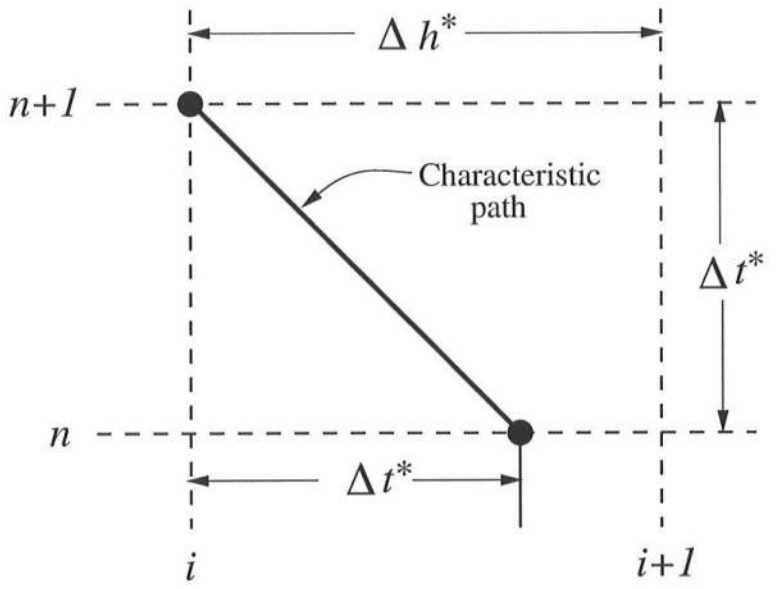

Figure 3.4: Numerical Solution

The computation is marched in time until $x_o^*(t^*)$ and $x_b^*(t^*)$ approach the equilibrium x_{oe}^* and x_{be}^* given by (3.58) and (3.59), respectively, within the error of 0.0001. For the actual computation, $x_o^*(t^*)$ and $x_b^*(t^*)$ are computed first using (3.62), (3.66) and (3.69). Second, $x_j^*(t^*)$ is calculated using (3.63) and (3.70). Third, $x^*(h^*, t^*)$ is computed using (3.61) and (3.68) where h^* in the range $0 \leq h^* \leq 1$ is discretized as $h^* = (i-1)\Delta h^*$ with $i = 1, 2, \cdots$, and $\Delta h^* = 0.02$ where the computed results are found to be essentially identical for $\Delta h^* = 0.01$ and 0.02.

To check the accuracy of the semi-analytical solution obtained without regard to the double intersections between $x_j^*(t^*)$ and $x_o^*(t^*)$ as described in relation to (3.62) and (3.63), (3.60) is also solved numerically using the finite difference grid with constant Δh^* and Δt^* shown in Figure 3.4. Along the characteristic path, $dh^* = -dt^*$ using (3.60) and the finite difference approximation of (3.60) between the two points at $(h_i^* + \Delta t^*,\ t_n^*)$ and $(h_i^*,\ t_{n+1}^*)$ is used in the time marching computation. The value of x^* at $(h_i^* + \Delta t^*,\ t_n^*)$ is linearly interpolated using $x_{i,n}^*$ and $x_{i+1,n}^*$ under

the condition of $\Delta t^* \leq \Delta h^*$

$$x^*_{i+\Delta t^*,n} = \left(1 - \frac{\Delta t^*}{\Delta h^*}\right) x^*_{i,n} + \frac{\Delta t^*}{\Delta h^*} x^*_{i+1,n} \tag{3.71}$$

where $x^*_{i,n}$ =value of x^* at $h^*_i = (i-1)\Delta h^*$ and $t^*_n = (n-1)\Delta t^*$. The finite difference representation of $dx^* = -d(h^*)^{1.5}$ along the characteristic path yields

$$x^*_{i,n+1} - x^*_{i+\Delta t^*,n} = -\left[(h^*)^{1.5}_i - (h^*_i + \Delta t)^{1.5}\right] \tag{3.72}$$

Substitution of (3.71) into (3.72) yields

$$x^*_{i,n+1} = \left(1 - \frac{\Delta t^*}{\Delta h^*}\right) x^*_{i,n} + \frac{\Delta t^*}{\Delta h^*} x^*_{i+1,n} + (h^*_i + \Delta t)^{1.5} - (h^*_i)^{1.5} \tag{3.73}$$

The initial values of $x^*_{i,1}$ at $t^*_1 = 0$ are known from the specified initial beach profile. The shoreline location $(x^*_o)_{n+1} = x^*_{1,n+1}$ can be found from (3.73) with $i = 1$. The breaker location $(x^*_b)_{n+1} = x^*_{I,n+1}$ with $h^*_I = (I-1)\Delta h^* = 1$ is calculated using (3.66). The numerical and semi-analytical solutions for $\Delta t^* = 0.01$ are found to be slightly different for $\Delta h^* = 0.02$ but indistinguishable for $\Delta h^* = 0.01$. The computed results presented in the following are based on the semi-analytical solution.

3.4 Comparison with Profile Evolution Data

Comparison is made with the regular wave data from large scale wave tank experiments conducted by Thorndike Saville at the Coastal Engineering Research Center during 1956–1957 and 1962. The data were retrieved and reported by Kraus and Larson (1988). The initial beach slope was approximately 1:15 where $m = 1/15$ is used in the semi-analytical solution. The median sand diameter d_{50} was 0.22 or 0.40 mm. The sand specific gravity was $s = 2.65$. The sand porosity is assumed as $n_p = 0.4$ here. Three cases for accretional, erosional and neutral shoreline changes are selected as listed in Table 3.1. The wave period T, the breaker depth h_b, the ratio $\gamma = H_b/h_b$ with H_b = breaker height, and the sediment fall velocity w_f for each case are listed in Table 3.1. Use is made of the average values of the measured H_b and h_b which varied somewhat during each test.

Table 3.1: Comparison of Semi-Analytical Solution with Three Cases

Case	Shoreline Change	T (s)	h_b (m)	γ	w_f (cm/s)	$A(m^{1/3})$ Emp.	$A(m^{1/3})$ Cal.	m^*	L_e (m)	t_m (hr)
201	accretion	11.33	1.36	1.42	5.9	0.15	0.23	0.71	14.4	2.6
500	erosion	3.75	1.60	1.19	3.1	0.11	0.10	2.67	63.9	15.0
801	neutral	3.75	0.75	0.91	5.9	0.15	0.15	0.99	11.2	6.5

The beach profile evolution predicted by the semi-analytical solution is sensitive to the parameter A for the equilibrium profile (3.25) but is not sensitive to $e_B(1-\beta)$ in (3.44) and d_b^* and d_o^* in (3.43). It is simply assumed that $e_B(1-\beta) = 0.001$, $d_b^* = 0.4$ and $d_o^* = 0.2$ as typical values. The calibrated A and the empirical $A = 0.067\ w_f^{0.44}$ (Dean 1991) for each case are listed in Table 3.1. The calibrated and empirical values of A are in good agreement except for case 201. Table 3.1 also lists the normalized initial slope m^* defined in (3.43) as well as the equilibrium surf zone width L_e and the morphological time scale t_m defined in (3.44). The shoreline change becomes more erosional (accretional) with the increase (decrease) of m^* from unity as explained in relation to (3.58). The predicted beach profile becomes essentially equilibrium after the duration of regular wave action on the order of 10 t_m. The analysis of Dalrymple (1992) showed that the use of a profile parameter $P = (gH_0^2)/(w_f^3 T)$, based on the deep water wave height H_0, is useful in the prediction of the trend of the beach profile evolution. For values of $P > (9,000 - 10,400)$, barred (erosional) profiles were observed, while normal (accretional) beach profiles were observed for smaller values of P. The values of the profile parameter P are 894, 240,000, and 8,774 for cases 201, 500, and 801, respectively. The profile parameter is independent of time and does not account for the initial beach slope. Nevertheless, the profile parameter accurately indicates the accretional and erosional trends for cases 201 and 500, respectively, as well as the profile of small change in case 801.

Figures 3.5–3.7 show the comparisons of the measured and predicted beach profiles for the three cases where $x = 0$ is taken at the still water shoreline on the

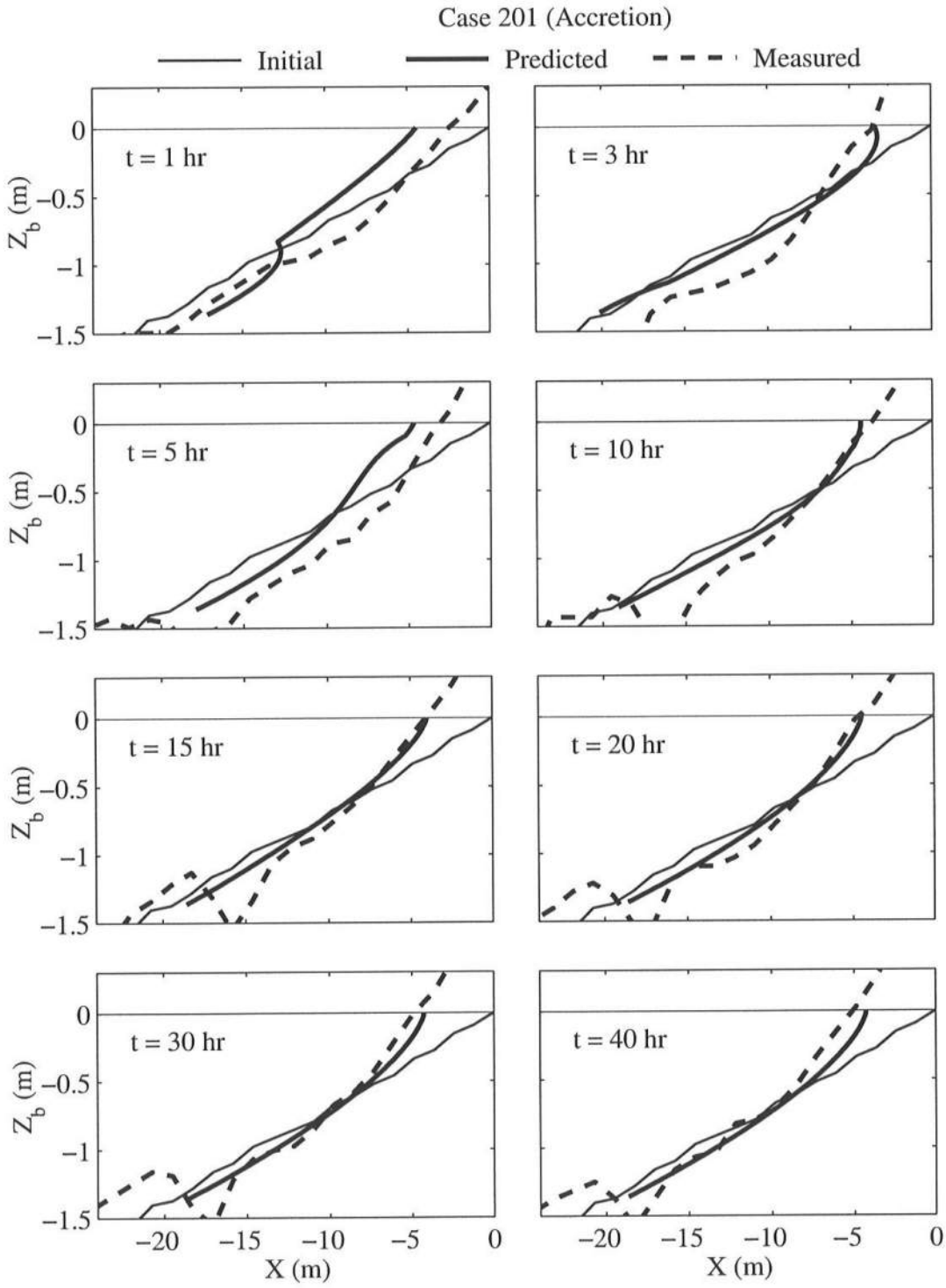

Figure 3.5: Measured and Predicted Beach Profiles for Case 201.

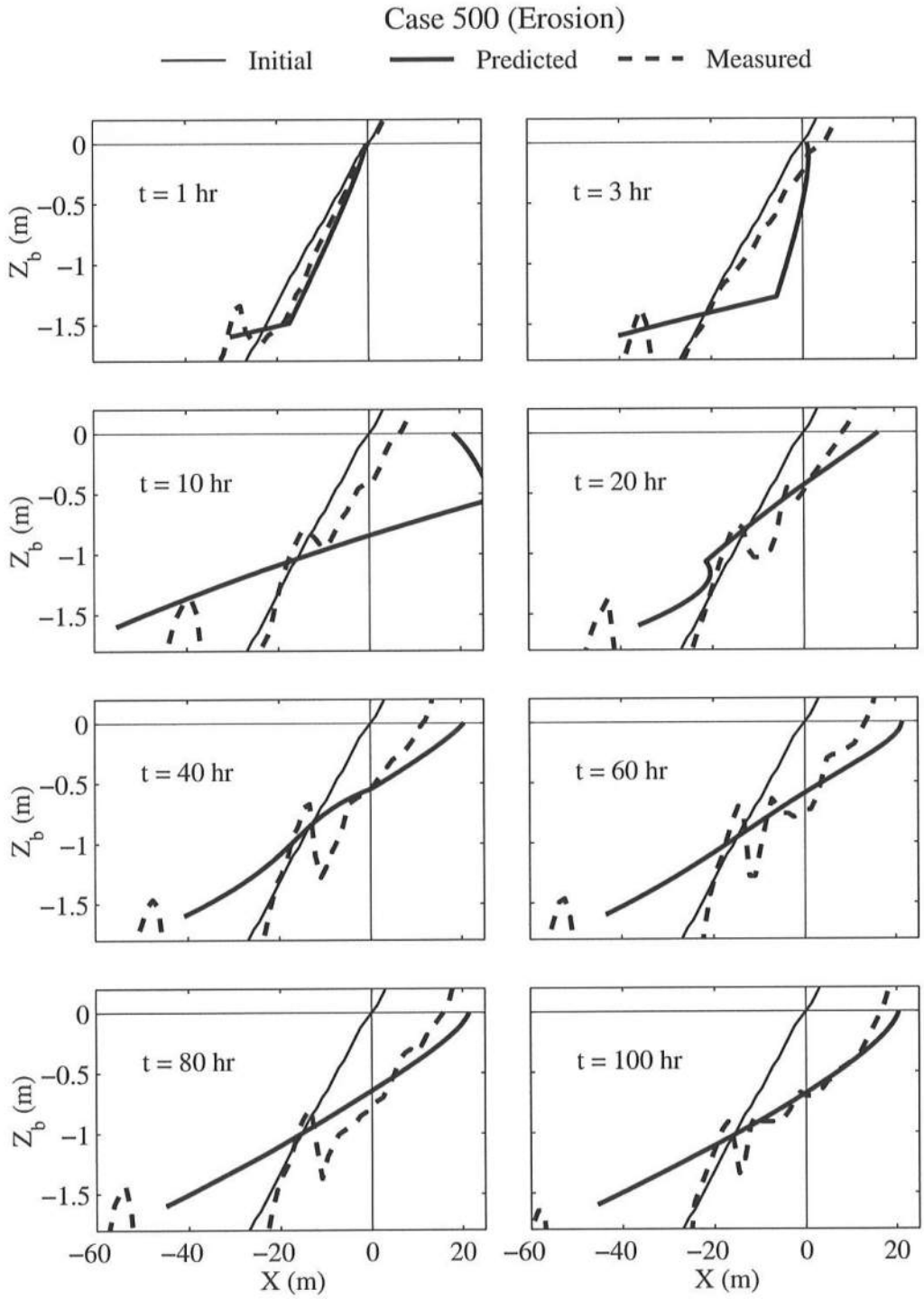

Figure 3.6: Measured and Predicted Beach Profiles for Case 500.

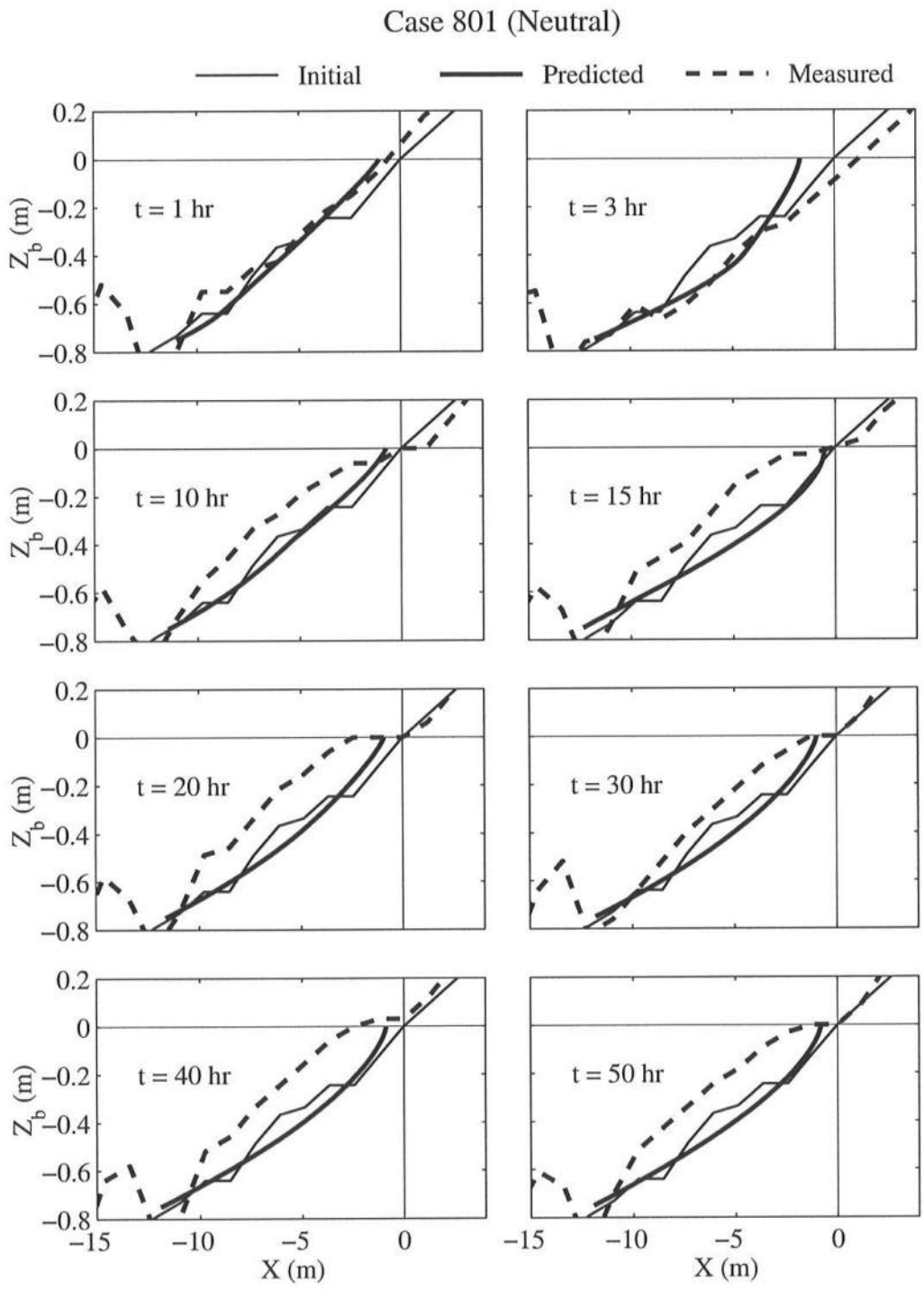

Figure 3.7: Measured and Predicted Beach Profiles for Case 801.

initial 1:15 slope at $t = 0$ and the bottom elevation z_b equals $-h$ with h = still water depth. The measured and predicted profiles are practically equilibrium at the last time level for each case. The semi-analytical solution based on the standard equilibrium profile is limited to the depth range $0 \leq h \leq h_b$ and can not predict bar formation. Both the seaward (accretion) and landward (erosion) displacements of the shoreline at $z_b = 0$ relative to the initial location $x = 0$ are predicted fairly well. The analytical solution based on x as a function of h and t occasionally produces two values of h at given x. This is not possible physically and may have been caused by the assumption (3.18) which has resulted in the wave equation for h without any diffusion. In conclusion, the simple profile evolution model proposed here may predict both the shoreline accretion and erosion but may be no better than existing models [e.g. Kriebel and Dean (1985); Kriebel *et al.* (1991)] based on the standard equilibrium profile which does not always represent the measured profiles well.

3.5 Comparison with Equilibrium Beach Data

To develop a time-averaged sediment transport model based on (3.14)–(3.16), it is necessary to overcome the closure problem created by time averaging. It might be possible to assume on the basis of (3.17) without the overbar for time averaging that the suspension rate S_e, the sediment concentration C_e and the energy dissipation rate per unit volume, D_B/h, are constant in the surf zone on an equilibrium beach. This assumption is examined using the irregular wave data that corresponds to test 4 and test 5 for equilibrium beach profiles that are outlined in Chapter 2. In review, the measured sand characteristics were $d_{50} = 0.18\ mm$, $w_f = 1.9\ cm/s$, $s = 2.66$ and $n_p = 0.4$ with the empirical $A = 0.067\ w_f^{0.44} = 0.09\ m^{1/3}$. Two tests were conducted for two different irregular waves. The incident waves were measured in 0.6 m water depth as shown in Table 2.1. The spectral significant wave height H_{mo} was 18.2 and 20.3 cm for tests 4 and 5, respectively. The spectral peak period T_p was 1.6 and 2.8 s for tests 4 and 5, respectively. A comparison of the the nonlinear

time-averaged model CSHORE with the measured wave statistics for these tests was presented in Section 2.5.

The equilibrium profile model of Dean (1977) makes the assumption of a constant energy dissipation rate per unit volume D_B/h along with a wave height of γh in (3.21) to obtain the monotonic equilibrium beach profile given by (3.25). This model, therefore, can not predict the barred and terraced profiles seen in Figures 3.8 and 3.9 which show the cross-shore variations of the measured and predicted root-mean-square wave height $H_{rms} = \sqrt{8}\,\sigma$ with σ = standard deviation of the free surface oscillation for tests 4 and 5. Creed *et al.* (1992) demonstrated that a more accurate energy dissipation model including a distribution of irregular wave heights such as that of Thornton and Guza (1983) could predict an equilibrium profile that differs from the (3.25) under the assumption of constant D_B/h. The energy dissipation rate per unit volume, D_B/h, in the model CSHORE is based on the formula proposed by Battjes and Janssen (1978) for the outer zone where the fraction of breaking waves is less than 1 as explained in Section 2.2. The energy dissipation within the inner zone is estimated empirically in CSHORE because the formula of Battjes and Janssen (1978) yields values of H_{rms} that exceed the maximum height H_m as explained in relation to (2.22). The energy dissipation rate D_B is predicted fairly well by CSHORE as the cross-shore variations of H_{rms} compare well with the data as seen in Figures 3.8 and 3.9. In spite of the very simple model for breaking waves adopted by Dean (1977), the measured equilibrium beach profile is represented fairly well by the standard equilibrium profile with $A = 0.09\ m^{1/3}$ inside the surf zone where the incident waves broke intensively at the bar crest(test 4) and the terrace edge (test 5). The energy dissipation rate D_B and the mean water depth h predicted by CSHORE are used in (3.17) to estimate the value of $C_e/e_B = [\rho g(s-1)w_f]^{-1}(D_B/h)_e$ where the suspension efficiency e_B is uncertain but may be on the order of 0.01. The estimated cross-shore variations of C_e/e_B for

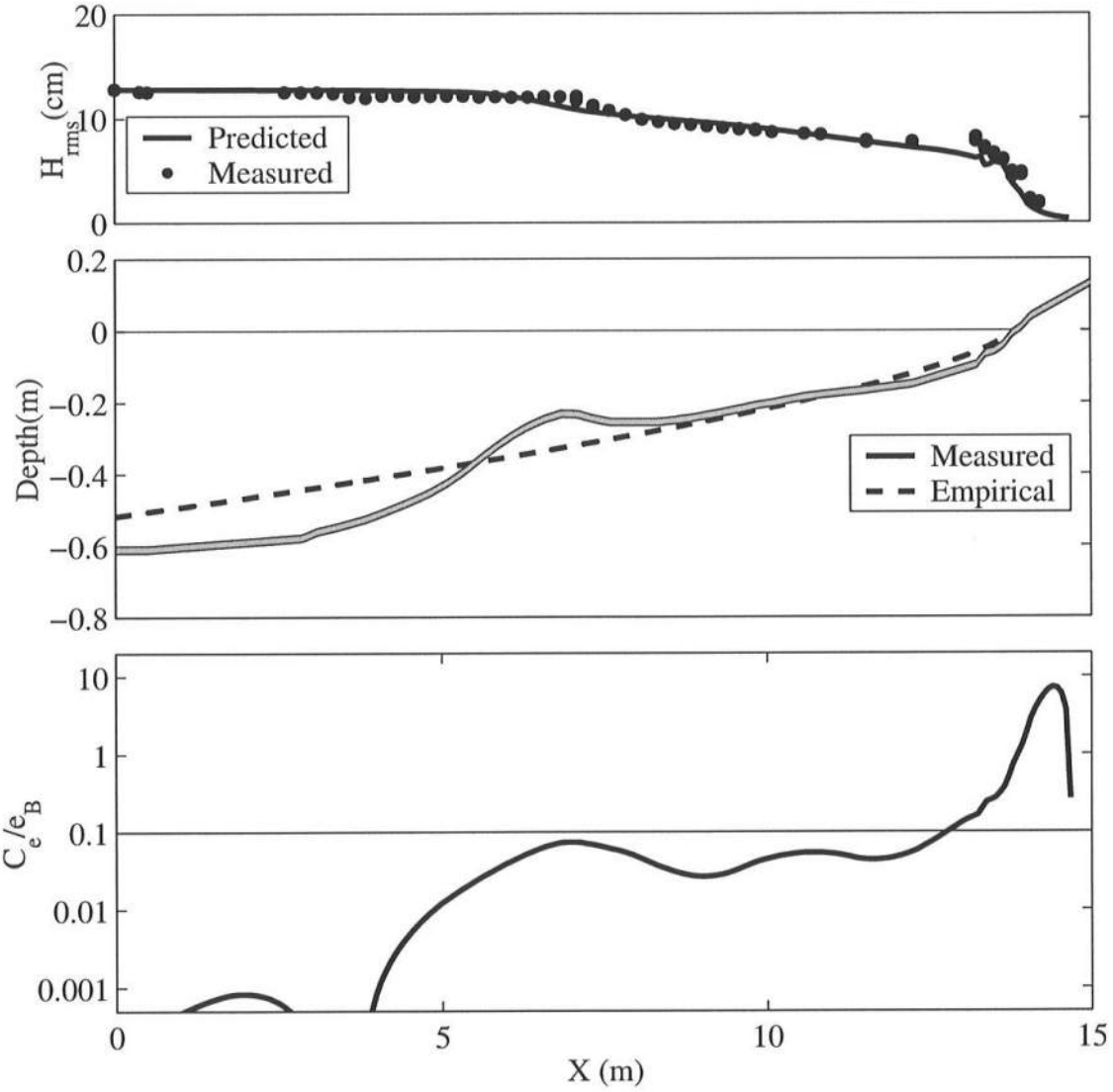

Figure 3.8: Cross-Shore Variations of Wave Height H_{rms}, Equilibrium Bottom Elevation and Time-Averaged Sediment Concentration for Test 4.

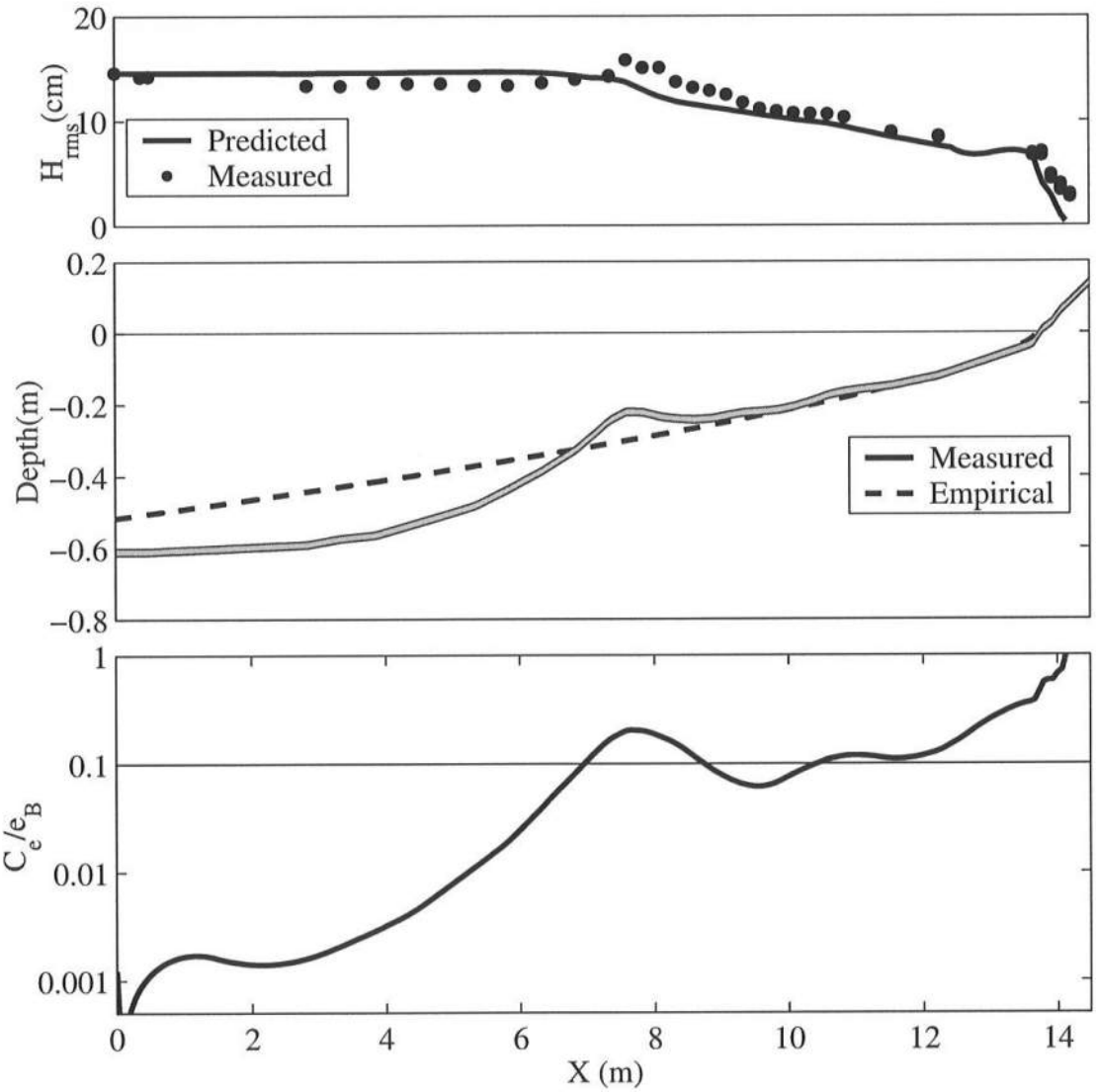

Figure 3.9: Cross-Shore Variations of Wave Height H_{rms}, Equilibrium Bottom Elevation and Time-Averaged Sediment Concentration for Test 5.

tests 4 and 5 indicate that the values of C_e/e_B and D_B/h are very small seaward of the breaker zone as expected and roughly constant in the surf zone but that these values are significantly larger in the swash zone. As a result, the assumption of constant energy dissipation rate per unit volume is less accurate than the standard equilibrium profile for these two tests, and a new assumption will be required to predict various equilibrium profiles. This problem is related to closure problem for the time-averaged sediment transport model based on (3.15)–(3.17). Future studies will be required to solve these problems and extend the time-averaged irregular wave model CSHORE to predict beach profile evolution more accurately.

Chapter 4

TIME-DEPENDENT SEDIMENT TRANSPORT MODEL

4.1 Introduction

A time-dependent, cross-shore sediment transport model in the surf and swash zones on beaches is developed to predict both beach accretion and erosion under the assumptions of alongshore uniformity and normally incident waves. The model is based on the time-dependent equations derived in Chapter 3. Because Chapter 3 discussed existing beach profile evolution models only, a more extensive review on nearshore sediment transport is given in the following.

Considering the complexity of the three-dimensional nearshore processes including the spatial and temporal variability of sand bar morphology (Lippmann and Holman 1990) and shoreline position (Plant and Holman 1996), this study has been limited to the cross-shore processes of well-sorted sand in surf and swash zones under the assumptions of alongshore uniformity and normally incident waves. These assumptions may be too restrictive but beach recovery even under these conditions can not be explained quantitatively at present. The bottom boundary layer and sediment transport outside surf zones are better understood [e.g., Grant and Madsen, (1986); Madsen *et al.* (1993)]. Longshore currents and sediment transport inside surf zones are also better understood apart from the uncertainties of the cross-shore and vertical distributions of longshore currents [e.g., Gallagher *et al.* (1998); Garcez Faria *et al.* (1998)] and longshore sediment fluxes [e.g., Wang (1998)].

Empirical one-dimensional models are widely used in the U.S. to predict beach and dune erosion [e.g., Kriebel *et al.* (1991)]. These models are based on the

concept of equilibrium beach profiles without any bar (Dean 1991), an empirical closure depth of the profile change, and empirical criteria for beach erosion and accretion (Kraus *et al.* 1991; Dalrymple 1992). The empirical models based on the adjustment of a beach profile toward an equilibrium profile in the presence of large storm surge can predict dune erosion reasonably well if empirical parameters are calibrated (Kobayashi 1987; Zheng and Dean 1996). As for nearshore bars, Trowbridge and Young (1989) used a sheet flow model based on the time-averaged onshore bottom shear stress to explain the onshore movement of a bar on a natural beach observed during low-energy wave conditions. Thornton *et al.* (1996) and Gallagher *et al.* (1998) used the energetics-based total load model of Bailard (1981) to explain the offshore movement of a bar on the same beach observed during storms. The energetics model could not predict the slow onshore migration observed during low-energy wave conditions. The sheet flow and energetics models could not explain equilibrium terraced and barred beaches created by irregular waves in a wave flume (Orzech and Kobayashi 1998).

Cross-shore beach profile models based on physical processes were developed mostly in Europe and Japan. For example, Hedegaard et al. (1992) presented the intercomparison of five European and one Japanese model. The hydrodynamic modules of these six models are mostly based on the horizontally one-dimensional, time-averaged equations for energy and momentum for predicting the wave height and setup as well as the vertically one-dimensional, time-averaged momentum equation for predicting the undertow current [e.g., Svendsen (1984a)]. For the sediment transport modulus, use was made of a vertical diffusion equation of suspended sediment combined with a bed load formula (Deigaard *et al.* 1986) or the energetics model of Bailard (1981) which was modified to include the effect of wave breaking explicitly (Roelvink and Stive 1989). These sediment transport models assume that the local sediment transport rate is determined solely by the local hydrodynamic

forcing and sediment characteristics without regard to cross-shore sediment advection. The comparisons of these six models with the measured eroded profiles in a large wave flume indicated the deficiencies of the models in terms of swash dynamics and low-frequency waves. No comparison was made with accreted beach profiles.

The instantaneous concentration of suspended sediment measured by various researchers [e.g., Hanes (1991); Beach and Sternberg (1991), (1992); Conley and Inman (1992); Hay and Bowen (1994); Jaffe and Rubin (1996); Foster *et al.* (1996); Puleo *et al.* (2000)] outside and inside surf zones on natural beaches indicated intermittent temporal variations in which the instantaneous concentration was intermittently much larger than the mean concentration. Possible mechanisms suggested for the intermittent variations include bed forms (ripples and megaripples), large waves in a wave group, vortices and turbulence generated by breaking waves and bores, wave-induced boundary ventilation, and coherent motions including shear instability in the turbulent boundary layer. Numerical time-dependent models developed to predict sediment suspension include vertical diffusion models for spilling waves (Deigaard *et al.* 1986) and for nonbreaking waves (Li and Davies 1996), a discrete vortex model for plunging waves (Pedersen *et al.* 1995), and a convection-diffusion model (Duy and Shibayama 1997). The comparisons of these models for breaking waves were limited to the mean concentration under monochromatic waves probably because of the large uncertainty of the time-dependent bottom boundary condition for the concentration and because of extensive computation time to simulate irregular waves. On the other hand, Lin and Liu (1998) solved the Reynolds equations with an algebraic nonlinear Reynolds stress model and computed the solute mixing under plunging waves which was impulsive and almost immediate. None of these time-dependent models were applied to predict cross-shore beach profile changes.

The above concise review suggests that the sediment transport models adopted in the existing cross-shore beach profile models may be too simplistic to predict

both beach erosion and accretion. On the other hand, the two-dimensional, time-dependent models for suspended sediment may be too demanding computationally for the simulation of beach profile evolution. Furthermore, the accuracy of these time-dependent models may be limited by the very limited knowledge of sediment dynamics in the bottom boundary layer in surf zones. As a result, a one-dimensional, time-dependent model is developed here to predict the depth-integrated sediment dynamics and resulting beach profile change in surf and swash zones.

4.2 Formulation

The time-dependent sediment continuity equation derived in Section 3.2.1 is modified slightly in the following. The vertical distributions of bed load and suspended sediment are not analyzed in the following one-dimensional model which assumes that suspended load is dominant in surf and swash zones. The depth-integrated continuity equation (3.6) for sediment per unit horizontal area is modified as

$$\underset{\text{storage}}{\frac{\partial}{\partial t}(hC)} + \underset{\text{advection}}{\frac{\partial}{\partial x}(hCU_s)} = \underset{\text{suspension}}{S} - \underset{\text{settling}}{w_f C} \tag{4.1}$$

where t is time, x is the cross-shore coordinate defined positive onshore, h is the instantaneous water depth, C is the depth-averaged sediment concentration including both bed load and suspended load, U_s is the horizontal sediment velocity, S is the upward sediment suspension rate from the bottom, and w_f is the sediment fall velocity. The concentration C is defined such that hC is the sediment volume in the water column per unit horizontal area. The sediment velocity U_s is defined such that hCU_s is the volumetric sediment transport rate per unit width which is positive onshore. The sediment settling rate $w_f C$ in (4.1) is assumed to be represented by the depth-averaged concentration C.

The horizontal fluid and sediment velocities are generally assumed to be the same. As a result, the sediment velocity U_s in the advection term in the one-dimensional equation (4.1) was approximated by the depth-averaged horizontal fluid velocity U in (3.6). This approximation may introduce a dispersion term due to the vertical variations of the horizontal fluid velocity and the sediment concentration [e.g., Kobayashi *et al.* (1997a)] but this dispersion term is neglected for lack of knowledge of the vertical distribution of the instantaneous sediment concentration. For steady uniform flow, Kobayashi and Seo (1985) solved the conservation equations of mass and momentum for both the fluid and sediment and showed the difference between the horizontal fluid and sediment velocities on the order of the sediment fall velocity w_f. The discriminator laser-Doppler velocimeter measurement by Muste and Patel (1997) indicated that the streamwise velocity of suspended fine sand was less than that of water by as much as 4%. The sediment velocity U_s in (4.1) is assumed to be given by

$$U_s = U - w_f \tag{4.2}$$

Admittedly, (4.2) results in $(-U_s) > (-U)$ when $U < 0$ but the small correction $w_f > 0$ increases the mean offshore sediment velocity $\overline{U}_s = (\overline{U} - w_f)$ where the overbar denotes time averaging and $\overline{U}$ is the return current flowing offshore which is smaller than the undertow flowing offshore below the wave trough (Kobayashi *et al.* 1989). In short, (4.2) should be regarded as an empirical adjustment for the shortcoming of the one-dimensional equation (4.1).

As demonstrated in Section 3.2.1, the sediment suspension rate S has been estimated using the transport equation for the turbulent kinetic energy k as

$$S = \frac{P - \epsilon}{(s-1)g} \tag{4.3}$$

where $(P - \epsilon)$ is the net production rate of k used for the sediment suspension from the bottom. Expressing $(P - \epsilon)$ in terms of the local wave energy dissipation rates

D_B and D_f per unit horizontal area due to wave breaking and bottom friction, respectively, (4.3) has been rewritten as

$$S = \frac{e_B\, D_B + e_f\, D_f}{\rho g(s-1)h} \tag{4.4}$$

The suspension rate S is thus expressed in terms of the energy dissipation rates D_B and D_f which can be predicted using a one-dimensional, time-dependent wave model. The suspension efficiencies e_B and e_f in (4.4) are assumed constant, although e_B may depend on breaker types such as spilling and plunging breakers. It is expected that $e_B < e_f$ because bottom friction acting on the bottom may be more efficient than wave breaking occurring at the water surface. The instantaneous response between D_f and S in (4.4) may be realistic but the lag between D_B and S neglected in (4.4) may cause some shift in the predicted erosion and accretion pattern.

The sediment continuity equation (4.1) along with (4.2) and (4.4) may be solved numerically to obtain $C(t,x)$ for the computed $h(t,x)$, $U(t,x)$, $D_f(t,x)$ and $D_B(t,x)$ using a one-dimensional wave model. The temporal change of the bottom elevation z_b defined positive upward with $z_b = 0$ at the still water level (SWL) can be computed using the volume conservation of bottom sediment

$$\frac{\partial z_b}{\partial t} = \frac{w_f C - S}{(1-n_p)} \tag{4.5}$$

where n_p is the bottom sediment porosity. Substitution of (4.1) into (4.5) yields the sediment continuity equation in terms of the cross-shore gradient of the sediment transport rate where the storage term is normally neglected in comparison to the volume change of the bottom sediment during a sufficient duration. The suspension rate S in (4.5) is determined by the local hydrodynamic forcing of D_B and D_f in (4.4) but the concentration C in the settling rate $w_f C$ in (4.5) is influenced by the sediment advection from and to the surrounding areas.

4.3 Numerical Model

The numerical model called CBREAK is developed on the basis of (4.1), (4.2), (4.4) and (4.5) which are normalized using the following dimensionless variables denoted by the prime:

$$t' = \frac{t}{T} \ , \ x' = \frac{x}{\sigma H} \ , \ z_b' = \frac{z_b}{H} \ , \ h' = \frac{h}{H} \ , \ U' = \frac{U}{(gH)^{1/2}} \ , \ U_s' = \frac{U_s}{(gH)^{1/2}} \tag{4.6}$$

$$C' = \frac{C}{C_c} \quad , \quad S' = \frac{S}{C_c H/T} \quad , \quad D_B' = \frac{D_B}{\rho g H^2/T} \quad , \quad D_f' = \frac{D_f}{\rho g H^2/T} \tag{4.7}$$

$$\sigma = \frac{T(gH)^{1/2}}{H} \ , \ w_f' = \frac{w_f}{H/T} \ , \ C_c = \frac{e_f}{(s-1)} \ , \ C_m = \frac{(1-n_p)}{C_c} \ , \ e_r = \frac{e_B}{e_f} \tag{4.8}$$

where T and H are the characteristic wave period and height used for the normalization, respectively. The normalized variables in (4.6) and (4.7) are assumed to be on the order of unity. The important dimensionless parameters are defined in (4.8). The ratio σ between the horizontal and vertical length scales is assumed to be large for finite-amplitude, shallow-water waves in surf zones. The normalized sediment fall velocity w_f is the inverse of the Dean number which has been shown to be useful in separating bar and berm profiles [e.g., Kraus *et al.* (1991); Dalrymple (1992)]. The characteristic concentration C_c determines the order of magnitude of the concentration C. The normalized concentration C_m of the bottom sediment with the porosity n_p is the maximum value allowed for C'. The ratio e_r between the suspension efficiencies e_B and e_f is assumed to be in the range $0 < e_r \leq 1$. Substitution of (4.6)–(4.8) into (4.1), (4.2), (4.4) and (4.5) yields

$$\frac{\partial}{\partial t'}(h'C') + \frac{\partial}{\partial x'}(h'C'U_s') = S' - w_f'C' \tag{4.9}$$

$$U_s' = U' - \frac{w_f'}{\sigma} \quad , \quad S' = \frac{D_f' + e_r D_B'}{h'} \tag{4.10}$$

$$\frac{\partial z_b'}{\partial t'} = \frac{w_f'C' - S'}{C_m} \tag{4.11}$$

For sands under typical breaking waves in surf zones on natural beaches, the length ratio σ is on the order of 10. The normalized fall velocity w_f', which can also be regarded as the ratio between the sediment fall velocity w_f and the vertical velocity scale H/T, is generally on the order of unity or less. The difference $(U'-U_s')$ between the normalized fluid and sediment horizontal velocities is hence on the order of 0.1 or less. Assuming the suspension efficiency $e_f \simeq 0.01$ as suggested by Bagnold (1966), $C_c \simeq 0.006$ and $C_m \simeq 100$ for sands with $s \simeq 2.6$ and $n_p \simeq 0.4$. This estimated order of magnitude of C_c is consistent with available concentration data in surf and swash zones on natural and laboratory beaches (Beach and Sternberg 1991; Van Rijn and Kroon 1992; Kobayashi *et al.* 1996; Osborne and Rooker 1999; Puleo *et al.* 2000). Eq. (4.11) with $C_m \simeq 100$ indicates that the temporal change of the bottom elevation over one wave period is indeed very small and on the order of 0.01. The morphological time scale of the beach profile change is thus on the order of 100 T and much larger than the characteristic wave period T. In the following, th prime for the normalized variables is omitted for brevity.

The numerical model CBREAK is an extension of the numerical wave model RBREAK based on the finite-amplitude, shallow-water equations under the assumption of $\sigma^2 \gg 1$ (Kobayashi *et al.* 1989; Kobayashi and Wurjanto 1992). RBREAK has been verified extensively using inner surf and swash data on natural beaches by Raubenheimer *et al.* (1995, 1996) and Raubenheimer and Guza (1996). The hydrodynamic variables used in RBREAK are normalized in the same way as in (4.6)–(4.8). The normalized continuity, momentum and energy equations are given by

$$\frac{\partial h}{\partial t} + \frac{\partial}{\partial x}(hU) = 0 \tag{4.12}$$

$$\frac{\partial}{\partial t}(hU) + \frac{\partial}{\partial x}(hU^2 + \frac{1}{2}h^2) = -h\frac{\partial z_b}{\partial x} - \frac{1}{2}\sigma f_b|U|U \tag{4.13}$$

$$\frac{\partial E}{\partial t} + \frac{\partial F}{\partial x} = -D \quad , \quad D = D_B + D_f \quad , \quad D_f = \frac{1}{2}\sigma f_b|U|^3 \tag{4.14}$$

$$E = \frac{1}{2}(hU^2 + \eta^2) \quad \text{for} \quad z_b < 0 \quad , \quad E = \frac{1}{2}(hU^2 + \eta^2 - z_b^2) \quad \text{for} \quad z_b > 0 \tag{4.15}$$

$$F = hU(\eta + \frac{1}{2}U^2) \tag{4.16}$$

where f_b is the constant bottom friction factor, $\eta = (h + z_b)$ is the normalized free surface elevation above SWL, E is the specific energy normalized by $\rho g H^2$, and F is the energy flux per unit width normalized by $\rho g H^2 (gH)^{1/2}$. The normalized local bottom slope $(\partial z_b / \partial x)$ in (4.13) and the local surf similarity parameter ξ are related by $\xi = (\partial z_b / \partial x)/(2\pi)^{1/2}$ (Kobayashi *et al.* , 1989).

As a first attempt, CBREAK is limited to the computation of h, U, D_f, D_B and C using (4.9), (4.10) and (4.12)–(4.16) for the fixed bottom and for the duration of 100 T and the prediction of the rate of the bottom elevation change using (4.11). In other words, only the initial profile change is predicted in the following because the computation for a very long duration is time-consuming and may not be warranted if the initial profile change can not be predicted accurately.

The finite difference grid of grid sizes Δt and Δx is used to solve (4.9) and (4.12)–(4.14) numerically. The cross-shore grid size Δx is chosen to be constant and small enough to resolve the steep front of breaking waves where $\Delta x \simeq 0.005$ for the computed results presented in the following. The time step size Δt on the order of 0.001 is allowed to vary such that Δt is reduced in a semi-automated way whenever numerical difficulties occur at the moving shoreline defined as $h = \delta$ where $\delta = 0.001$ is used in the following computation. The seaward and landward boundaries of the computation domain are located at $x = 0$ and well above the moving shoreline, respectively. The initial time $t = 0$ for the computation marching forward in time is taken to be the time when the specified incident wave train arrives at $x = 0$. The initial conditions are specified as $\eta = 0$, $U = 0$ and $C = 0$ at $t = 0$ for $x \geq 0$.

For the known values of h_j, U_j and C_j at the time level t and at the cross-shore node j indicated by the subscript j, the values of these variables at the next time level $t^* = (t + \Delta t)$, which are denoted by the asterisk, are computed in sequence.

First, the values of h_j^* and U_j^* with the nodal location $j = 1, 2, \cdots, s^*$ are computed from (4.12) and (4.13) using the dissipative Lax-Wendroff method in the same way as RBREAK (Kobayashi *et al.* 1987). The integer s^* indicates the wet node next to the moving shoreline at the next time level t^*, and $h_j^* = 0$ and $U_j^* = 0$ for $j \geq (s^* + 1)$. The reflected wave train at $x = 0$ is computed from the characteristic equations derived from (4.12) and (4.13) (Kobayashi *et al.* 1989).

Second, the values of $(D_f)_j^*$, E_j^* and F_j^* are calculated using (4.14)–(4.16). The value of D_j^* is computed using the first equation in (4.14) which is approximated by the implicit first-order difference in t and the central difference in x. The computed D_j^* and $(D_f)_j^*$ are smoothed by averaging the computed values over the five nodes from $(j - 2)$ to $(j + 2)$ because numerical noises tend to occur near the steep wave front and the moving shoreline. Then, $0 \leq (D_f)_j^* \leq D_j^*$ is imposed so that $(D_B)_j^* = [D_j^* - (D_f)_j^*] \geq 0$. The values of $(U_s)_j^*$ and S_j^* are calculated using (4.10) before the computation of C_j^* using (4.9) where $C_j^* = 0$ for $j \geq (s^* + 1)$.

Third, the sediment continuity equation (4.9) is solved using the MacCormack method in the same way as Kobayashi and Karjadi (1996) who computed the alongshore fluid velocity V using the alongshore momentum equation for small incident wave angles. These two equations become the same if C and U_s in (4.9) are replaced by V and U, respectively, and S and w_f are regarded as the driving force and linearized friction factor for V, respectively. The value of C_1^* with $j = 1$ at $x = 0$ is computed separately using the following characteristic form of (4.9) derived using (4.10) and (4.12):

$$\frac{\partial C}{\partial t} + U_s \frac{\partial C}{\partial x} = \frac{S}{h} - \frac{w_f C}{h}\left(1 - \frac{1}{\sigma}\frac{\partial h}{\partial x}\right) \tag{4.17}$$

which is solved following the numerical procedure devised by Kobayashi and Karjadi (1996) to avoid the specification of C as input when $U_s > 0$ and the characteristic variable C propagates landward at $x = 0$. Use is made of the implicit first-order difference approximation of (4.17) along the straight characteristic path from the

unknown $\widehat{C}$ at the time level t to C_1^* at the next time level t^*. The value of $\widehat{C}$ is estimated from C_1 and C_2 by interpolation for $(U_s)_1^* < 0$ and by extrapolation for $(U_s)_1^* > 0$. This approximation of (4.17) yields

$$C_1^* = \left[1 + \frac{\Delta t w_f}{h_1^*}\left(1 - \frac{1}{\sigma}\,\frac{h_2^* - h_1^*}{\Delta x}\right)\right]^{-1}\left[C_1 - \frac{\Delta t}{\Delta x}\,(U_2)_1^*\,(C_2 - C_1) + \frac{\Delta t S_1^*}{h_1^*}\right] \tag{4.18}$$

Use of the Lax-Wendroff and MacCormack methods results in numerical high-frequency oscillations that tend to appear at the rear of a breaking wave, especially on a gentle slope. These numerical artifacts are apparent, for instance, in the computed free surface elevation η as shown in Figures 4.1–4.3. More advanced numerical solutions such as slope-limiting methods do not suffer these numerical oscillations [e.g. LeVeque (1990)]. The Lax-Wendroff and MacCormack methods are used, nevertheless, due to previous experience as explained above.

The time-marching computation is continued until the normalized time $t = 100$ where the following computation is limited to regular incident waves. The computed temporal variations of h, U and C become periodic sufficiently before $t = 100$ as shown in Section 4.4. After the establishment of the periodicity, computation is made of the time-averaged quantities denoted by the overbar which are involved in the time-averaged sediment continuity equation obtained from (4.9) along with (4.10)

$$\frac{\partial}{\partial x}\overline{(hCU_s)} = \overline{S} - w_f\overline{C} \tag{4.19}$$

$$\overline{hCU_s} = \overline{hC}\;\overline{U_s} + \overline{(hC - \overline{hC})(U_s - \overline{U_s})}\;,\quad \overline{U_s} = \overline{U} - \frac{w_f}{\sigma} \tag{4.20}$$

$$\overline{S} = \overline{S_f} + \overline{S_B}\;,\quad \overline{S_f} = \overline{\left(\frac{D_f}{h}\right)}\;,\quad \overline{S_B} = e_r\overline{\left(\frac{D_B}{h}\right)} \tag{4.21}$$

where $\overline{S_f}$ and $\overline{S_B}$ are the time-averaged suspension rates due to the turbulence generated by bottom friction and wave breaking, respectively. The net cross-shore sediment transport rate $\overline{hCU_s}$ in (4.19) is the sum of the offshore (negative) and onshore (positive) transport rates as shown in (4.20). The time-averaged sediment

volume $\overline{hC}$ per unit horizontal area is transported offshore by the mean sediment velocity $\overline{U_s}$ which is negative because the return current $\overline{U}$ flows offshore. The small correction w_f/σ increases this offshore sediment transport rate slightly. The oscillatory components $(hC - \overline{hC})$ and $(U_s - \overline{U_s}) = (U - \overline{U})$ are positively correlated and cause onshore sediment transport because sediment particles suspended under the steep front of breaking waves tend to transport onshore by the onshore wave velocity $(U - \overline{U})$. Finally, the normalized bottom elevation change Δz_b during one wave period is obtained by integrating (4.11) from $t = t_p$ to $t = (t_p + 1)$ with t_p being the time after the establishment of the periodicity

$$\Delta z_b = (w_f \overline{C} - \overline{S})/C_m \tag{4.22}$$

which is positive for accretion and negative for erosion.

4.4 Comparison with Initial Profile Change

Comparison is made with the regular wave data used in the comparison of the profile evolution model in Chapter 3 taken from large scale wave tank experiments conducted by Thorndike Saville and reported by Kraus and Larson (1988). The experiment was conducted in a wave tank that was 194 m long, 4.6 m wide, and 6.1 m deep. The initial beach slope was approximately 1/15. The measured initial profile is used in the following computation. The median sand diameter was 0.22 or 0.40 mm. The specific gravity of the sand was $s = 2.65$. The porosity of the sand bed differed slightly along the beach profile but $n_p = 0.4$ is assumed in the following comparison. Three representative cases are selected for the comparison with CBREAK. For case 201, a berm was formed above SWL and the still water shoreline was displaced seaward. For case 500, erosion occurred near the shoreline and a bar was formed near the break point. For case 801, the initial profile changed little. The sediment fall velocity was 5.9 cm/s for cases 201 and 801 and 3.1 cm/s for case 500. The wave period T was 11.33 s for case 201 and 3.75 s for cases 500

Table 4.1: Comparison of CBREAK with Three Cases

Case	Profile Change	T (s)	H (m)	d (m)	σ	ξ	w_f	R	r
201	accretion	11.33	1.52	1.56	28.8	0.77	0.44	0.69	0.08
500	erosion	3.75	1.83	2.20	8.7	0.23	0.064	0.39	0.03
801	neutral	3.75	0.91	0.95	12.3	0.33	0.24	0.34	0.03

and 801. The wave height H and the still water depth d listed in Table 4.1 are the measured breaker height and depth for each case. All the quantities presented hereafter are the normalized quantities defined in (4.6)–(4.8) where the prime has been omitted. The values of T and H for each case in Table 4.1 are used for the normalization.

The dimensionless parameters listed in Table 4.1 are explained along with the input parameters specified for the computation. The ratio σ between the horizontal and vertical length scales is in the range $\sigma = 8.7$–28.8. The shallow-water assumption of $\sigma^2 \gg 1$ is acceptable at the break point which is taken as the seaward boundary $x = 0$ for the computation. The normalized incident wave profile whose height and period are unity in the normalized depth d/H is specified for lack of the wave profile data using cnoidal wave theory [e.g., Kobayashi *et al.* 1987] where the Ursell parameter is larger than 55 for the three cases. The specified incident wave profile may not be very accurate but the finite-amplitude, shallow-water equations adopted in CBREAK are not expected to describe the detail of breaking waves in the outer surf zone. The surf similarity parameter ξ is proportional to the normalized bottom slope as explained in relation to (4.13). The value of ξ based on the uniform slope of 1/15 is 0.77, 0.23, and 0.33 for cases 201, 500, and 801, respectively. The breaking waves are likely to be plunging for case 201 and spilling for cases 500 and 801 on the basis of the empirical criteria by Battjes (1974). The normalized sediment fall velocity w_f is 0.44, 0.064, and 0.24 for cases 201, 500, and 801, respectively. The

computed wave transformation and sediment response in the surf and swash zones are explained in light of these different values of ξ and w_f where the computed results for case 801 fall between those for cases 201 and 500.

The bottom friction factor f_b in (4.13) and (4.14) is simply taken as $f_b = 0.015$ which was the value calibrated by Raubenheimer *et al.* (1995) using runup measurements on a natural beach. The value of R in Table 4.1 is the computed runup height on the initial beach which is the maximum shoreline elevation above SWL normalized by H. The swash zone is wider for plunging waves in case 201 with $R = 0.69$ than for spilling waves in cases 500 and 801 with $R = 0.34$–0.39. The computed wave reflection coefficient r at $x = 0$ is also listed in Table 4.1. Since $r = 0.03$–0.08, wave reflection is negligible at $x = 0$. On the other hand, the suspension efficiency e_f associated with bottom friction is simply taken as $e_f = 0.01$ as suggested by Bagnold (1966). For $e_f = 0.01$, $s = 2.65$ and $n_p = 0.4$, the characteristic concentration $C_c = 0.0061$ and the normalized bottom sediment concentration $C_m = 99$. These values seem to be reasonable as discussed in relation to (4.11). The suspension efficiency e_B associated with wave breaking is calibrated in the range $e_B = 0.002$–0.01 corresponding to the ratio $e_r = (e_B/e_f) = 0.2$–1. Only the ratio e_r appears in the normalized equations (4.9)–(4.11). The increase of e_r results in the increase of sediment suspension due to wave breaking. The computed results for $e_B = 0.005$ and $e_r = 0.5$ are shown in the following. The effects of e_B on the computed profile changes are discussed in relation to the comparison of the measured and predicted beach profile changes.

Computation is made for the duration $0 \leq t \leq 100$ for each case. Figures 4.1, 4.2, and 4.3 show the computed cross-shore variations of the free surface elevation η with the initial bottom elevation z_b, the horizontal fluid velocity U, the suspension rate S, and the sediment concentration C at $t = 99.25$ and 99.75 for cases 201, 500, and 801, respectively. For case 201 with $\xi = 0.77$, the steep front of a plunging wave

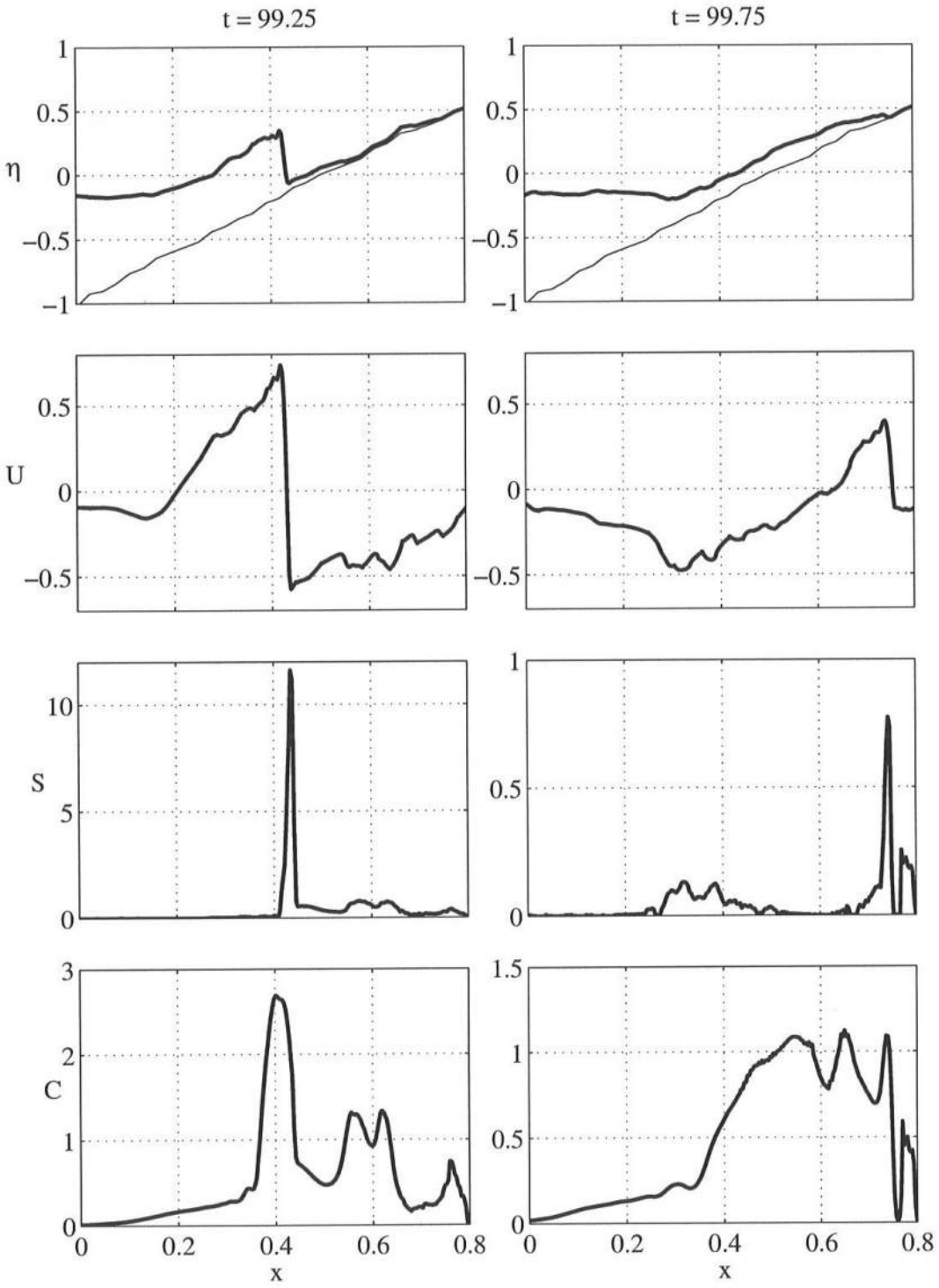

Figure 4.1: Computed Cross-shore Variations of η, U, S, and C at $t = 99.25$ and $t = 99.75$ for Case 201.

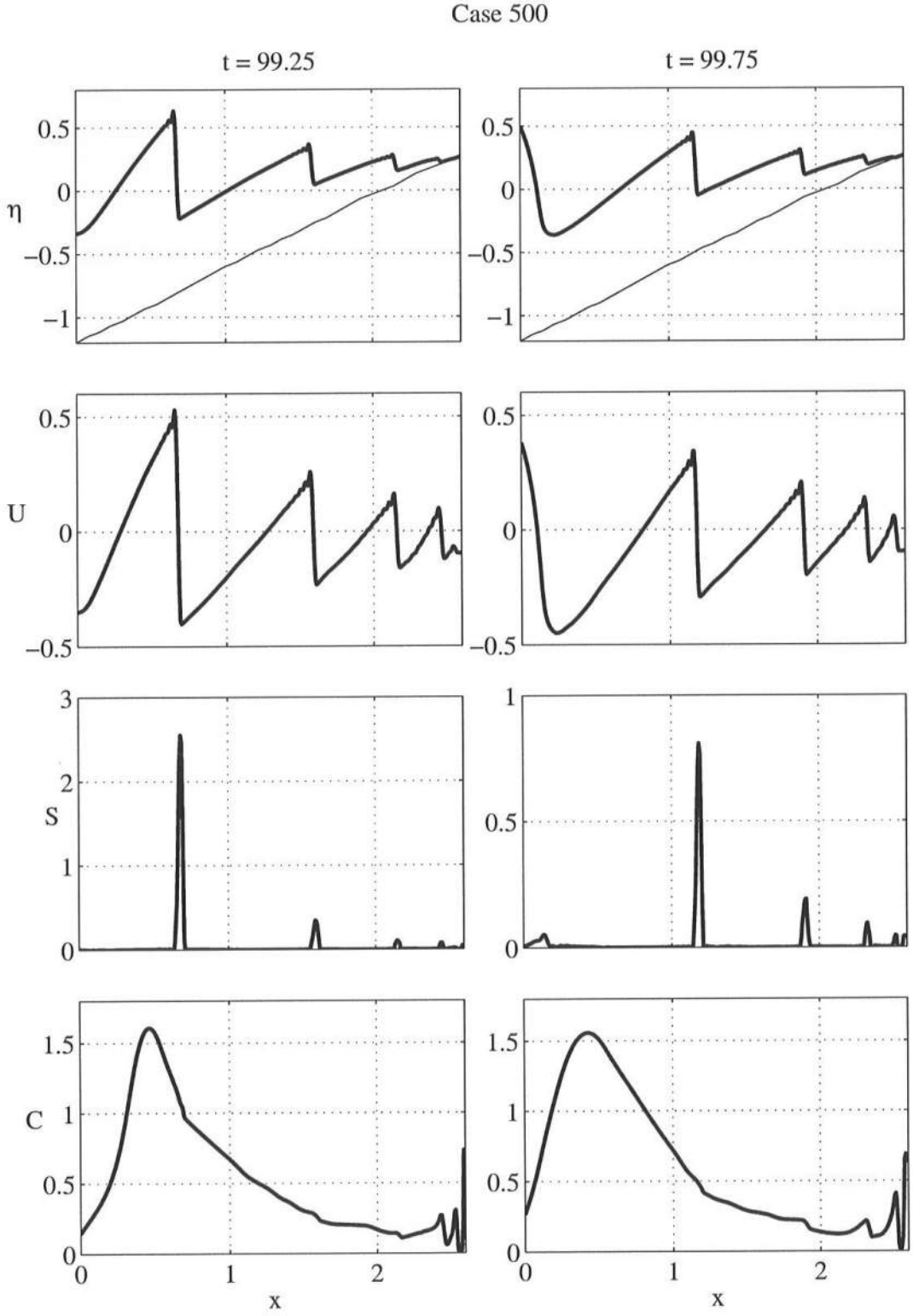

Figure 4.2: Computed Cross-shore Variations of η, U, S, and C at $t = 99.25$ and $t = 99.75$ for Case 500.

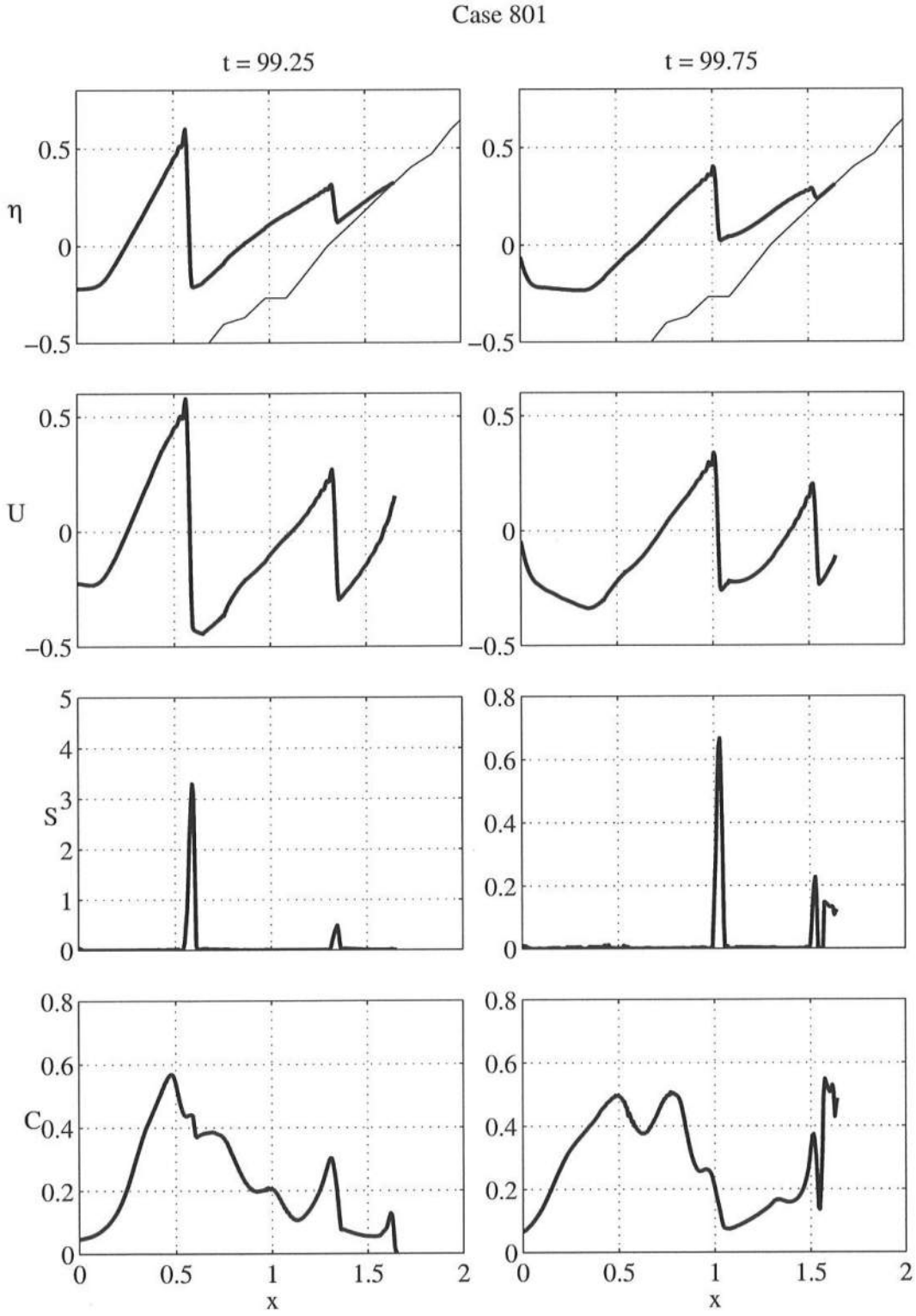

Figure 4.3: Computed Cross-shore Variations of η, U, S, and C at $t = 99.25$ and $t = 99.75$ for Case 801.

propagates upslope against a thin layer of water flowing downslope on the beach face at $t = 99.25$. The front propagating upslope is reduced and becomes gentler at $t = 99.75$ after a half of the wave period and water flows downslope in the rear of the front. Intense sediment suspension occurs in the narrow region of the steep front and milder sediment suspension occurs in the wider region of the water flowing downslope. The depth-averaged concentration C does not respond to the suspension rate S instantaneously even though $w_f = 0.44$ for case 201 is relatively large. The response is damped and shifted due to sediment storage and advection.

Figure 4.2 for case 500 with $\xi = 0.23$ shows four spilling waves with steep fronts in the surf zone. Each wave propagating upslope is dissipated almost completely before it reaches the shoreline which oscillates very little. Noticeable sediment suspension is confined near the steep wave fronts. The suspension intensity under the spilling wave is significantly less than that under the plunging wave shown in Figure 4.1. The depth-averaged concentration C for case 500 with $w_f = 0.064$ does not vary much with time because of the slow settling of the suspended sediment. It is noted that the values of S and C near the break point at $x = 0$ are fairly small in Figures 4.1 and 4.2. This is because the incident cnoidal wave specified at $x = 0$ needs to propagate onshore to develop a steep front in this one-dimensional computation. The lack of intense suspension at the break point may not be unrealistic in light of the turbulence data by Cox *et al.* (1994b) who found almost no turbulence in the interior below the break point defined as the start of aeration in the tip of the regular wave. Figure 4.3 for case 801 with $\xi = 0.33$ shows the case where the computed results lie between those for cases 201 and 500 shown in Figures 4.1 and 4.2.

Figures 4.4 and 4.5 show the temporal variations of the computed volume flux hU per unit width, the computed suspension rate S, and the computed concentration C at four cross-shore locations for case 201. Cases 500 and 801 are shown

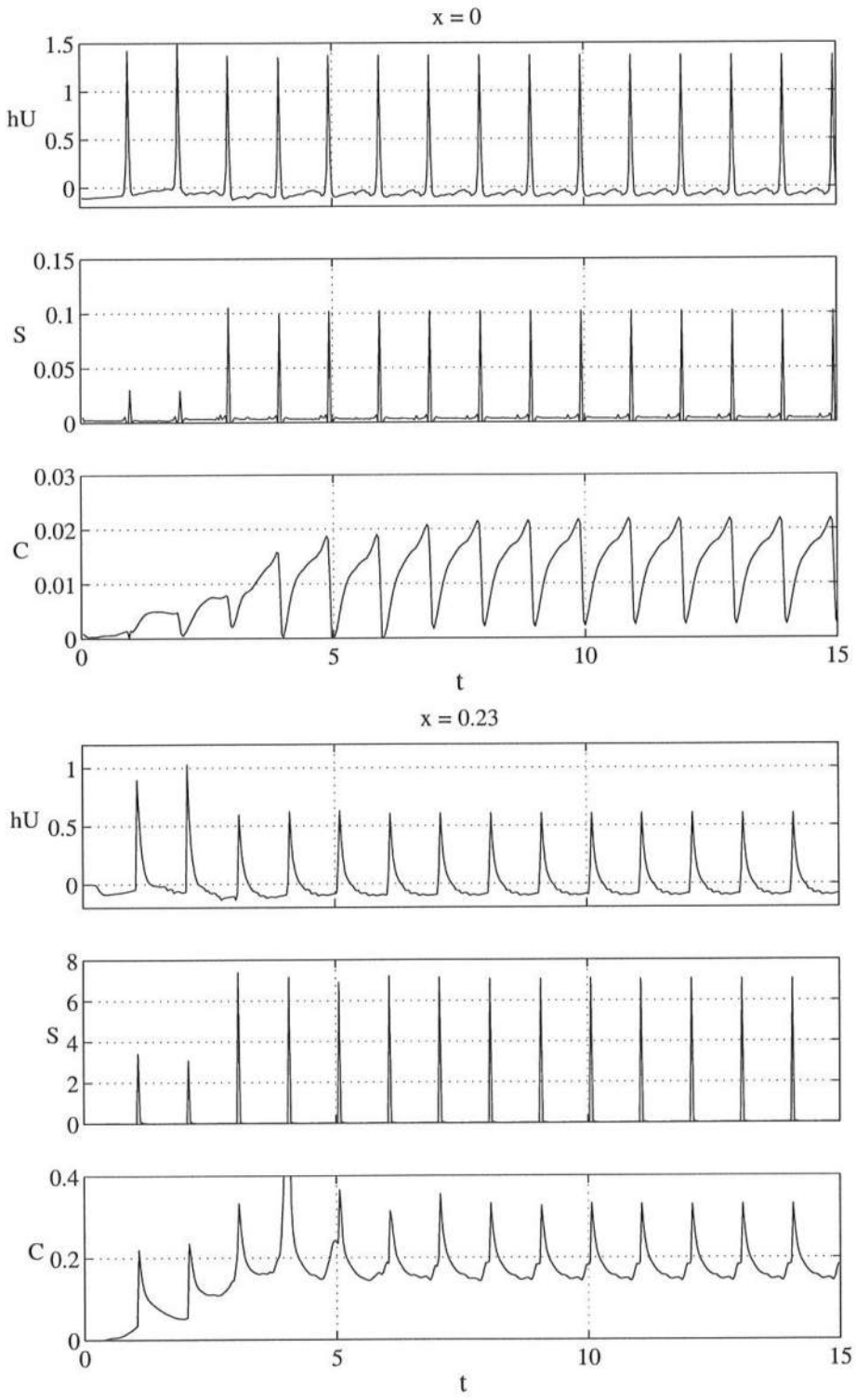

Figure 4.4: Temporal Variations of Computed hU, S, and C at $x = 0$ (top) and $x = 0.23$ (bottom) for Case 201.

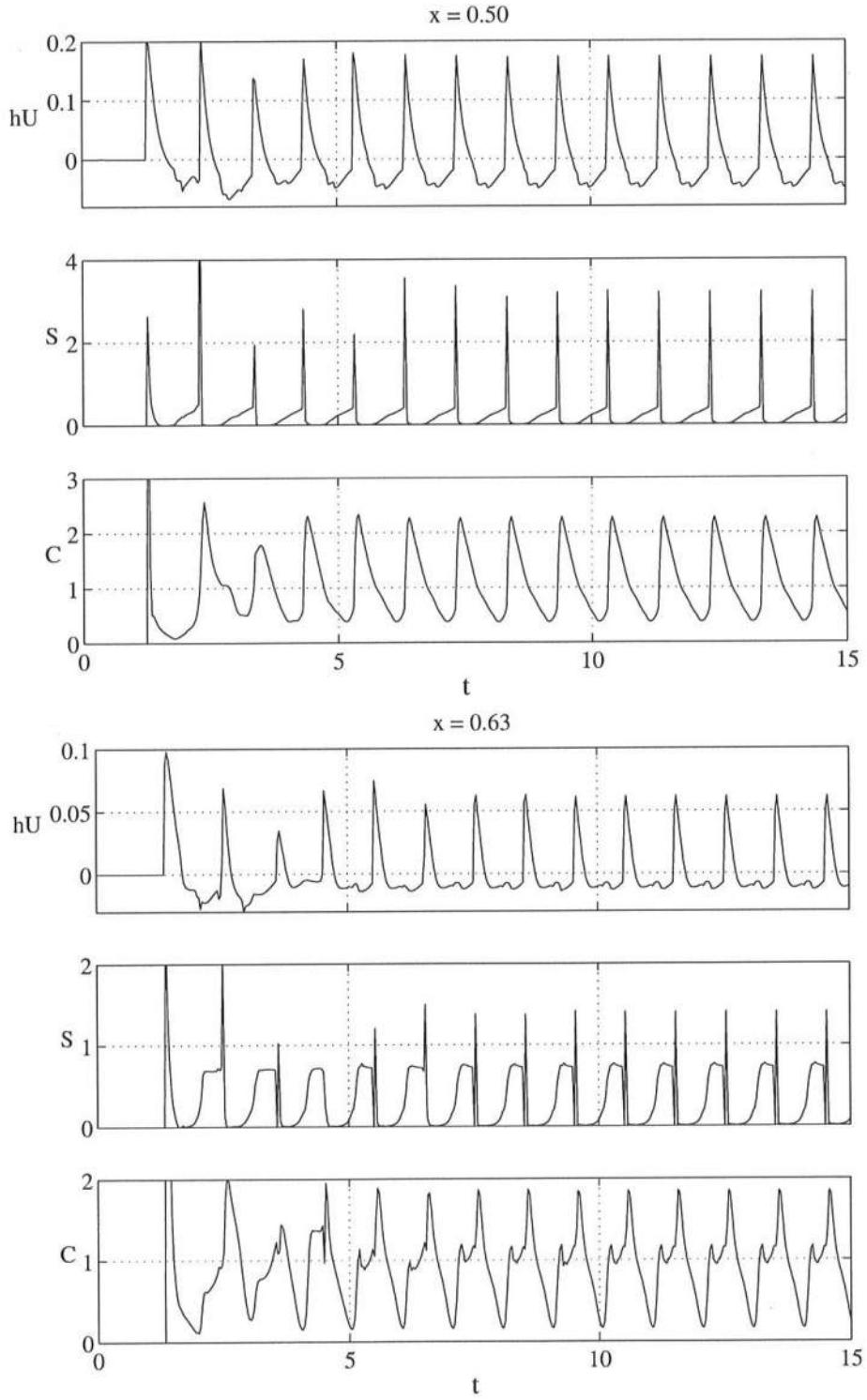

Figure 4.5: Temporal Variations of Computed hU, S, and C at $x = 0.5$ (top) and $x = 0.63$ (bottom) for Case 201.

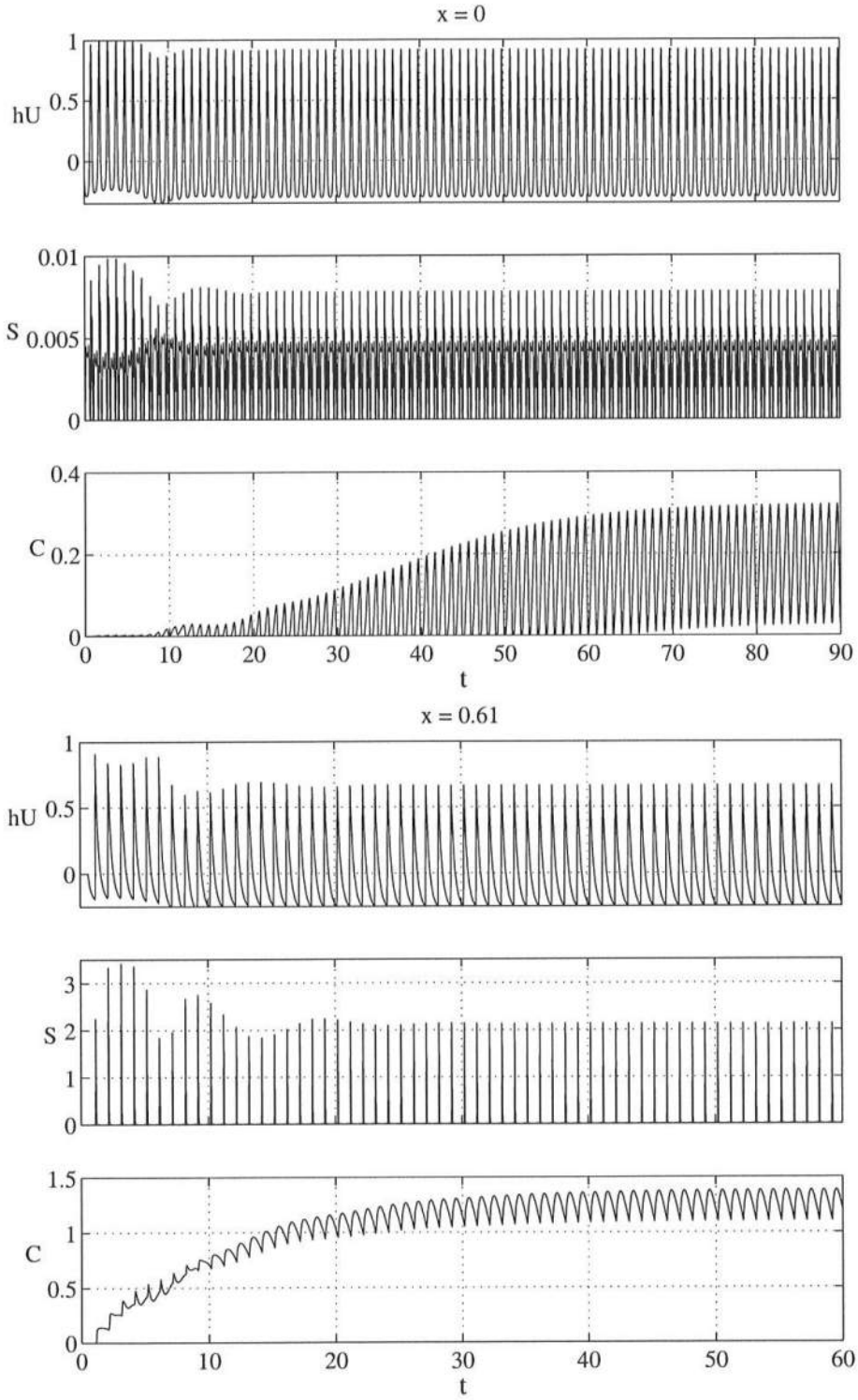

Figure 4.6: Temporal Variations of Computed hU, S, and C at $x = 0$ (top) and $x = 0.61$ (bottom) for Case 500.

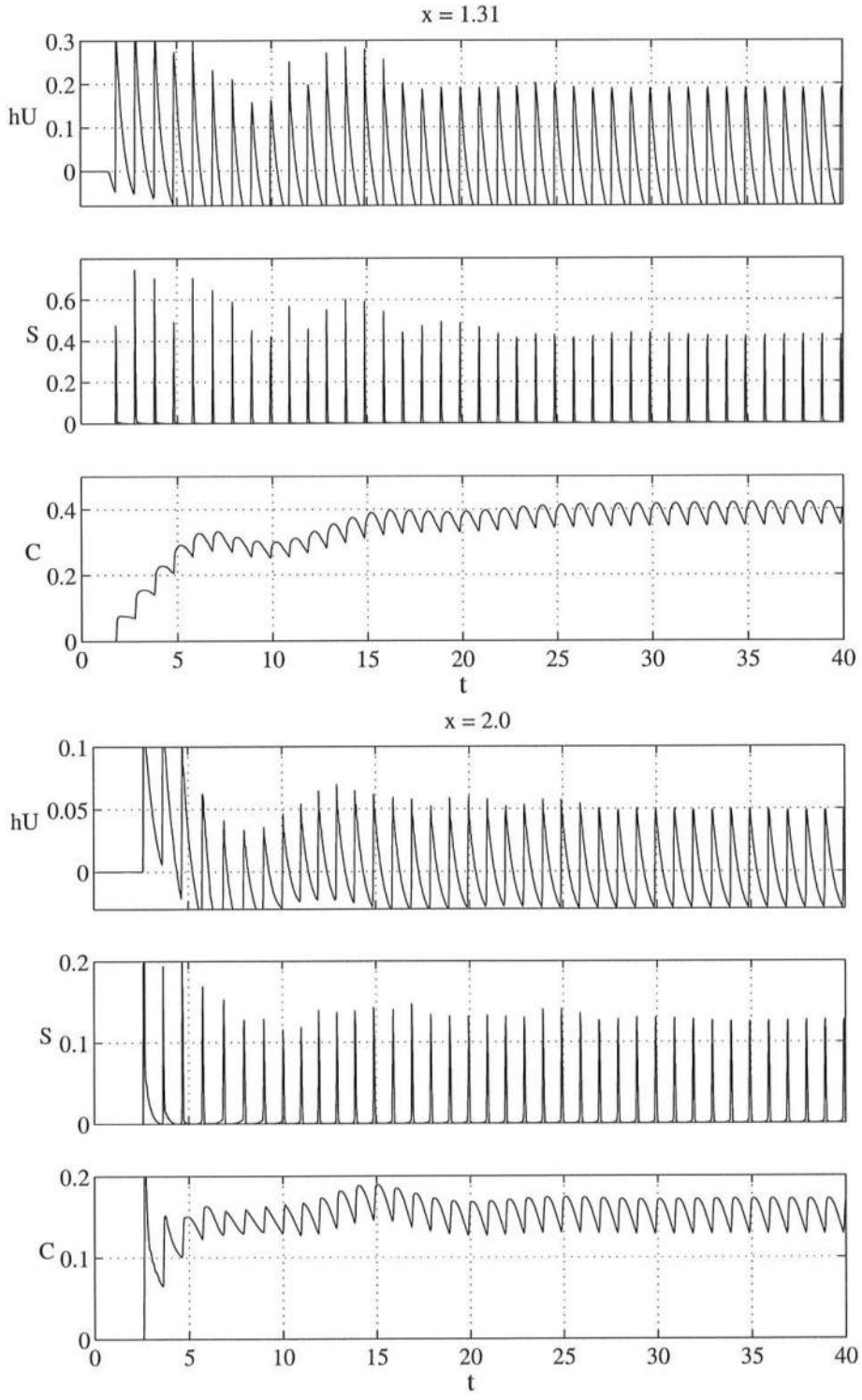

Figure 4.7: Temporal Variations of Computed hU, S, and C at $x = 1.31$ (top) and $x = 2.0$ (bottom) for Case 500.

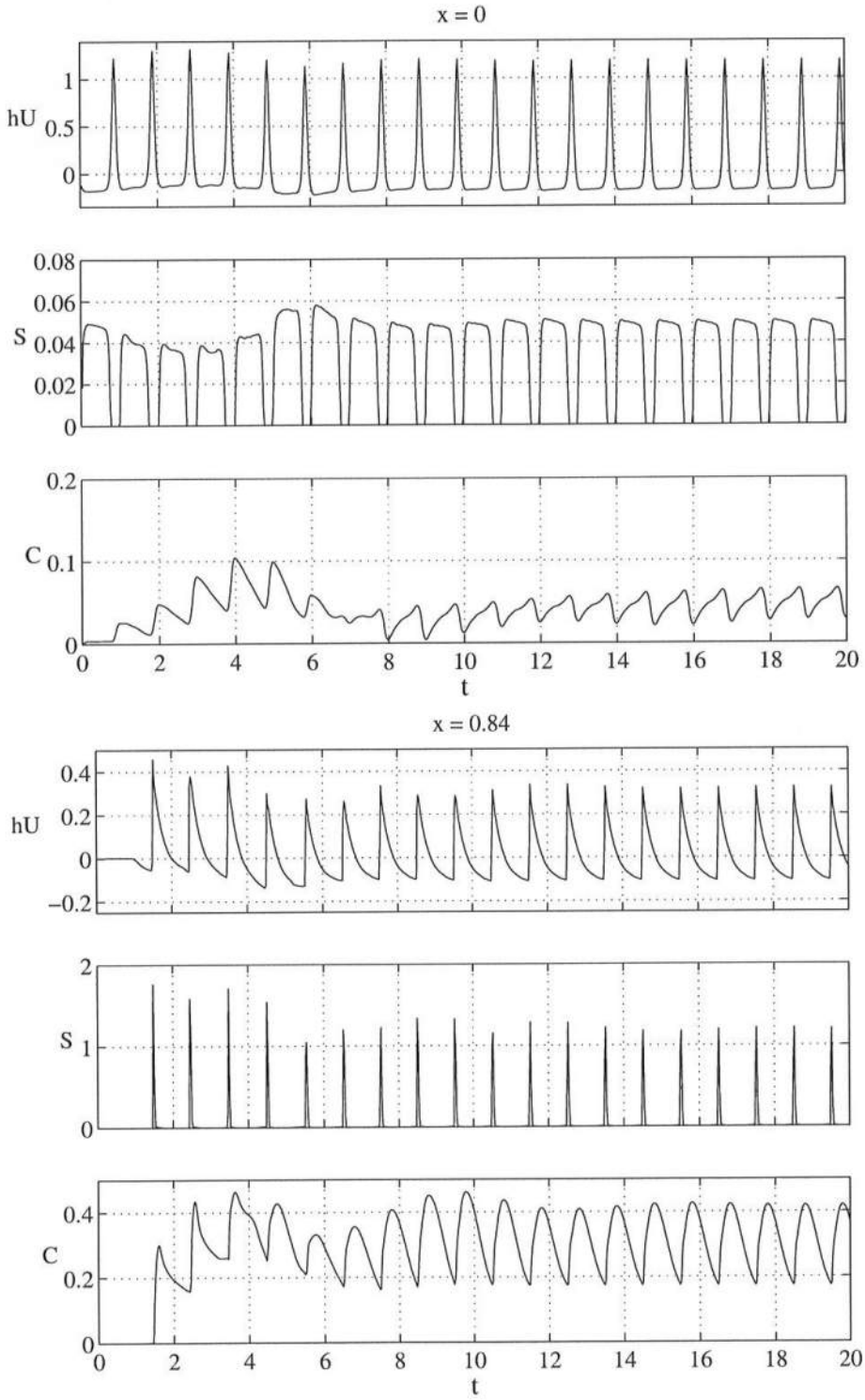

Figure 4.8: Temporal Variations of Computed hU, S, and C at $x = 0$ (top) and $x = 0.84$ (bottom) for Case 801.

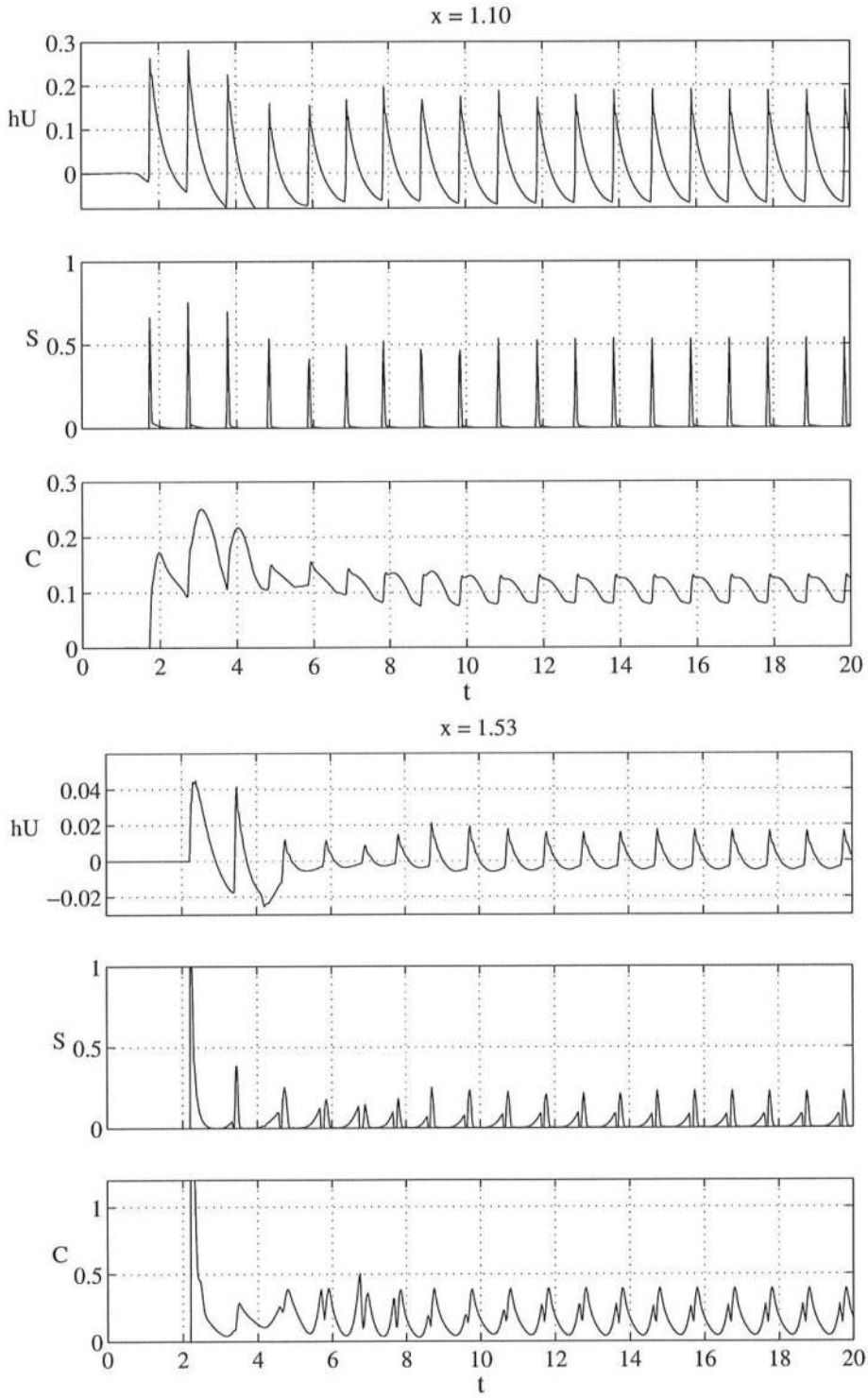

Figure 4.9: Temporal Variations of Computed hU, S, and C at $x = 1.10$ (top) and $x = 1.53$ (bottom) for Case 801.

in Figures 4.6–4.9. For case 201 with $\xi = 0.77$ and $w_f = 0.44$, the computed temporal variations become periodic after approximately ten waves. At the break point ($x = 0$), sediment suspension is caused by bottom friction associated with the large onshore velocity under the narrow wave crest and the small offshore velocity under the wide wave trough. In the middle of the surf zone ($x = 0.23$), intense suspension occurs under breaking waves but the mean concentration is as large as the oscillatory concentration. At the still water shoreline ($x = 0.50$), sediment suspension occurs intensely during short wave uprush ($hU > 0$) and mildly during long wave downrush ($hU < 0$). In the swash zone above SWL ($x = 0.63$), suspension during uprush is reduced and suspension during downrush is increased, while C appears to respond to S more instantaneously.

Figures 4.6–4.7 for case 500 with $\xi = 0.23$ and $w_f = 0.064$ show that the computed temporal variations do not become periodic until $t = 90$ at $x = 0$, $t = 60$ at $x = 0.61$, and $t = 40$ at $x = 1.31$ and 2.00 where the still water shoreline is at $x = 2.07$. At the break point ($x = 0$), sediment suspension is caused by bottom friction and the concentration averaged over several waves builds up very slowly. At the other locations $x = 0.61$, 1.31 and 2.00, wave breaking is well established and sediment suspension under breaking waves is dominant. However, the mean concentration exceeds the oscillatory concentration due to the large number of suspension events required to build up the mean concentration. Figures 4.8 and 4.9 show that the computed results for case 801 with $\xi = 0.33$ and $w_f = 0.24$ lie between those for cases 201 and 500. A periodic state is reached before approximately $t = 20$.

In the following, the time-averaged quantities during $99 < t \leq 100$ are used to examine the computed time-averaged sediment transport dynamics on the basis of (4.19)–(4.22). Figure 4.10 shows the cross-shore variations of $\overline{C}$, $\overline{S_B}$ and $\overline{S_f}$ for cases 201, 500, and 801. The time-averaged sediment concentration $\overline{C}$ is the maximum near the still water shoreline at $x = 0.50$ for plunging waves in case 201 and in the

outer surf zone for spilling waves in case 500. For case 801, the peaks of $\overline{C}$ occur in the middle of the surf zone and in the swash zone where the still water shoreline is located at $x = 1.31$. The time-averaged suspension rates $\overline{S_B}$ and $\overline{S_f}$ defined in (4.21) are caused by wave breaking and bottom friction, respectively. For the three cases, $\overline{S_B}$ is the maximum in the middle or outer surf zone but $\overline{S_B}$ is larger for case 201 because of wave breaking and dissipation in the narrow surf zone. For case 201, $\overline{S_f}$ is as large as $\overline{S_B}$ except that the suspension due to bottom friction is dominant in the swash zone. For cases 500 and 801, $\overline{S_f}$ is very small except in the narrow upper swash zone and numerical noises become apparent in the regions of very small $\overline{S_f}$. The cross-shore variations of $\overline{C}$ and $\overline{S} = (\overline{S_B} + \overline{S_f})$ are similar although S and C do not respond simultaneously as shown in Figures 4.1–4.9.

Figure 4.11 shows the cross-shore variations of the time-averaged sediment volume $\overline{hC}$ per unit area for the three cases where $\overline{hC} = [\overline{h}\ \overline{C} + \overline{(h-\overline{h})(C-\overline{C})}]$. The correlation between the oscillatory components $(h-\overline{h})$ and $(C-\overline{C})$ is generally positive and significant near the still water shoreline at $x = 0.50$ for plunging waves in case 201. The positive correlation implies that the sediment concentration tends to be larger under the wave crest and smaller under the wave trough where $(h-\overline{h}) = (\eta - \overline{\eta})$. The contribution of the correlated oscillatory components decreases with the decrease of w_f and ξ. For case 500, $\overline{hC} \simeq \overline{h}\ \overline{C}$ because the mean concentration $\overline{C}$ is larger than the oscillatory concentration $(C - \overline{C})$ as shown in Figures 4.6 and 4.7 and the slow sediment settling due to $w_f = 0.064$ reduces the correlation between the oscillatory concentration and the wave profile.

Figure 4.12 shows the cross-shore variations of the time-averaged sediment transport rate $\overline{hCU_s}$ per unit width for the three cases where $\overline{hCU_s}$ is the sum of the offshore transport rate $\overline{hC}\ \overline{U_s}$ and the onshore transport rate $\overline{(hC - \overline{hC})(U_s - \overline{U_s})}$ as shown in (4.20). These onshore and offshore transport rates are on the order of 0.1 and relatively small. Consequently, it is difficult to predict the small difference

on the order of 0.01 between the relatively small two quantities. The net rate $\overline{hCU_s}$ for the accretional case 201 is positive (onshore) and becomes the maximum (0.04) slightly seaward of the still water shoreline at $x = 0.50$. The net rate for the erosional case 500 is negative (offshore) and becomes the minimum (-0.008) in the outer surf zone. It should be noted that the net rate for case 500 would become slightly positive without the correction term w_f/σ added to $\overline{U_s} = (\overline{U} - w_f/\sigma)$ in (4.20) where $w_f/\sigma = 0.007$ for case 500. The net rate $\overline{hCU_s}$ for the neutral case 801 is slightly negative (more than -0.002) in the outer surf zone and slightly positive (less than 0.003) in the inner surf and swash zones. The net rate is hence practically zero.

Figure 4.13 shows the cross-shore variations of the net suspension rate ($\overline{S} - w_f\overline{C}$) per unit area for the three cases where the net rate is the relatively small difference between the suspension rate $\overline{S}$ and the settling rate $w_f\overline{C}$. The net suspension rate for the accretional case 201 is positive (erosion) in the surf zone and negative (accretion) in the swash zone where the net rate becomes zero slightly seaward of the still water shoreline at the location of the maximum $\overline{hCU_s}$ in Figure 4.12. The net suspension rate for the erosional case 500 is slightly negative (more than -0.03) in the outer surf zone and slightly positive (less than 0.02) in the inner surf zone where the net rate becomes zero at the location of the minimum $\overline{hCU_s}$ in Figure 4.12. The net suspension rate for the neutral case 801 fluctuates in the range of -0.025 to 0.025 and is relatively small. It is noted that the computed cross-shore variations of $\overline{hCU_s}$ and $(\overline{S} - w_f\overline{C})$ satisfy the time-averaged sediment continuity equation (4.19) within highly fluctuating errors on the order of 0.01. These errors appear to be caused by the finite difference approximation of the cross-shore gradient of the small sediment transport rate $\overline{hCU_s}$ which is sensitive to numerical noises. This is the reason why the bottom elevation change Δz_b during one wave period is expressed as (4.22) in terms of the net settling rate $(w_f\overline{C} - \overline{S})$.

The beach profiles measured after one-hour wave action were reported by Kraus and Larson (1988). The number N of regular waves involved in the one-hour wave action is 318 for case 201 with $T = 11.33$ s and 960 for cases 500 and 801 with $T = 3.75$ s. Since the computation is made only for 100 waves, the beach profile change after the one-hour wave action is simply predicted to be $N\Delta z_b$. This prediction neglects the effects of the evolving beach profile on the wave motion and sediment transport. Figure 4.14 shows the normalized profiles measured initially and after the one-hour wave action and the predicted profile which is the sum of the initial profile and $N\Delta z_b$ in the region of $x \geq 0$. For the accretional case 201, the degree of erosion and accretion is overpredicted for the suspension efficiency $e_B = 0.005$ and is better predicted for $e_B = 0.002$. For the erosional case 500, the predicted profiles using $e_B = 0.005$ and 0.01 are in reasonable agreement with the measured profile apart from the shift of the bar crest and the erosion depth in the bar trough. For the neutral case 801, the measured and predicted profile changes are small except for the relatively small bar which changed very little during the 20-hr wave action. The empirical suspension efficiency e_B may need to be varied spatially to predict the detailed profile changes.

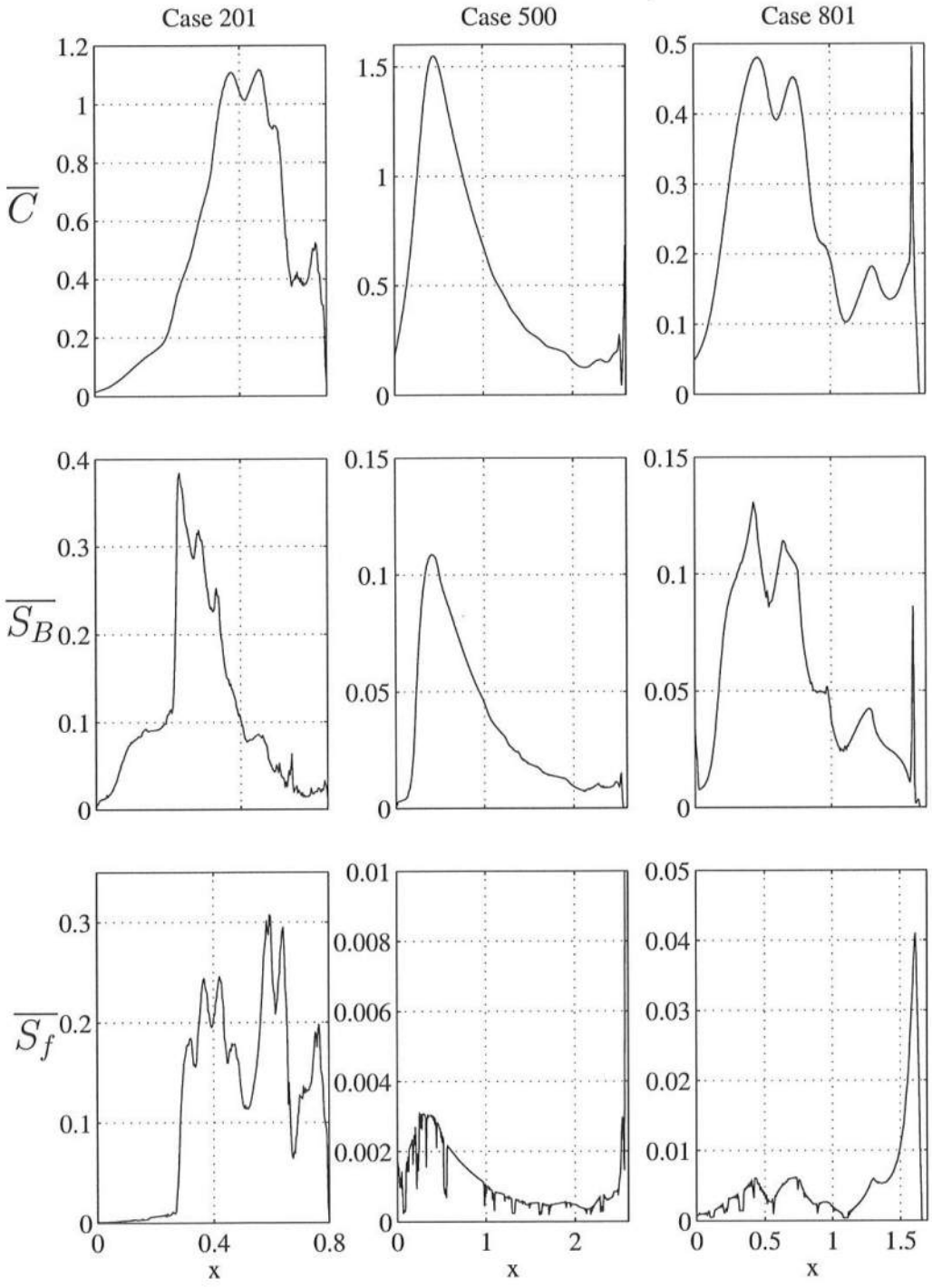

Figure 4.10: Cross-shore Variations of Computed $\overline{C}$, $\overline{S_B}$, and $\overline{S_f}$ for Cases 201, 500, and 801.

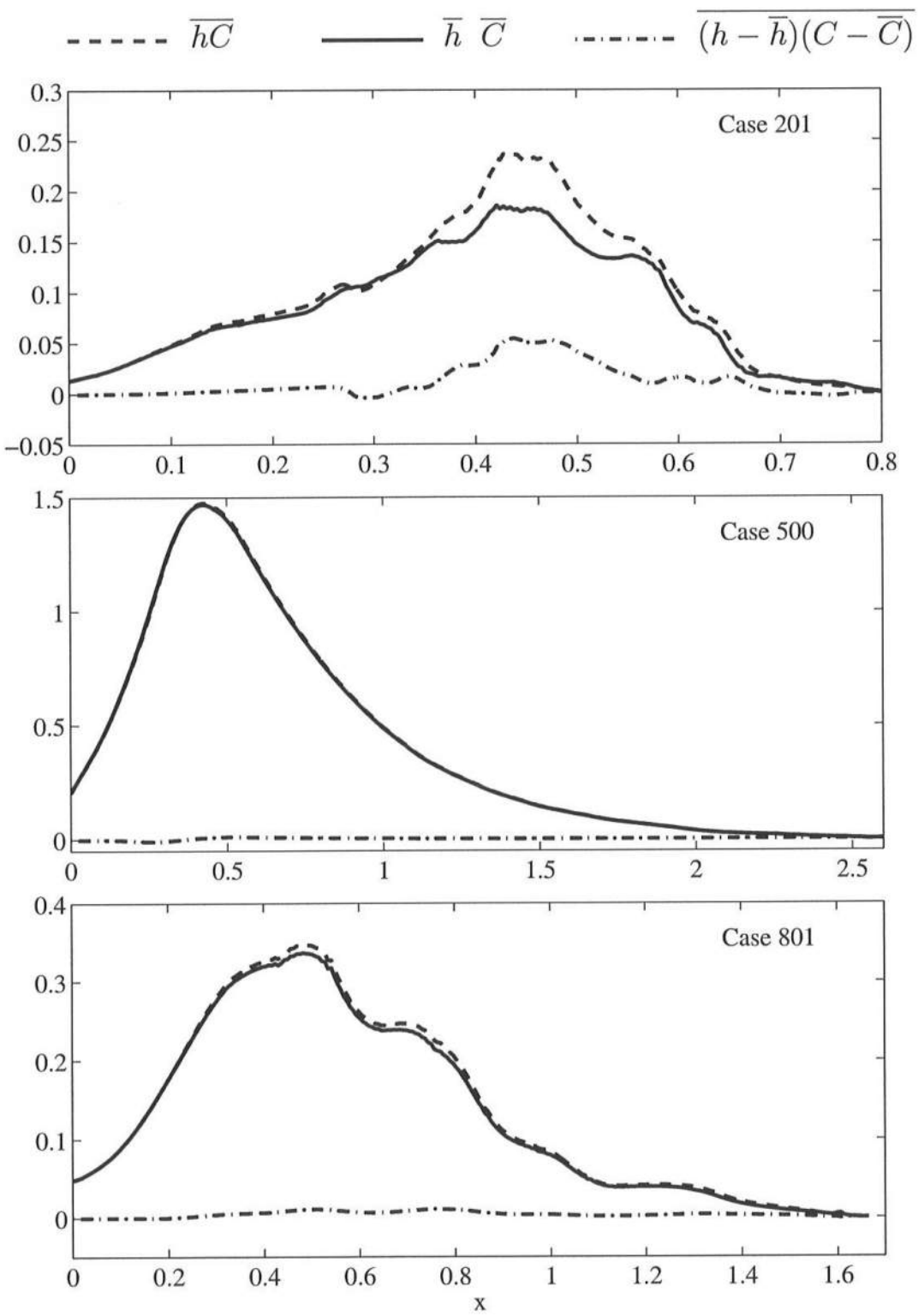

Figure 4.11: Cross-shore Variations of Computed $\overline{hC}$, $\overline{h}\ \overline{C}$, and $\overline{(h-\overline{h})(C-\overline{C})}$ for Cases 201, 500, and 801.

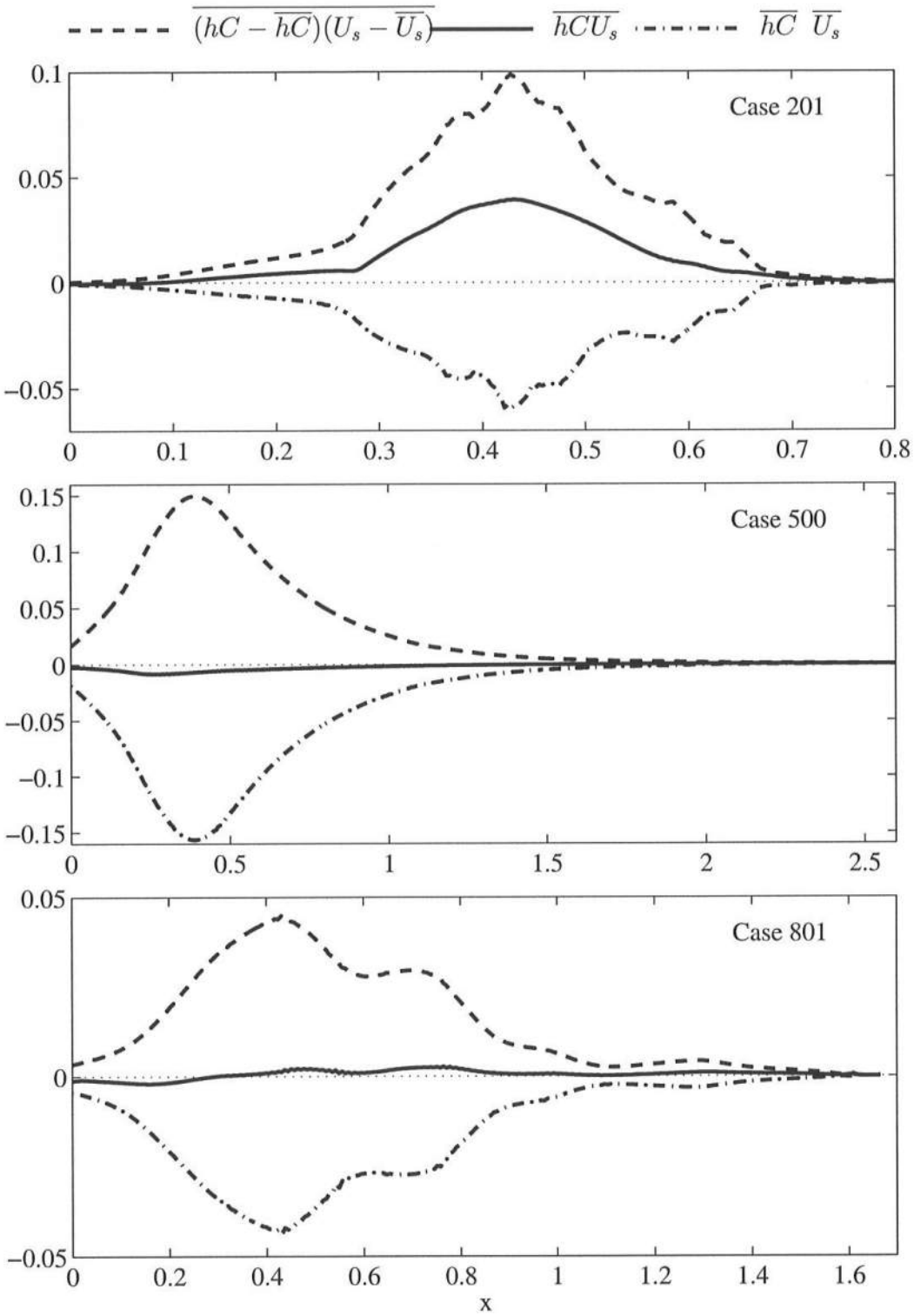

Figure 4.12: Cross-shore Variations of Computed $\overline{(hC-\overline{hC})(U_s-\overline{U_s})}$, $\overline{hCU_s}$, and $\overline{hC}\ \overline{U_s}$ for Cases 201, 500, and 801.

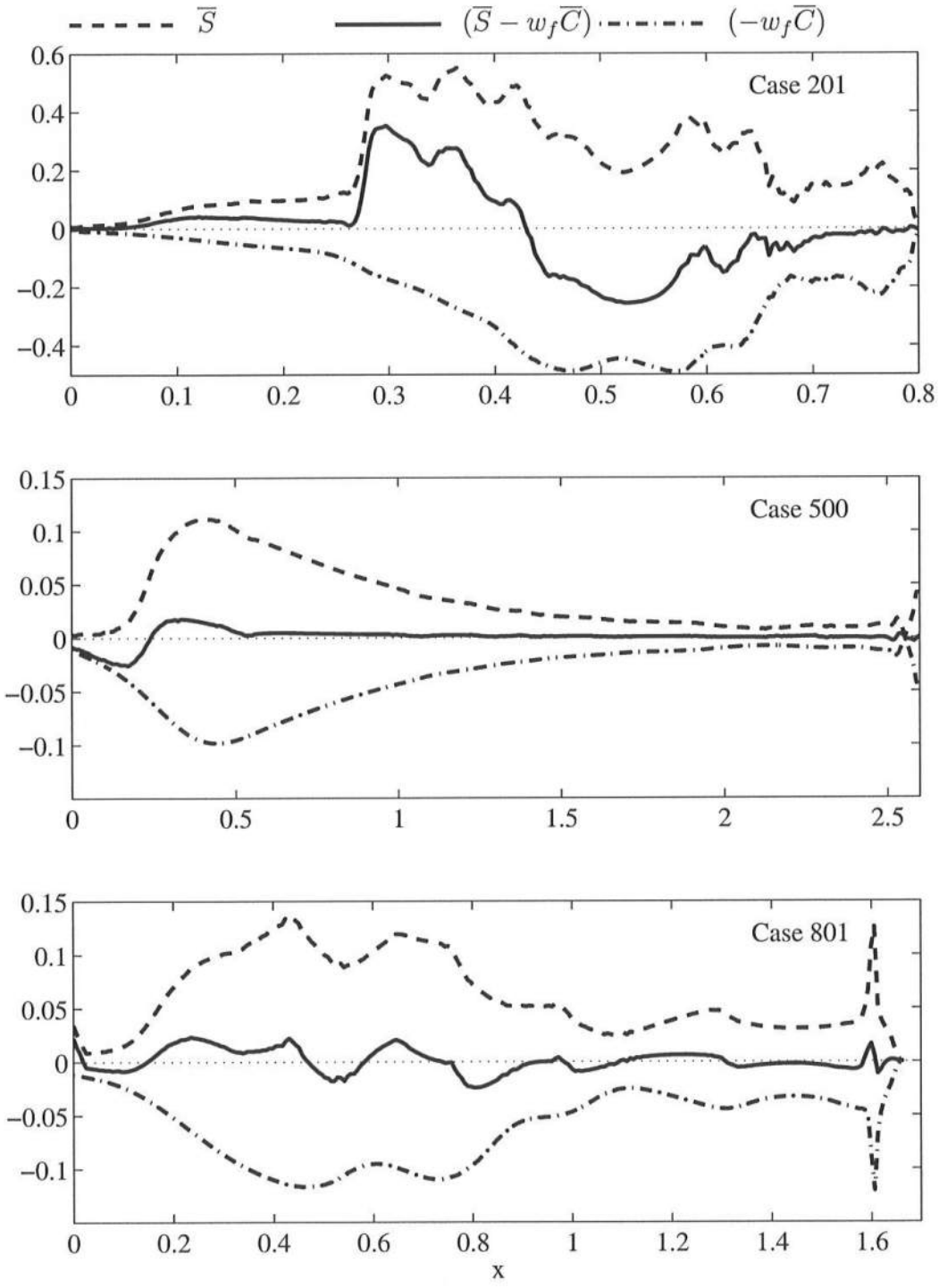

Figure 4.13: Cross-shore Variations of Computed $\overline{S}$, $(\overline{S} - w_f\overline{C})$, and $(-w_f\overline{C})$ for Cases 201, 500, and 801.

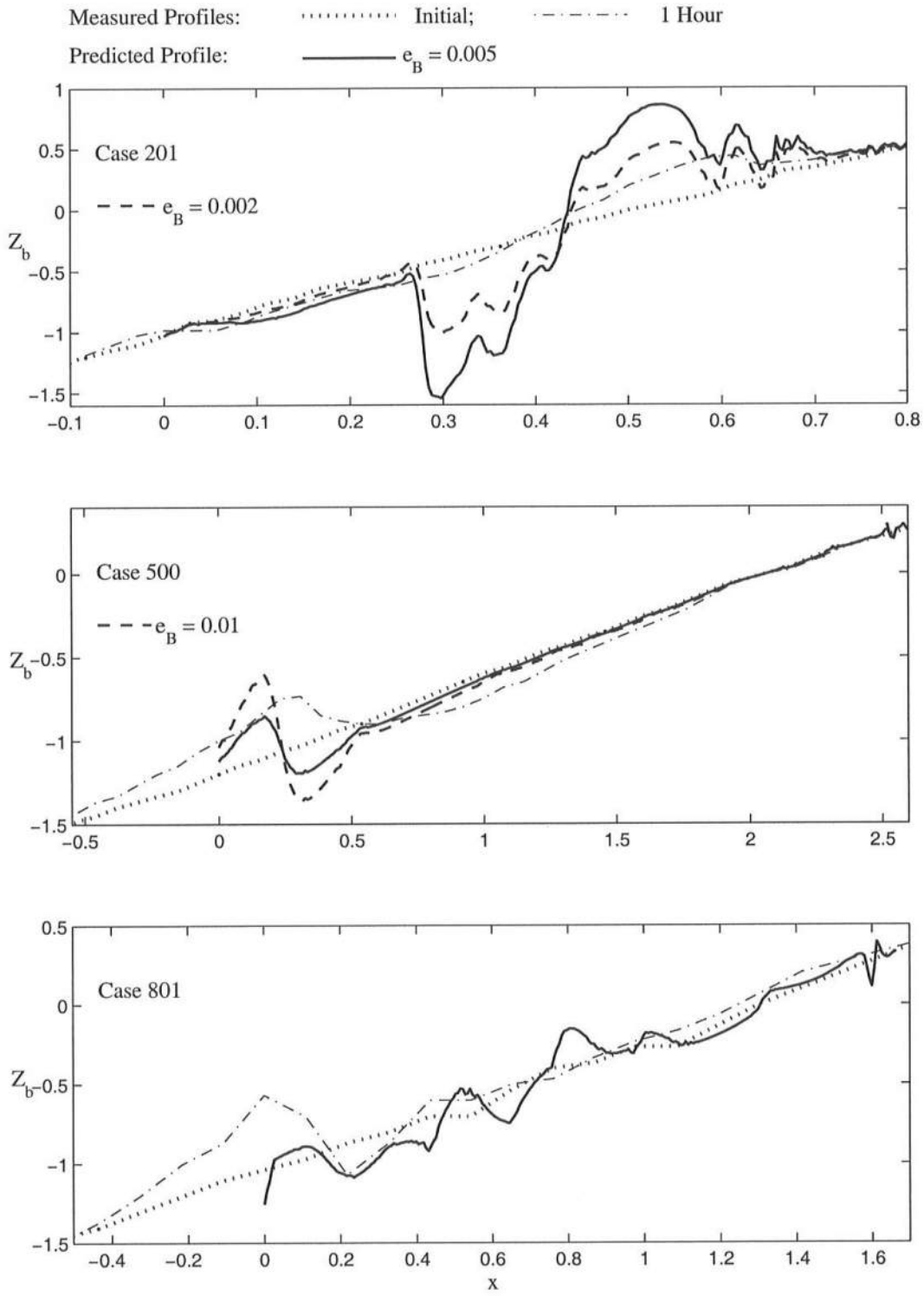

Figure 4.14: Beach Profiles Measured Initially, Measured After 1 hr, and Predicted Profiles using Varied e_B for Cases 201, 500, and 801.

Chapter 5

CONCLUSIONS

A time-averaged model for breaking irregular waves is developed in Chapter 2 to predict the cross-shore variations of the mean and standard deviation of the free surface elevation from outside the surf zone to the lower swash zone. This time-averaged model is derived by averaging the time-dependent continuity, momentum, and energy equations which were used successfully to predict irregular wave runup on beaches. This time-averaged model includes nonlinear corrections terms in the cross-shore radiation stress and energy flux. The correction terms involving the skewness and kurtosis are important in very shallow water. The time-averaging of the time-dependent equations reduces computation time considerably but creates a closure problem. The energy dissipation rate due to wave breaking is estimated using an existing empirical formula in the outer zone. In the inner zone near the still water shoreline, a new empirical formula for $H_* = H_{rms}/\overline{h}$ is proposed to describe the landward increase of H_*. In addition, simple empirical formulas are proposed to express the skewness and kurtosis as a function of H_*.

The developed model is calibrated and compared with three irregular wave tests on a 1:16 smooth impermeable slope and two tests on quasi-equilibrium terraced and barred beaches. Verification is conducted using five independent laboratory tests on a 1:30 slope as well as additional comparisons with field data collected at the Field Research Facility. The major improvements of the new model in comparison to existing models are that it is capable of predicting the wave setup and

root-mean-square wave height near the still water shoreline. Coupling of the new wave model with a cross-shore sediment transport model may make it feasible to predict the erosion and recovery near the still water shoreline.

The runup time series and statistics as measured by a runup wire are shown in Chapter 2 to differ markedly from those measured by vertical wave gauges. The exponential gamma distribution, which was shown by Kobayashi *et al.* (1998) to describe the free surface probability distributions measured in a wave flume, is found to be also capable of describing the measured probability density functions of the runup in the wave flume and the free surface elevations in a surf zone on a natural beach.

A time-dependent cross-shore sediment continuity equation is derived in Chapter 3 that includes sediment suspension, storage, advection, and settling. Time-averaging of this equation creates a closure problem associated with the correlation of time-varying quantities. Several empirical assumptions are made to obtain a simple model for beach profile evolution. A semi-analytical solution is derived for constant water level and wave conditions and compared with three large-scale laboratory tests with accretional, erosional, and neutral (little) beach profile changes. This simple model predicts both shoreline accretion and erosion but is not accurate enough to predict detailed features. Finally, equilibrium terraced and barred beach data are used to assess the assumption of constant energy dissipation rate per unit volume for equilibrium profiles. This assumption is less accurate than the standard equilibrium profile. A different approach will need to be devised to solve the closure problem for the time-averaged sediment continuity equation.

A time-dependent, cross-shore sediment transport model is developed to predict the temporal and spatial variations of the depth-averaged sediment concentration in surf and swash zones in Chapter 4. The model is based on the depth-integrated sediment continuity equation which includes sediment suspension by turbulence generated by wave breaking and bottom friction, sediment storage in the entire water column, sediment advection by waves and wave-induced return current, and sediment settling on the movable bottom. The sediment suspension rate is expressed in terms of the wave energy dissipation rates due to wave breaking and bottom friction using the simplified transport equation for the turbulent kinetic energy which includes the negative buoyancy effect due to suspended sediment. The rate of the bottom elevation change is computed using the volume conservation of bottom sediment and the net sediment settling rate. The hydrodynamic input required for this sediment transport model is predicted using the finite-amplitude, shallow-water equations including bottom friction. The combined numerical model called CBREAK is explained concisely. The present version of CBREAK does not include the effects of the bottom profile change on the wave motion and sediment transport.

The time-dependent numerical model is compared with the same three large-scale laboratory tests of accretional, erosional, and neutral (little) beach profile changes as presented in Chapter 3. Sediment suspension is predicted to be intense under the steep front of breaking waves and mild but persistent in the thin layer of water flowing downslope in the swash zone which is affected by bottom friction. The response of the depth-averaged sediment concentration to the sediment suspension rate is damped and shifted due to the sediment storage and advection. As the normalized sediment fall velocity is reduced, the mean sediment concentration becomes dominant in comparison to the oscillatory concentration. The positively-correlated oscillatory components of the suspended sediment volume per unit area and the

horizontal sediment velocity cause relatively small onshore sediment transport. The product of the mean suspended sediment volume and the mean horizontal sediment velocity yields relatively small offshore sediment transport. The net cross-shore sediment transport rate is the small difference between the relatively small onshore and offshore transport rates, which is difficult to predict accurately. The net sediment suspension rate is also the small difference between the mean suspension rate and the mean settling rate but can be used directly to predict the rate of the bottom elevation change. The predicted profile changes are consistent with the measured initial profile changes. CBREAK can predict the formation of a berm above the still water shoreline and the formation of a bar in the outer surf zone, although it can not predict the detailed profile changes using the constant suspension efficiencies e_B and e_f. CBREAK will need to be compared with irregular wave data and detailed measurements of sediment concentration and fluid velocities. Additionally, the effects of bottom profile changes on the wave motion and sediment transport will need to be included.

BIBLIOGRAPHY

Abramowitz, M., and Stegun, I.A. (1972). *Handbook of Mathematical Functions.* Dover Publications, NY.

Bagnold, R.A. (1966). "An approach to the sediment transport problem from general physics." Professional Paper 422-I, U.S. Geological Survey, Government Printing Office, Washington, D.C.

Bailard, J.A. (1981). "An energetics total sediment transport model for a plane sloping beach." *Journal of Geophysical Research*, 86(C11), 19038–10954.

Battjes, J.A. (1974). "Surf similarity." *Proceedings of the 14^{th} Coastal Engineering Conference*, ASCE, 466–480.

Battjes, J.A. (1988). "Surf-zone dynamics." *Annual Review of Fluid Mechanics*, 20, 257–293.

Battjes, J.A., and Janssen, J.P.F.M. (1978). "Energy loss and set-up due to breaking of random waves." *Proceedings of the 16^{th} Coastal Engineering Conference*, ASCE, 569–587.

Battjes, J.A., and Stive, M.J.F. (1985). "Calibration and verification of a dissipation model for random breaking waves." *Journal of Geophysical Research*, 90(C5), 9159–9167.

Baquerizo, A., Losada, M.A., Smith, J.M., and Kobayashi, N. (1997). "Cross-shore variation of wave reflection from beaches." *Journal of Waterway, Port, Coastal, and Ocean Engineering*, 123(5), 274–279.

Beach, R.A., and Sternberg, R.W. (1991). "Infragravity driven suspended sediment transport in the swash, inner and outer surf zone." *Proceedings of Coastal Sediments '91*, ASCE, 114–128.

Beach, R.A., and Sternberg, R.W. (1992). " Suspended sediment transport in the surf zone: Response to incident wave and longshore current interaction." *Marine Geology*, 103, 513–520.

Bowen, A.J. (1969). "The generation of longshore currents on a plane beach." *Journal of Marine Research*, 27, 206–215.

Conley, D.C., and Inman, D.L. (1992). "Field observations of the fluid-granular boundary layer under near-breaking waves." *Journal of Geophysical Research*, 97(C6), 9631–9643.

Cox, D.T., Kobayashi, N., and Kriebel, D.L. (1994a). "Numerical model verification using SUPERTANK data in surf and swash zones." *Proceedings of Coastal Dynamics '94*, ASCE, 248–262.

Cox, D.T., Kobayashi, N., and Okayasu, A. (1994b). "Vertical variations of fluid velocities and shear stress in surf zones." *Proceedings of the 24th Coastal Engineering Conference*, ASCE, 98–112.

Creed, C.G., Dalrymple, R.A., Kriebel, D.L., and Kaihatu, J.M. (1992). "Equilibrium beach profiles with random seas." *Proceedings of the 23rd Coastal Engineering Conference*, ASCE, 1973–1986.

Dally, W.R. (1992). "Random breaking waves: Field verification of a wave-by-wave algorithm for engineering application." *Coastal Engineering*, 16, 369–397.

Dalrymple, R.A. (1992). "Prediction of storm/normal beach profiles." *Journal of Waterway, Port, Coastal, and Ocean Engineering*, 118(2), 193-200.

Dean, R.G. (1977). "Equilibrium beach profiles: U.S. Atlantic and Gulf coasts." *Ocean Engineering Report 12*, Department of Civil Engineering, University of Delaware, Newark, DE.

Dean, R.G. (1991). "Equilibrium beach profile: Characteristics and applications." *Journal of Coastal Research*, 7(1), 53–84.

Deigaard, R., Fredsøe, J., and Hedegaard, I.B. (1986). "Suspended sediment in the surf zone." *Journal of Waterway, Port, Coastal and Ocean Engineering*, 112(1), 115–127.

Duy, N.T., and Shibayama, T. (1997). "A convection-diffusion model for suspended sediment in the surf zones." *Journal of Geophysical Research*, 102(C10), 23169–23186.

Foster, D.L., Bowen, A.J., Beach, R.A., and Holman, R.A. (1996). "A comparison of field observations and quasi-steady linear shear instabilities of the wave bottom boundary layer." *Proceedings of the 25th Coastal Engineering Conference*, ASCE, 3207–3218.

Gallagher, E.L., Elgar, S., and Guza, R.T. (1998). "Observations of sand bar evolution on a natural beach." *Journal of Geophysical Research*, 103(C2), 3203–3215.

Garcez Faria, A.F., Thornton, E.B., Stanton, T.P., Soares, C.V., and Lippmann, T.C. (1998). "Vertical profiles of longshore currents and bottom roughness." *Journal of Geophysical Research*, 103(C2), 3217–3232.

Grant, W.D., and Madsen, O.S. (1986). "The continental shelf bottom boundary layer." *Annual Review of Fluid Mechanics*, 18, 265–305.

Guza, R.T., and Thornton, E.B. (1980). "Local and shoaled comparisons of sea surface elevations, pressures, and velocities." *Journal of Geophysical Research*, 85(C3), 1524–1530.

Guza, R.T., and Thornton, E.B. (1982). "Swash oscillations on a natural beach." *Journal of Geophysical Research*, 87(C1), 483–491.

Guza, R.T., and Thornton, E.B. (1985). "Velocity moments in nearshore." *Journal of Waterway, Port, Coastal, and Ocean Engineering*, ASCE, 111(2), 235–256.

Hanes, D.M. (1991). "Suspension of sand due to wave groups." *Journal of Geophysical Research*, 96(C5), 8911–8915.

Hanson, H., and Kraus, N.C. (1989). "GENESIS: Generalized model for simulating shoreline change." *Technical Report CERC-89-19*, U.S. Army Engineer Waterways Experiment Station, Vicksburg, MS.

Hay, A.E., and Bowen, A.J. (1994). "Coherence scales of wave-induced suspended sand concentration fluctuations." *Journal of Geophysical Research*, 99(C6), 12749–12765.

Hedegaard, I.B., Roelvink, J.A., Southgate, H., Pechon, P., Nicholson, J., and Hamm, L. (1992). "Intercomparison of coastal profile models." *Proceedings of the 23rd Coastal Engineering Conference*, ASCE, 2108–2121.

Hillyer, T.M., Stakhir, E.Z., and Sudar, R.A. (1997). "An evolution of the economic performance of the U.S. Army Corps of Engineers shore protection program." *Journal of Coastal Research*, 13(1),8–22.

Holland, K.T., and Holman, R.A. (1993). "The statistical distribution of swash maxima on natural beaches." *Journal of Geophysical Research*, 98(C6), 10271–10278.

Jaffe, B.E., and Rubin, D.M. (1996). "Using nonlinear forecasting to learn the magnitude and phasing of time-varying sediment suspension in the surf zone." *Journal of Geophysical Research*, 101(C6), 14283–14296.

Johnson, B.D., and Kobayashi, N. (1998a). "Nonlinear time-averaged model in surf and swash zones." *Proceedings of the 26th Coastal Engineering Conference*, ASCE, 2785–2798.

Johnson, B.D., and Kobayashi, N. (1998b). "Nearshore water level surges in the surf zone." *Research Report No. CACR-98-08*, Center for Applied Coastal Research, University of Delaware, Newark, DE.

Kobayashi, N. (1987). "Analytical solution for dune erosion by storms." *Journal of Waterway, Port, Coastal, and Ocean Engineering*, 113(4), 401–418.

Kobayashi, N., DeSilva, G.S., and Watson, K.D. (1989). "Wave transformation and swash oscillation on gentle and steep slopes." *Journal of Geophysical Research*, 94(C1), 951–966.

Kobayashi, N., Herrman, M.N., Johnson, B.D., and Orzech, M.D. (1998). "Probability distribution of surface elevation in surf and swash zones." *Journal of Waterway, Port, Coastal and Ocean Engineering*, 124(3), 99–107.

Kobayashi, N., and Johnson, B.D. (1998). "Computer program CSHORE for predicting cross-shore transformation of irregular breaking waves." *Research Report No. CACR-98-04*, Center for Applied Coastal Research, University of Delaware, Newark, DE.

Kobayashi, N., and Karjadi, E.A. (1996). "Obliquely incident irregular waves in surf and swash zones." *Journal of Geophysical Research*, 101(C3), 6527–6542.

Kobayashi, N., Karjadi, E.A., and Johnson, B.D. (1997a). "Dispersion effects on longshore currents in surf zones." *Journal of Waterway, Port, Coastal, and Ocean Engineering*, 123(5), 240–248.

Kobayashi, N., Orzech, M.D., Johnson, B.D., and Herrman, M.N. (1997b). "Probability modeling of surf zone and swash dynamics." *Proceedings Waves '97*, ASCE, 107–121.

Kobayashi, N., Otta, A.K., and Roy, I. (1987). "Wave reflection and runup on rough slopes." *Journal of Waterway, Port, Coastal, and Ocean Engineering*, 113(3), 282–298.

Kobayashi, N., and Seo, S.N. (1985). "Fluid and sediment interaction over a plane bed." *Journal of Hydraulic Engineering*, 111(6), 903–921.

Kobayashi, N., Tega, Y., and Hancock, M.W. (1996). "Wave reflection and overwash of dunes." *Journal of Waterway, Port, Coastal, and Ocean Engineering*, 122(3), 150–153.

Kobayashi, N., and Wurjanto, A. (1992). "Irregular wave setup and runup on beaches." *Journal of Waterway, Port, Coastal, and Ocean Engineering*, 118(4), 368–386.

Komar, P.D., and Holman, R.A. (1986). "Coastal processes and the development of shoreline erosion." *Annual Review of Earth Planet Science*, 14,237–265.

Kraus, N.C., and Larson, M. (1988). "Beach profile change measured in the tank for large waves, 1956–1957 and 1962." *Technical Report CERC-88-6*, U.S. Army Engineer Waterways Experiment Station, Vicksburg, MS.

Kraus, N.C., Larson, M., and Kriebel, D.L. (1991). "Evaluation of beach erosion and accretion predictors." *Proceedings of Coastal Sediments '91*, ASCE, 572–587.

Kriebel, D.L. (1994). "Swash zone wave characteristic from SUPERTANK." *Proceedings of the 24^{th} Coastal Engineering Conference*, ASCE, 2207–2221.

Kriebel, D.L., and Dean, R.G. (1985). "Numerical simulation of time-dependent beach and dune erosion." *Coastal Engineering*, 9, 221–245.

Kriebel, D.L., Kraus, N.C., and Larson, M. (1991). "Engineering methods for predicting beach profile response." *Proceedings of Coastal Sediments '91*, ASCE, 557–571.

LeVeque, R.J. (1990). *Numerical Methods for Conservation Laws.* Birkhauser-Verlag, Basel, Cambridge, MA.

Li, Z., and Davies, A.G. (1996). "Towards predicting sediment transport in combined wave-current flow." *Journal of Waterway, Port, Coastal, and Ocean Engineering*, 122(4), 157–164.

Lin, P., and Liu, P.L.-F. (1998). "Turbulence transport, vorticity dynamics, and solute mixing under plunging breaking waves in surf zone." *Journal of Geophysical Research*, 103(C8), 15677–15694.

Lippmann, T.C., and Holman, R.A. (1990). "The spatial and temporal variability of sand bar morphology." *Journal of Geophysical Research*, 95(C7), 11575–11590.

Longuet-Higgins, M.S. (1970). "Longshore currents generated by obliquely incident sea waves. Parts 1 and 2." *Journal of Geophysical Research*, 75,6778–6801.

Madsen, O.S., Wright, L.D., Boon, J.D., and Chisholm, T.A. (1993). "Wind stress, bed roughness and sediment suspension on the inner shelf during an extreme storm event." *Continental Shelf Research*, 13, 1303–1324.

Mase, H. and Kobayashi, N. (1991). "Transformation of random breaking waves and its empirical numerical model considering surf beat." *Procedings of Coastal Sediments '91*, ASCE, 688–702.

Mei, C.C. (1989). *The Applied Dynamics of Ocean Surface Waves.* World Scientific, River Edge, NJ.

Muste, M., and Patel, V.C. (1997). "Velocity profiles for particles and liquid in open-channel flow with suspended sediment." *Journal of Hydraulic Engineering*, 123(9), 742–751.

National Research Council. (1987). *Responding to changes in Sea Level: Engineering Implications.* Marine Board, National Academy Press, Washington, D.C.

National Research Council. (1990). *Managing Coastal Erosion.* Marine Board, National Academy Press, Washington, D.C.

National Research Council. (1995). *Beach Nourishment and Protection.* Marine Board, National Academy Press, Washington, D.C.

Nielsen, P. (1992). *Coastal Bottom Boundary Layers and Sediment Transport.* World Scientific, River Edge, NJ.

Ochi, M.K., and Wang, W.C. (1984). "Non-Gaussian characteristics of coastal waves." *Proceedings of the 19th Coastal Engineering Conference*, ASCE, 516–531.

Orzech, M.D., and Kobayashi, N. (1998). "Equilibrium terraced and barred beaches." *Proceedings of the 26th Coastal Engineering Conference*, ASCE, 2736–2749.

Osborne, P.D., and Rooker, G.A. (1999). "Sand re-suspension events in a high energy infragravity swash zone." *Journal of Coastal Research*, 15(1), 74–86.

Peregrine, D.H. (1983). "Breaking waves on beaches." *Annual Revue of Fluid Mechanics*, 15, 149–178.

Pedersen, C., Deigaard, R., Fredsøe, J., and Hansen, E.A. (1995). "Simulation of sand in plunging breakers." *Journal of Waterway, Port, Coastal, and Ocean Engineering*, 121(2), 77–87.

Phillips, O.M. (1977). *Dynamics of the Upper Ocean, 2^{n}d Edition.* Cambridge University Press, London.

Plant, N., and Holman, R.A. (1996). "Interannual shoreline variations at Duck, N.C., USA." *Proceedings of the 25th Coastal Engineering Conference*, ASCE, 3521–3533.

Puleo, J.A., Beach, R.A., Holman, R.A., and Allen, J.S. (2000). "Swash zone sediment suspension and transport and the importance of bore-generated turbulence." *Journal of Geophysical Research*, 105(C7), 17021-17044.

Raubenheimer, B., and Guza, R.T. (1996). "Observations and predictions of run-up." *Journal of Geophysical Research*, 101(C10), 25575–25587.

Raubenheimer, B., Guza, R.T., and Elgar, S. (1996). "Wave transformation across the inner surf zone." *Journal of Geophysical Research*, 101(C10), 25589–25597.

Raubenheimer, B., Guza, R.T., Elgar, S., and Kobayashi, N. (1995). "Swash on a gently sloping beach." *Journal of Geophysical Research*, 100(C5), 8751–8760.

Raudkivi, A.J. (1990). *Loose Boundary Hydraulics.* 3rd Edition, Pergamon Press, New York, NY

Roelvink, J.A., and Stive, M.J.F. (1989). "Bar-generating cross-shore flow mechanisms on a beach." *Journal of Geophysical Research*, 94(C4), 4785–4800.

Schäffer, H.A., Deigaard, R., and Madsen, P. (1992). "A two-dimensional surf zone model based on the Boussinesq equations." *Proceedings of the 23rd Coastal Engineering Conference*, ASCE, 576–589.

Svendsen, I.A. (1984a). "Mass flux and undertow in a surf zone." *Coastal Engineering*, 8, 347–365.

Svendsen, I.A. (1984b) "Wave attenuation and set-up on a beach." *Proceedings of the 19th Coastal Engineering Conference*, ASCE, 54–69.

Svendsen, I.A., and U. Putrevu (1995). "Surf Zone Dynamics" *Advances in Coastal and Ocean Engineering, Volume 2*, World Scientific Publishing, River Edge, NJ.

Tennekes, H., and Lumley, J.L. (1974). *A First Course in Turbulence*, MIT Press, Cambridge, MA.

Thornton, E.B., and Guza, R.T. (1983). "Transformation of wave height distribution." *Journal of Geophysical Research*, 88(C10), 5925–5938.

Thornton, E.B., Humiston, R.T., and Birkemeier, W. (1996). "Bar/trough generation on a natural beach." *Journal of Geophysical Research*, 101(C5), 12097–12110.

Trowbridge, J., and Young, D. (1989). "Sand transport by unbroken water waves under sheet flow conditions." *Journal of Geophysical Research*, 94(C8), 10971–10991.

Van Rijn, L.C., and Kroon, A. (1992). "Sediment transport by currents and waves." *Proceedings of the 23rd Coastal Engineering Conference*, ASCE, 2613–2628.

Wang, P. (1998). "Longshore sediment flux in water column and across surf zone." *Journal of Waterway, Port, Coastal, and Ocean Engineering*, 124(3), 108–117.

Zheng, J., and Dean, R.G. (1996). "Comparisons of erosion models for storms at Ocean City, MD." *Proceedings of the 25th Coastal Engineering Conference*, ASCE, 3115–3128.